

CONFIDENTIAL

X63-20825

# APOLLO

## *Final Report*

(NASA-CR-141987) APOLLO: SPACE ENVIRONMENT  
FACTORS: EVALUATION OF THE RADIATION AND  
METEORITE ENVIRONMENT AND DEVELOPMENT OF  
SAFETY PROCEDURES Final Report (Martin Co.)  
163 p

N75-71794

Unclas

00/98 08662

EXTRA  
K 21

ER 12018 JUNE 1961



## *Space Environment Factors*

CLASSIFICATION CHANGE

TO

~~CONFIDENTIAL~~  
UNCLASSIFIED

By authority of

E.O. 11652

Changed by

L. Shirley

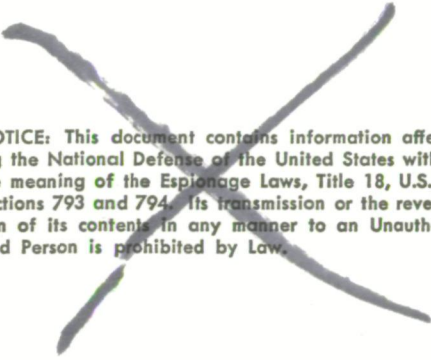
Date 16-15-73

CONFIDENTIAL

MARTIN

EXCLUDED FROM THE GDS

~~CONFIDENTIAL~~



NOTICE: This document contains information affecting the National Defense of the United States within the meaning of the Espionage Laws, Title 18, U.S.C., Sections 793 and 794. Its transmission or the revelation of its contents in any manner to an Unauthorized Person is prohibited by Law.

~~CONFIDENTIAL~~

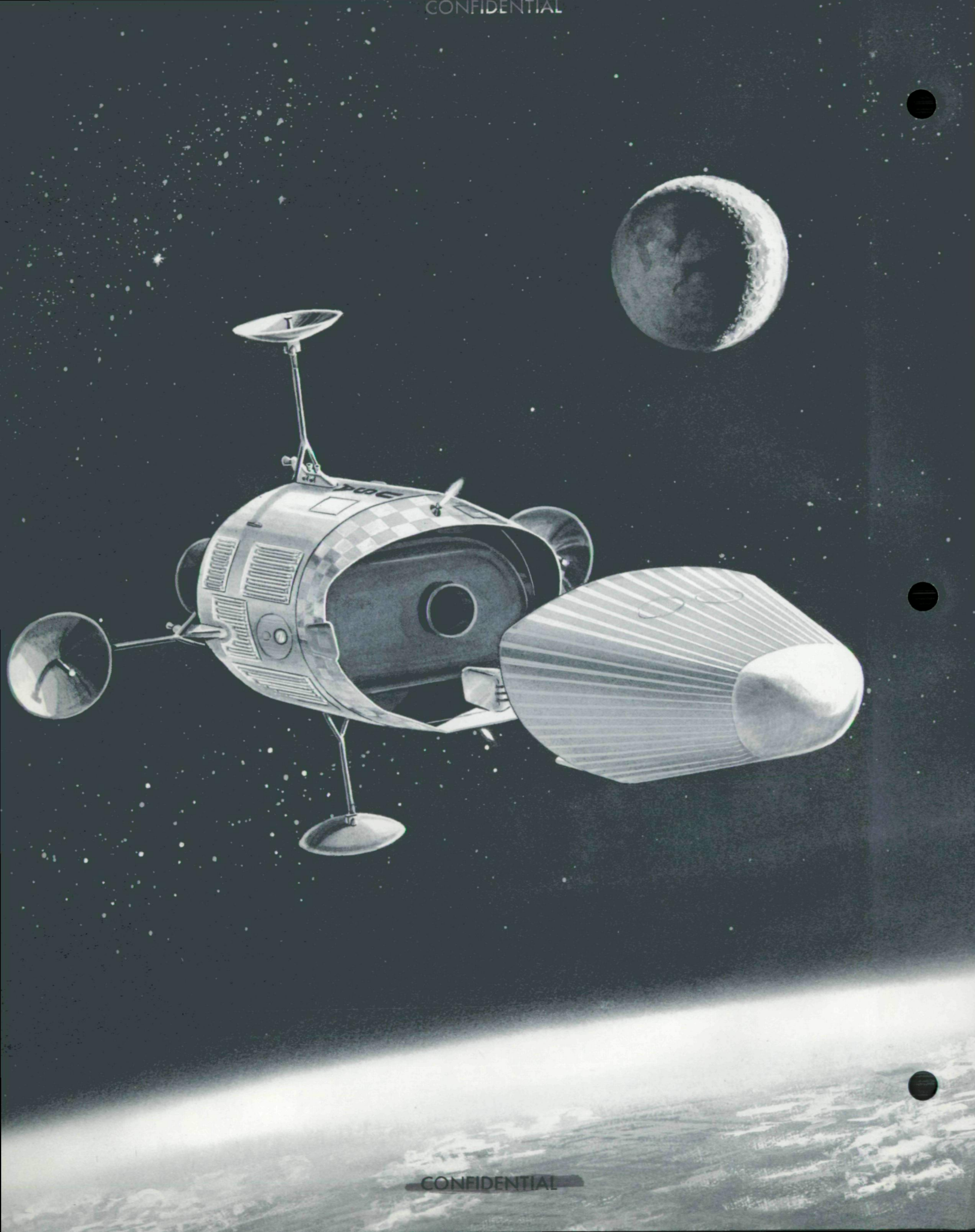
CONFIDENTIAL

50

CONFIDENTIAL



CONFIDENTIAL



CONFIDENTIAL



# APOLLO

---

## *Final Report*

Submitted to: NASA Space Task Group.  
Contract NAS 5-303, Exhibit A, Item 1.2

### *Space Environment Factors*

EVALUATION OF THE RADIATION  
AND METEORITE ENVIRONMENT  
AND DEVELOPMENT OF SAFETY  
PROCEDURES

ER 12018      JUNE 1961

MARTIN

EXCLUDED FROM THE GDS

CONFIDENTIAL

CONFIDENTIAL

# MODEL 410 — THE SYSTEM AND ITS OPERATION

## *A BRIEF DESCRIPTION\**

Model 410 is the spacecraft system recommended by Martin for the Apollo mission. Its design satisfies the guidelines stated in NASA RFP-302, as well as a more detailed set of guidelines developed by Martin during the Apollo design feasibility study.

We conceive the ultimate Apollo mission to be a manned journey to the lunar surface, arrived at by the preliminary steps of earth orbit, circumlunar and lunar orbit flights. Operational procedures proved out in the early steps will be carried over into the advanced steps, thus establishing a high level of confidence in the success of the lunar flights. With the recommended system, manned lunar orbit missions can be made as early as 1966.

## **Operational Features**

For a circumlunar flight when the moon is at its most southerly declination (Fig. p-1) the launch operation proceeds southeast from Cape Canaveral and down the Atlantic Missile Range. The Saturn C-2 third stage shuts down when orbital velocity is reached at an altitude of 650,000 feet. What follows is a coasting orbit passing over the southern tip of Africa, the Indian Ocean and up the Pacific Missile Range. In this interval the crew checks out all onboard equipment, which has just passed through the accelerations, noise and vibration of the boost phase. If the pilot-commander is satisfied that all systems are working properly, the third stage is restarted and the spacecraft is injected at parabolic velocity northwest of Hawaii. If the pilot-commander is dissatisfied with the condition of the vehicle or crew, he separates from the Saturn S-IV, starts the mission abort engine, re-enters at the point shown in Fig. p-1 and lands at Edwards AFB.

Continuing translunar flight from the point of injection, the trajectory trace swings down over the Caribbean and then west over South America. This particular trajectory passes within 240 naut mi of the moon, then turns back for a direct re-entry some six days after launch. Re-entry occurs southwest of Hawaii some 3300 naut mi from the Edwards AFB landing site.

*Tracking.* The range coverage provided by present and planned facilities is shown in Fig. p-1 for this trajectory and for a second return trace representing the case when the moon is at the most northerly declination. This second trajectory establishes the 10000-naut mi re-entry range requirement for Apollo to meet the guidelines of operation on every day of the lunar month and of operation into a single landing site.

\*For more complete descriptions, see ER 12000 or ER 12001.



*Abort.* During the critical launch and checkout phase, abort will be possible at any time : at the crew's discretion, automatically or by ground command. Up to nine minutes after launch (from Canaveral), the abort landing is restricted to the AMR for a circumlunar flight. Beyond this point the pilot has the option of continuing to any point along the AMR, PMR or into Edwards AFB through the use of the mission abort propulsion system and the inherent downrange maneuverability of the Model-410.

## The Selected Spacecraft

The Apollo space vehicle (Model 410 spacecraft plus launching vehicle) is shown in Fig. p-2. The spacecraft—that portion of the space vehicle which makes the flight to the moon—consists of these three modules:

- (1) Command module, housing the three crew members during all thrusting periods, e.g., launch from earth, any corrections to the flight path during flight in space, during re-entry and, ultimately, during landing and launch from the moon. It is the operating center from which all control of the flight is made.
- (2) Propulsion and equipment module, containing all the propulsion units which operate between the point of final booster separation and re-entry after the lunar flight. It is separated from the command module at 200 naut mi from the earth on the return trip. It is designed with tankage for lunar takeoff and will be offloaded for less ambitious missions.
- (3) Mission module—contained within the outer frame of the propulsion and equipment module—providing space during the lunar voyage for scientific observations and crew living functions.

### Command Module

With its lifting capability, the Apollo command module represents a step forward in technology over ballistic vehicles, Mercury and (to the best of our knowledge the *Boctók* (*Vostok*)). The lift results from the capsule's shape—a blunted cone flattened on the top (see Fig. p-3).

*Heating and radiation protection.* The Model 410 is shaped conservatively for aerodynamic heating in addition to its relatively high L/D (0.77). By accepting the large convective heat load of a nose radius smaller than that of the Mercury type, the Model 410 shape tends to minimize radiative heat transfer which is less well understood and harder to protect against. The thermal protection system provides excellent protection for the crew from the large aerodynamic heat loads, from space radiation (including solar flares) and from meteorites.

The normal mission radiation dose will not exceed the five rem limit defined by NASA. If the crew should encounter a solar event as severe as that following the May 10, 1959 flare, they would receive a dose of only 67 rem—well within the 100 rem dose limit set by Martin as tolerable during an emergency.

Thermal protection for re-entry is provided by a composite shield of deep charring ablator (nylon phenolic) bonded to superalloy honeycomb panels which are set off and insulated from the water-cooled pressure shell. The control flaps are protected from the high initial heat rate by an ablator bonded directly to the flap. The long-time, lower heating rates are handled by re-radiation from the backside. The aft bulkhead is protected by a fiberglass phenolic honeycomb panel with a foamed polyurethane insulation.

*Crew provisions.* The crew has access to all electronic and electrical equipment in the command module for maintenance and replacement. Both pilots have two-axis sidestick and foot controllers as well as a manual guidance mode used with the computers inoperative for deep space and re-entry operations.

Cabin pressure is maintained at the equivalent of 5000 feet altitude ("shirt sleeve" environment). Protective suiting is donned only for launching and landing, but need not be inflated except in emergency.

*Guidance.* The guidance system consists of both automatic and manual star tracking equipment, as well as two inertial platforms and two general purpose digital computers. Two windows, with ablative heat shield covers, are provided for use with tracking instruments.

*Flight control.* Pitch and yaw attitude control within the atmosphere is provided by flaps driven by hot gas servos. Outside the atmosphere dual reaction controls are used. Roll is controlled at all times by a dual reaction system.

*Communications.* Communications equipment includes a K<sub>a</sub> band for re-entry, a C-band for the pre-reentry and both HF and VHF rescue beacons for landing and recovery.

*Landing system.* The landing system consists of a steerable parachute, retro-rocket combination, enabling the M-410 to avoid local obstacles, trim out wind drift and reduce sinking speed to a nominal three feet per second—low enough for safe landing on any kind of terrain or in very rough seas. In the event of retrorocket failure, accelerations on the crew will not exceed 20 G.

*Launch escape propulsion system (LEPS).* LEPS is a thrust-vector-controlled, solid rocket system which separates the command module from the rest of the space vehicle in the event of an emergency during launch pad operations or during boost through the atmosphere. In an off-the-pad abort, it lifts the command module to an altitude of more than 4000 feet. During a normal boost trajectory, LEPS is jettisoned at 300,000 feet.

### ***Propulsion and Equipment Module***

The propulsion and equipment module (shown in Fig. p-3) contains propulsion devices and equipment which are not necessary for re-entry. Its outer skin serves both as a load carrying structure and as a meteorite shield for the propellant tanks, mission module and other equipment.

*Propulsion devices.* The mission engine, used for trajectory correction and abort, is a high performance, modified LR-115 (Pratt & Whitney), developing 15,600 pounds of thrust. A total of 10,450 pounds of liquid hydrogen and liquid oxygen propellants may be carried, sufficient for lunar takeoff.

~~CONFIDENTIAL~~

Four vernier engines, with 300 pounds of thrust each, are used for mid-course correction, ullage impulse to settle the mission engine propellants and for thrust vector control during operation of the mission engine. In addition there are two sets of six control jets which provide 30 pounds of thrust for roll, pitch and yaw control.

*Power sources.* Spacecraft equipment is powered by fuel cells (2 kw) which under normal conditions, use the boiloff from the mission propulsion system. A supply of independent reactants is provided for emergencies. Battery power is used during re-entry.

*Communications.* Four large antennas fold out to provide S-band communications and X-band radar altimeter information. VHF communications gear is also provided.

### ***Mission Module***

The mission module provides 400 cubic feet of living space during the lunar voyage. It serves as a midcourse work-rest area, providing freedom of movement and privacy. For operations on the lunar surface it will be a base of scientific investigations, and will serve as an airlock. The same "shirt sleeve" environment at 12.2 psi is maintained as in the command module.

The mission module provides the space and flexibility required for effective lunar reconnaissance and scientific experimentation. An Eastman-Kodak camera-telescope has been selected, for example, which has one-meter resolution at lunar orbit altitude of 50 naut mi.

### **MODEL 410 WEIGHT SUMMARY**

MISSION	CIRCUMLUNAR	LUNAR ORBIT	LUNAR TAKEOFF
COMMAND MODULE	6954	6954	6954
PROPULSION AND EQUIPMENT MODULE	7372	13,192	15,618
LAUNCH ESCAPE PROPULSION SYSTEM	185	185	0
ADAPTER	489	489	0
EFFECTIVE LAUNCH WEIGHT	15,000	20,820	22,572

~~CONFIDENTIAL~~



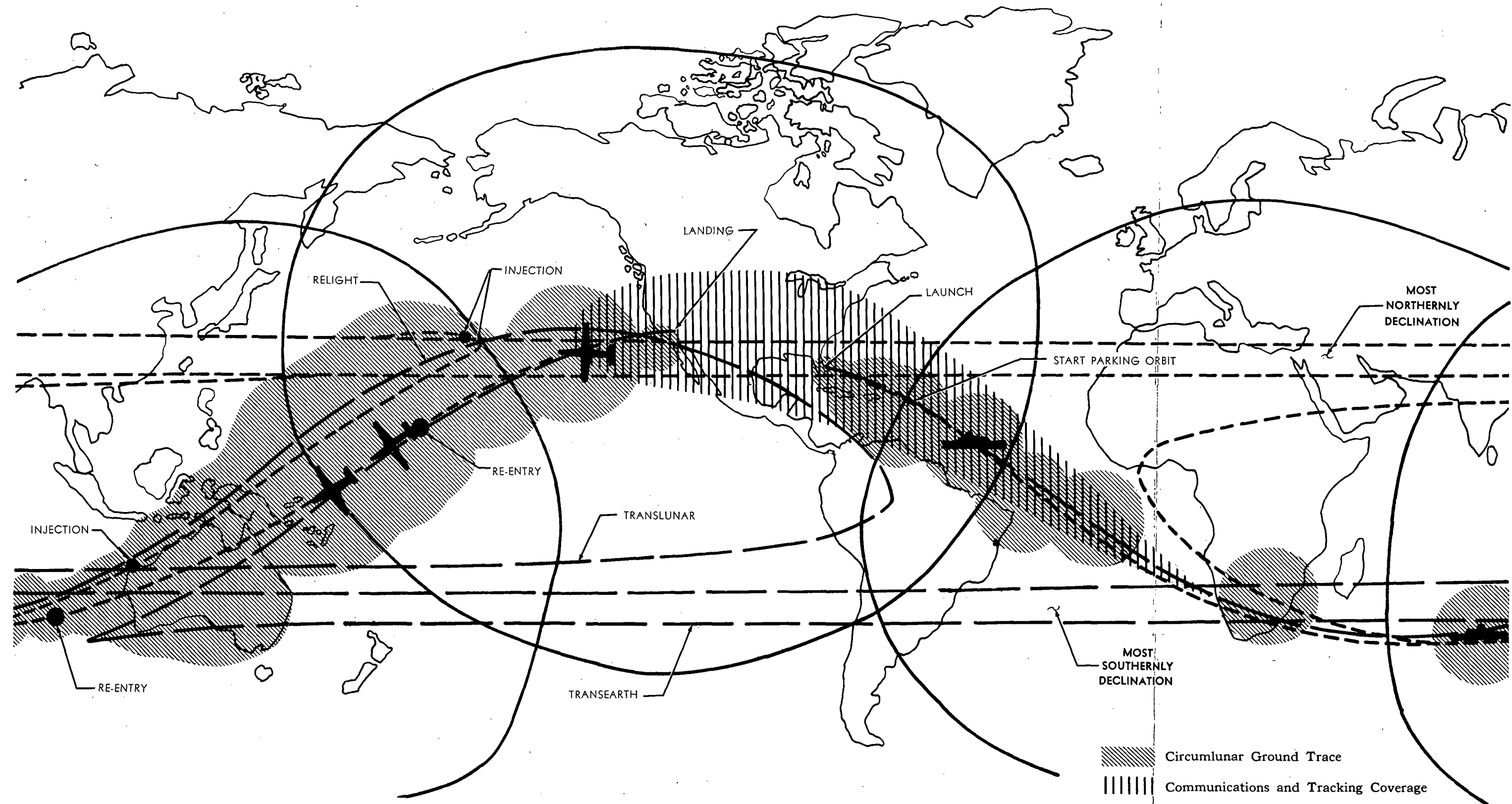


Fig. p-1 Model 410 Circumlunar Trajectory and Range Coverage

CONFIDENTIAL

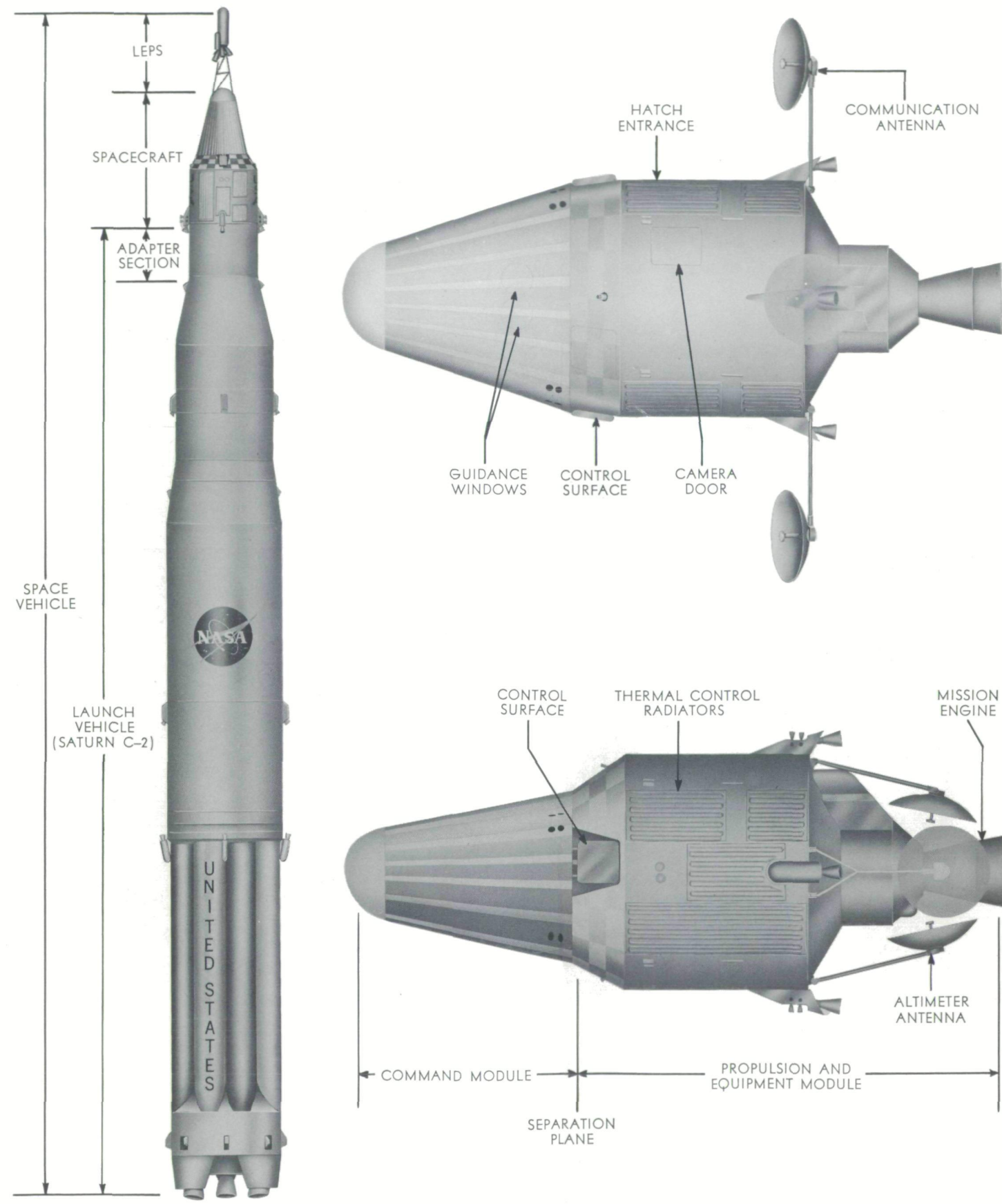
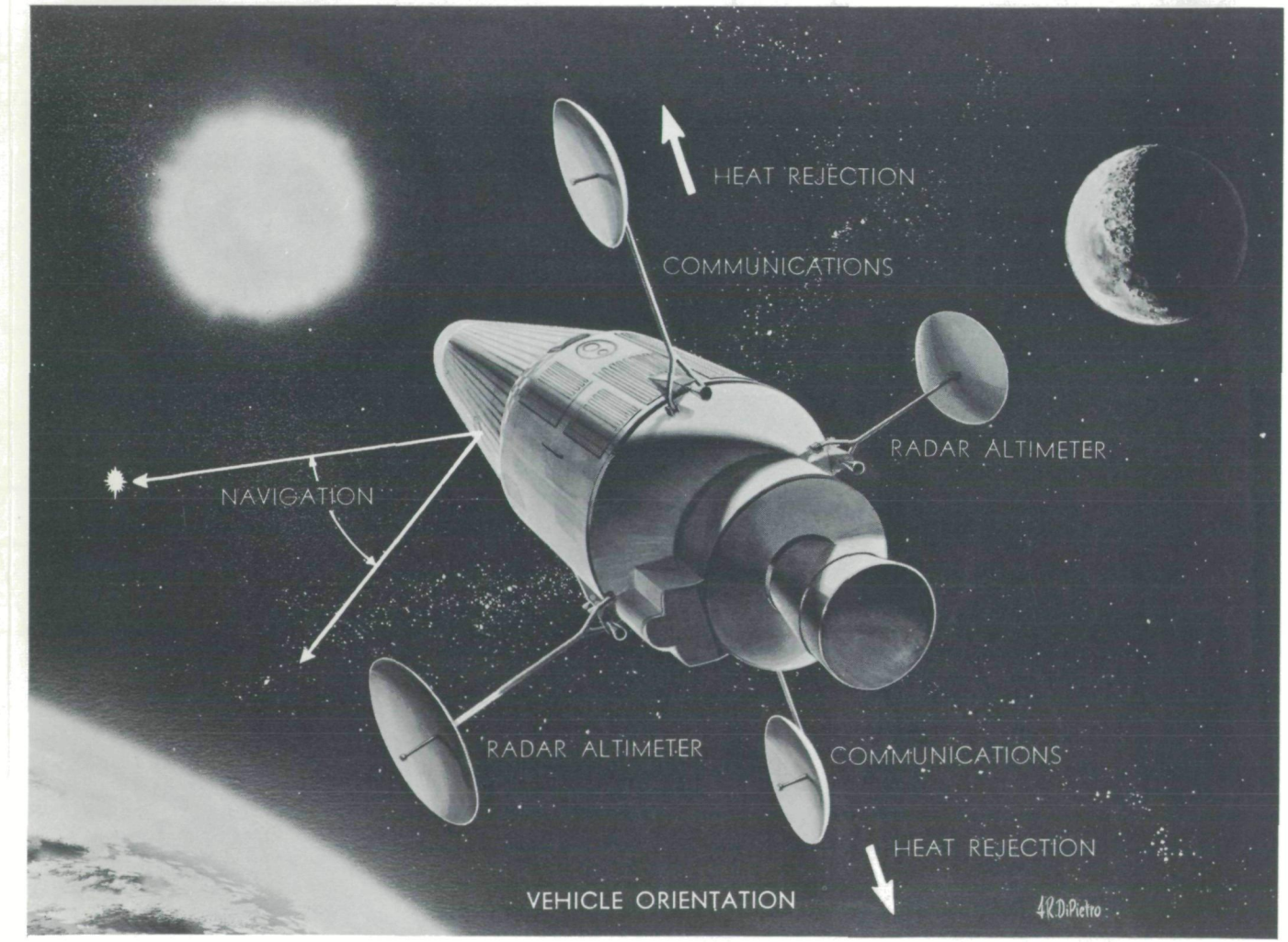


Fig. p-2. Model 410 Apollo Space Vehicle

CONFIDENTIAL

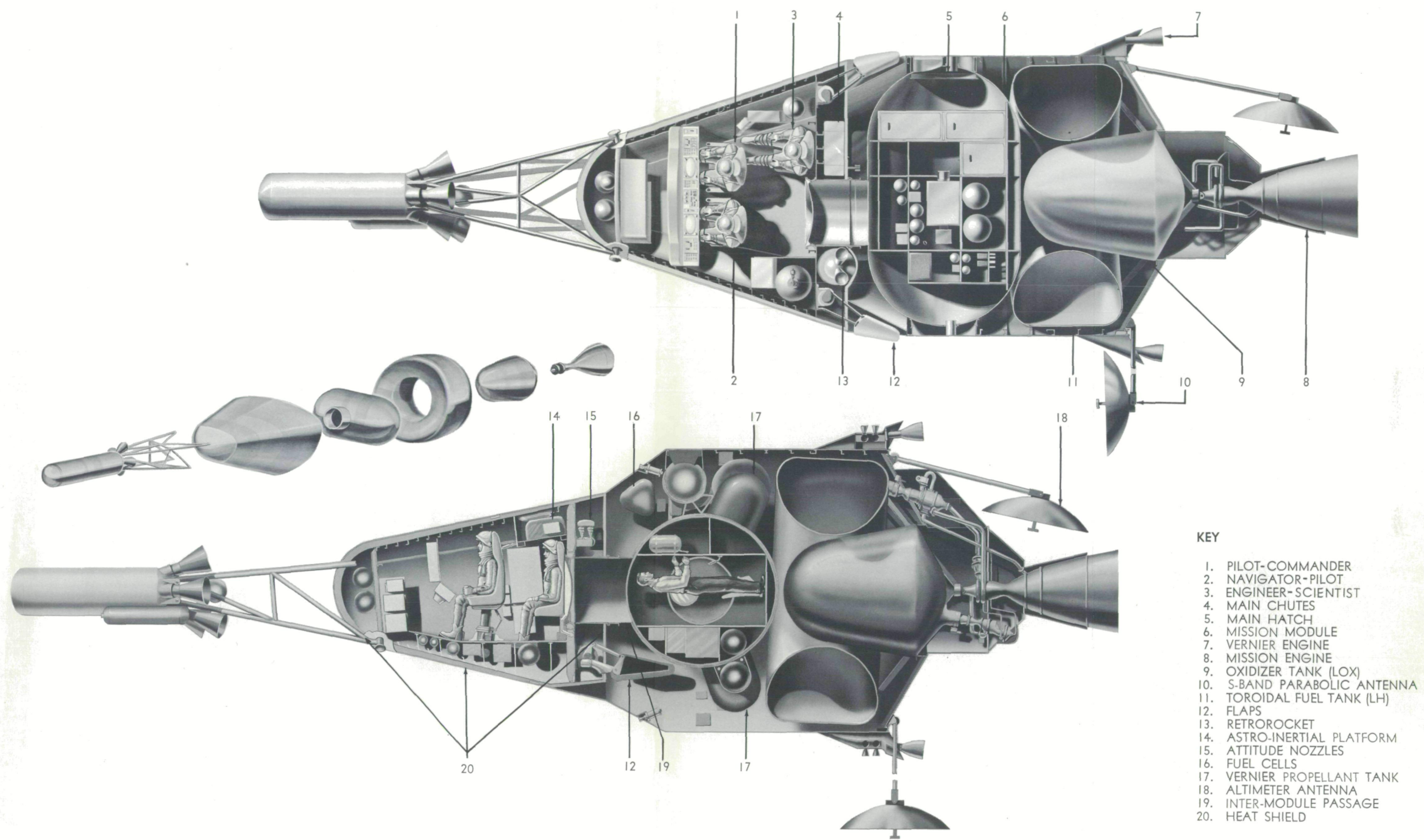
MISSION	EFFECTIVE GROSS WEIGHT (lb)	PROPULSION $\Delta V$ CAPABILITY (fps)		VOLUMES (cu ft)	
		MISSION	VERNIER	COMMAND MODULE	MISSION MODULE
CIRCUMLUNAR	15000	1830	525	350	400
LUNAR ORBIT	20820	6100	525	400	400
LUNAR TAKEOFF	22572	8600	200	MISSION H <sub>2</sub> TANK	MISSION O <sub>2</sub> TANK

PROPULSION SYSTEM DATA			
PURPOSE	TYPE	ISP. (sec)	THRUST (lb)
MISSION (1)	H <sub>2</sub> -O <sub>2</sub> (ADV. LR115)	427	15600
VERNIER (4)	N <sub>2</sub> H <sub>4</sub> /UDMH-N <sub>2</sub> O <sub>4</sub>	315	300 EACH
ATTITUDE CONTROL (14+BACKUP)	N <sub>2</sub> H <sub>4</sub> /UDMH-N <sub>2</sub> O <sub>4</sub>	250-315	15 TO 50





CONFIDENTIAL



KEY

- 1. PILOT-COMMANDER
- 2. NAVIGATOR-PILOT
- 3. ENGINEER-SCIENTIST
- 4. MAIN CHUTES
- 5. MAIN HATCH
- 6. MISSION MODULE
- 7. VERNIER ENGINE
- 8. MISSION ENGINE
- 9. OXIDIZER TANK (LOX)
- 10. S-BAND PARABOLIC ANTENNA
- 11. TOROIDAL FUEL TANK (LH)
- 12. FLAPS
- 13. RETROROCKET
- 14. ASTRO-INERTIAL PLATFORM
- 15. ATTITUDE NOZZLES
- 16. FUEL CELLS
- 17. VERNIER PROPELLANT TANK
- 18. ALTIMETER ANTENNA
- 19. INTER-MODULE PASSAGE
- 20. HEAT SHIELD

Fig. p-3. Model 410 Apollo Inboard Profile

CONFIDENTIAL



~~CONFIDENTIAL~~

CONTENTS

	Page
PART I: RADIATION ENVIRONMENT	
SUMMARY .....	R-vii
I RADIATION ENVIRONMENT .....	R-I-1
II RADIATION ENVIRONMENT WITHIN THE SPACECRAFT .....	R-II-1
III PROGRAM FOR EVALUATING RADIATION PROTON DOSE .....	R-III-1
IV PROGRAM FOR EVALUATING RADIATION DOSES FROM ELECTRONS AND BREMSSTRAHLUNG .....	R-IV-1
V SECONDARY PARTICLE RADIATION DOSE DUE TO PROTON NUCLEAR INTERACTIONS .....	R-V-1
A. GEOMETRY .....	R-V-1
B. PHYSICS .....	R-V-1
C. SPECIFIC REACTION TYPES .....	R-V-3
D. ANALYTICAL TERMS .....	R-V-7
E. EQUATIONS .....	R-V-11
VI RESULTS AND CONCLUSIONS .....	R-VI-1
VII BIBLIOGRAPHY .....	R-VII-1
VIII REFERENCES .....	R-VIII-1
PART II: METEORITE ENVIRONMENT	
SUMMARY .....	M-iii
I METEORITE ENVIRONMENT .....	M-I-1
A. PROBABILITY ANALYSIS OF METEORITE IMPACTS .....	M-I-1
B. PENETRATION EQUATIONS .....	M-I-6

~~CONFIDENTIAL~~CONTENTS (continued)

	Page
C. DETERMINATION OF REQUIRED SKIN THICKNESS . . . . .	M-I-13
D. DESIGN PROBABILITY OF NO PENETRATION. . . . .	M-I-14
E. METEORITE BUMPER CONCEPT . . . . .	M-I-15
F. HYPERVELOCITY IMPACT TESTS. . . . .	M-I-16
G. RESULTS AND RECOMMENDATIONS . . . . .	M-I-17
II REFERENCES . . . . .	M-II-1
III ILLUSTRATIONS . . . . .	M-III-1

~~CONFIDENTIAL~~

ER 12018

~~CONFIDENTIAL~~

R-v

## PART I: Radiation Environment

~~CONFIDENTIAL~~

ER 12018



~~CONFIDENTIAL~~

~~CONFIDENTIAL~~

ER 12018

## SUMMARY

An investigation has been conducted of the space radiation constituents to which Apollo will be exposed.

The approach to the radiation dose analysis involves using the basic structure and equipment for shielding, and analyzing the levels within the vehicle using this shielding in a position corresponding to the actual vehicle geometry. The detailed method of analysis separates the surface into a large number of sections, defines the materials and their thicknesses in each of the sections and determines the radiation transmission properties of the materials.

The emergent energy spectrum within the vehicle is found from the actual incident spectrum which enables the RBE to be determined. This analysis gives the dose rate, total dose, and dose distribution for any time during the mission, and facilitates the determination and positioning of spot shielding.

The stream of heavy particles, mostly protons, emitted from large solar flares presents the most critical radiation environment for the mission. The predictability of the severity and occurrence of these events is questionable; however, although thousands of solar flares are reported yearly, only a handful emit dose-significant numbers of protons. Although the event probably cannot be definitely established on a probability basis, there appears to be a good chance of reducing exposure to a critical event by scheduling flights during periods of reduced solar activity. The probability of exposure can be reduced approximately 2.4 times by using seasonal occurrence trends and by considering the grouped occurrences of these events. If the missions are flown during the minimal years of the sunspot cycle, the probability of exposure to a critically sized flare is reduced an additional five times.

The dose within three different command modules and within a radiation storm cellar has been determined.

Using as a model the severe event which followed the May 10, 1959 solar flare, the total incident proton dose within the final configuration is 67 REM based on utilization of the vehicle structure and equipment, jointly with spot shielding. As a result of the rapid decrease of dose with increasing absorber thickness, the shielding afforded by the command module equipment is very significant. It also is shown that detailed location of the equipment must be considered when analyzing the radiation within the vehicle. Variation in the spectral form is considered with regard to the resultant dosages.

A secondary neutron dose of about 2.5 REM is incurred during this event, giving a total combined dose of 70 REM. The probability of this happening has been estimated to be once per year during the solar cycle maximum, so the probability of occurrence during a 14-day mission is 0.037. Scheduling launchings during the quiet sun seasons of the solar cycle minimum reduces this probability to 0.003 (with values between 0.003 and 0.037, depending upon the sunspot cycle phase and upon random or scheduled flights).

~~CONFIDENTIAL~~

Using the data on the peak flux, energy spectrum and decay pattern for an intense event on July 14, 1959, the dose within the command module is 360 REM from protons and about 40 REM from neutrons. The probability of this occurring is about once in two years during the solar maximum or 0.018 for a 14-day mission. Applying the appropriate factors for scheduled launching, the probability of receiving this dose is 0.008 during a maximum year of the sunspot cycle and one-fifth this value during sunspot cycle minimum.

Detailed models of both regions of the Van Allen radiation have been prepared, and resulting proton and neutron doses are determined for a number of trajectories. The dose to the crew for any of the trajectories investigated lies between 0.06 and 0.63 REM from the inner Van Allen Belt protons. A neutron dose of 0.68 REM is incurred on the least favorable trajectory through the inner belt. The bremsstrahlung production from the Van Allen electrons along the least favorable trajectory lies between 0.4 and 2.0 REM.

A dose between 1.4 REM (during solar maximum) and 2.8 REM (during solar minimum) would be received on the 14-day Apollo mission from galactic cosmic rays.

The analyses indicate that normal mission radiation exposure totals between 2.2 and 9.4 REM, depending upon the flight date and the trajectory selected. An emergency condition (represented by a solar flare particle dose of 70 REM) will not have a probability greater than about 0.037 during solar sunspot cycle maximum.

~~CONFIDENTIAL~~

## I. RADIATION ENVIRONMENT

There has been no great increase in available data during the past six months, but a number of significant improvements in the detailed considerations and evaluations of the environment are now possible. This section, therefore, is an expansion of the physical models given in ER 11245M.

A far more realistic model of the Van Allen Belts has been developed using relationships developed by Yoshida, Ludwig and Van Allen (1960) which show that the position of the belt is related to the dip latitude and scalar intensity of the real magnetic field. In effect, the altitude of the belt varies approximately 800 km around the earth. The adiabatic invariant has also been noted to possess an improved physical basis for determining the structure of the trapped radiation. The theory and data given by Welch (1960) may offer a further improvement in locating the trapped particles.

Figure I-1 shows the position of the inner belt over the earth. This position is from the relationship found by Yoshida, Ludwig and Van Allen using an IBM 7090 program for a spherical harmonic fit to the magnetic field obtained by D. Jensen of the Air Force Special Weapons Center. The energy spectrum and particle fluxes were calculated using the experimental data of Freden and White (1960), Van Allen (1959) and Van Allen, McIlwain and Ludwig (1959).

Figure I-2 gives the basic form for the proton spectrum and the intensity near the lower boundary of the inner belt. Figure I-3 shows the contours of proton flux at one location. The experimental data have been extrapolated to include all protons above 20 Mev (below the cutoff region of the thinnest material of the vehicle).

Electrons in both inner and outer belts are the most abundant constituents of the trapped radiation. Spectral measurements of these particles have been made at only a few points at low altitudes. The energy spectrum again is complex and is much steeper above than below 100 Kev. In preparing a model of the electron distribution in the belts, spectral measurements of Holly (1960) and Walt, Chase, Cladis, Imhof and Knecht (1960), and the Anton 302 geiger counter data from a number of satellites and space probes (Van Allen, McIlwain and Ludwig, 1959; Van Allen and Frank, 1959a; Van Allen and Frank 1959b) were used.

Figure I-4 shows the form of the electron spectrum as derived by Dessler (1960) from the data of Walt, Chase, Cladis, Imhof and Knecht. This form is used in all regions where trapped electrons occur. The contours of electron flux (above 20 Kev) are shown for one location (Fig. I-5).

Some data on recent solar proton events have become available during the last six months. From this information, it appears the events following the

~~CONFIDENTIAL~~

flares on May 10 and July 14, 1959 still rank as extremes in intensity. Table I-1 shows data on solar proton events since May 10, 1959. Most significant is the variability of the energy spectrum with time, and the general flattening noted in some of the measurements. This effect is included in the analyses.

Information also has become available on the predictability of solar flare events. Anderson (1961) has shown their predictability to some extent, but for times far less than the 14-day Apollo mission, and even for short prediction times, the false alarm rate is fairly high.

The use of scheduled launchings to coincide with minimum seasons of solar activity was shown by Adamson (1961) to be quite promising. A further improvement in this technique is tentatively indicated in the findings of Goedeke (1961) which showed a regular movement in the solar activity seasons.

~~CONFIDENTIAL~~



Reference	Flare						Type III Polar Cap Absorption		Particle Measurements		Quantitative Data		Comments from Text		
	Date	Time (UT)			Location	Class	Location	Began	History	Location	Began	History		Spectral	
		Start(1)	Peak	End										Spectral	Temporal
Ney, Winckler and Freier Protons from the Sun on May 12, 1959, Phy. Rev. Lett. 8/15/59 V.3, N.4	5/10/59	2000 (10)			1st Quad- rant lat. 19° long. 50°	3+	College, Alaska	0100 (11)	Reached a value off scale and >17db. throughout latter part of day on 5/11 and up to at least 1700 on 5/12	Minn.	0200 (12) 1500 (12)	IGC-8 balloon reached peak altitude (10gm/cm <sup>2</sup> ) at 0530 (12) increase in vert. flux of 10 <sup>3</sup> C.R. bkgrd. giving an integral flux of 10 <sup>6</sup> / m <sup>2</sup> sec ster with R <sub>0</sub> 49BV. Forbush decrease at Minn. began 0300 (12) and peaked 0400 (12). " " balloon measurement at 0530 (12) was assumed to be near peak intensity of event (at Minn.) because of coinci- dence with Forbush peak.	N>R = 7500R <sup>-6.8</sup> R in BV and N increases rapidly with time after abrupt beginning of event; drops a factor of ten every four hours approximately exponentially with time derived N>E = 8.43 x 10 <sup>13</sup> E <sup>-3.8</sup>	Intensity de- creases rapidly with time after abrupt beginning of event; drops a factor of ten every four hours approximately exponentially with time derived I <sub>t</sub> = I <sub>0</sub> e <sup>-0.575t</sup> hours	
Winckler and Bhavsar Low Energy Solar Cosmic Rays and the Geomagnetic storm of May 12, 1959, JGR Sept. 1960 V.65, N.9	5/10/59	2055 (10)	2115 - 2150 (10)	0200 (11)	20°N 47°E	3+		0300 (11)	Continued to increase in intensity until 1600 UT on 5/11/59	Murmansk Geo. lat. 64°	1000 (11)  0400 (12) 1800 (12)	Rapid rise above C.R. bkgrd. above 50 gm/cm <sup>2</sup> . About a factor of 2 above C.R. bkgrd. @ 10 gm/cm <sup>2</sup> . Not observed at Moscow, 51° or at 41° geomag.  Number and exponent of energy spectrum decreased with time after reaching peak altitude. S.C. 2320 (11) coincident with world- wide Forbush decrease. De- crease reached bottom 0400 (12). Magnetic storm abated 2000 (12). 'K' index reached 9 for approximately 12 hours. "...it is clear that the low-energy C.R. appeared at Minn. only dur- ing terrestrial mag. storm. It is also certain that a continuous flux of these particles arrived at the polar cap beginning a few hours after the flare and continued in an interrupted but slowly decaying stream for more than 5 days."	N>E = CE <sup>-8</sup>  N>E <sub>105</sub> /cm <sup>2</sup> sec ster 51.5 = 2.47 x 10 <sup>9</sup> E <sup>-3.8</sup> 30.2 = 1.45 x 10 <sup>9</sup> E <sup>-3.8</sup> 10.9 = 1.23 x 10 <sup>6</sup> E <sup>-2.5</sup> 1.7 = 7.46 x 10 <sup>3</sup> E <sup>-1.8</sup>	peak 0539 (12) avg. 0539 - 0800 (12) avg. 0800 - 0940 (12) avg. 0940 - 1300 (12)	"... changes in the shape of the spectrum are a property of the geomagnetic field of the earth acting on the solar proton beam as it exists in free space. As far as we can tell, the polar cap effects continue without change, other than the steady decay during the period in which the geomagnetic storm produces the enormous increases ob- served at Minn."
Winckler, Primary Cosmic Rays. Presented at Radiation Research Society Symposium on Radiation in Space 5/10/60	3/11- 23/60 4/1/60 7/14/59 7/15/59									Pioneer V Mar. '60 Pioneer V 2000/4/60 Inferred 0600(14) Inferred 1100(15)	11-23 Mar. '60 Protons 40-500 Mev Protons 40-500 Mev Protons 40-500 Mev	2.5/cm <sup>2</sup> sec 30/cm <sup>2</sup> sec 5.5 x 10 <sup>6</sup> /cm <sup>2</sup> sec 6500/cm <sup>2</sup> sec			
Anderson and Enemark Observations of Solar Cosmic Rays Near the North Magnetic Pole, JGR Sept. 1960 V.65 N.9	7/16/59	2115 (16)	2129 (16)	0030 (17)		3+	College, Alaska	1 1/2 hrs. after peak 2250 (16)	Maximum effect was > 15 db. and enhanced absorption detectable until 1200 (19)	Resolute Bay 75°N 95°W	0200 (18) 0730 (19)	Peak altitude (6gm/cm <sup>2</sup> ) reached at 0330(18). Flux decreases generally in a steady manner unaffected by late magnetic storm ef- fects or by admission of protons south of Resolute Bay (as shown by riometer at King Salmon which in- dicated particles allowed and arriving between 0300 0700 (18))  Steady decrease with some plateaus (record goes to 1700(21))  Decrease plateaus and small rise after 1200 (24) (record goes to 2000 (24))  Particles still detected above C.R. bkgrd. at 1600 (27)	n(E)dE = E <sup>-4.5</sup> dE 85<E<400 0200 - 0400(18)  n(E)dE = KE <sup>-6.1</sup> dE 85<E<300 0130 - 0400(21)  General Expression where t>1.2 days following flare peak (2200 - 16) and 85<E<300MeV N(E,t) = 15 x 10 <sup>10</sup> t <sup>-3</sup> E <sup>-4</sup> part/cm <sup>2</sup> sec.  exponent seems to be constant to be constant sec ster @ 1.2 but substantial days (derived) changes not de- tectable late in event due to steepness and low intensity		

CONFIDENTIAL

Reference	Flare						Type III Polar Cap Absorption			Particle Measurements			Quantitative Data		Comments from Text							
	Date	Time (UT)			Location	Class	Location	Began	History	Location	Began	History	Spectral	Temporal								
		Start(1)	Peak	End																		
Ehmer, Erbe, Pfozner, Anger, and Brown Observation of Solar Flare Radiation and Modulation Effects at Balloon Altitudes July 1959 JGR V.65, N.9 Sept. 1960	7/10/59					3+										F(E)dE~E <sup>-3.6</sup> dE on 7/15/59 up to 400 Mev.						
	7/14/59					3+																
	7/16/59					3+																
Brown and D'Arcy Observation of Solar Flare Radiation at High Latitude during the Period July 10-17, 1959 Phys. Rev. Let. V.3n.8 10.15.59	7/10/59	0210 (10)				3+	College			*College Alaska	0210 (10) 0330 (10)	Flight 6 aloft between 37 and 10 gm/cm <sup>2</sup> at this time detected no protons					Determined from nascent portion of flight 13 assuming only protons  p/m <sup>2</sup> -sec-ster-Mev. 100-2400	Y-radiation also observed during flare increases as low as 200 g/cm <sup>2</sup> . Abs. coefficient 0.03 cm <sup>2</sup> /g indicating 3.5 Mev. Correcting for these does not appreciably alter slope of spectrum.				
	7/14/59	0342 (14)				3+			College Alaska	2300 (14) 0830 (15)	Balloon flight 13	N(E)dE = 6 x 10 <sup>-12</sup> E <sup>-4.5</sup> dE										
	7/16/59	2115 (16)				3+			College Alaska	2145 (16)	Flight 16 first detected particles at 2305 (16) at 30 gm/cm <sup>2</sup> . Intensity kept increasing and by 10 gm/cm <sup>2</sup> (~1 hr. later) 2400 UT (16) had risen to 3.5 x bkgrd level											
									*College Alaska	1240 (10)	Flight 7 was first to detect particles from this series of flares. This occurred at 1240 (10) @ 17 g/cm <sup>2</sup> and coincided with the Type III absorption at College.											
Anderson, Chasson, Liuechity and Suda Solar Cosmic Ray Outburst of May 4, 1960 JGR V.65, n.12 Dec. 1960	5/4/60	1015 (4)		1105 (4)		3 limb				Lincoln		Peak rel. increase 96%	Decay Law γ(min)e <sup>-t/T</sup> period of fit 17.5 ± 5.3 1040 - 1145	B(min)t <sup>-B</sup> period of fit								
										Lincoln		Peak rel. increase 135%										
										Deep River		Peak rel. increase 220%	15.4 ± 0.5 1042 - 1105	1.51 ± 0.05 1110 - 1150								
										Mt. Wash		Peak rel. increase 209%	16.7 ± 0.3 1041 - 1120	1.27 ± 0.02 1053 - 1315								
Brode, Brown, and Steiger Solar Flare Cosmic Ray Increase of May 4, 1960 JGR V.65, n.12 Dec. 1960	5/4/60	1020 (4)				2 limb				Berkeley	1030 rise 1039 peak 1100 return	Neutron monitors at 2 stations only Berkely showed increase which peaked at about 50% over pre-flux background										
										Makapiu Point, Hawaii	no var.											
VanAllen and Lin Outer Radiation Belt and Solar Protons Observations with Explorer VII during March-April 1960 JGR Sept. 1960 V.65, n.9	4/1/60	0845 (1)		1222 (1)			Thule	0945 (1)		Exp. VII	0830 (1) 1035 (1)	Increase flux occurred during the period 0933 - 1019 (1). Max. flux occurred 1019 - 1028 (1), 54/cm <sup>2</sup> sec on the 112 and 210/cm <sup>2</sup> sec on 302. ∴ integral energy spectrum Delay times 48 - 60 minutes 10Mev, 58; 20 - 41; 30 - 34; 40 - 29	E-2.6 18(E/30)	Δt-2.8 up to as much as 70 hrs. time at 1/2 intensity ~2 hrs.								
also VanAllen and O'Brien Progress Report on Investigation with SUI Apparatus on Exp. VII NASA News Release 60-184 April 29, 1960	Between 10/11/59 and 4/29/60 protons with E 30Mev were observed on 4 occasions by the Explorer VII counter														30 Nov. -	0.8/cm <sup>2</sup> sec.	1 April (1018 - 1028) (1203 - 1209) 2 April	60/cm <sup>2</sup> sec 14/cm <sup>2</sup> sec 0.8/cm <sup>2</sup> sec	17 March 17 March (1235-1243) 17 March	0.8/cm <sup>2</sup> sec 0.6/cm <sup>2</sup> sec 0.8/cm <sup>2</sup> sec	5 April 0706 5 April 0849 5 April 1033	0.6/cm <sup>2</sup> sec 4.0/cm <sup>2</sup> sec 4.0/cm <sup>2</sup> sec

CONFIDENTIAL

ER 12018

Reference	Flare						Type III Polar Cap Absorption			Particle Measurements			Quantitative Data		Comments from Text
	Date	Time (UT)			Location	Class	Location	Began	History	Location	Began	History	Spectral	Temporal	
		Start(1)	Peak	End											
Arnoldy, Hoffman, and Winckler Solar Cosmic Rays and Soft Radiation Observed at 5 x 10 <sup>6</sup> Km from Earth JGR, Sept. 1960 V.65, n.9	4/1/60	0830 (1)				3+				Pioneer V 5x10 <sup>6</sup> km Minn.		35/cm <sup>2</sup> sec, E>20 Mev  also balloon at Minn. 32/cm <sup>2</sup> sec E>20 Mev	E <sup>-3.5</sup> to E <sup>-4.0</sup> dE E>130	I = I <sub>0</sub> t <sup>-1.9</sup> (hrs)	2.6 x 10 <sup>-2</sup> R/hour
		No flare reported but noise storm at 1200 UT		18 flares in interval						5.9 x 10 <sup>6</sup> km		8 other small peaks of 0.2 - 2.0/cm <sup>2</sup> sec in period from 27 March - 6 April 1960			
also Arnoldy, Hoffman, and Winckler Solar Cosmic Rays and Soft Radiation Observation at 5,000,000 km from Earth NASA Release 60-185 4/29/60	4/1/60	0830 (1)								Pioneer V Minn.		Balloon flight M-38 detected particles to 400 Mev Spectrum and flux consistent with Pioneer V. Balloon was flown during severe mag. dist. from earlier flare.	N(E)dE CE <sup>-4</sup> dE above 40 Mev	I = I <sub>0</sub> t <sup>-1.9</sup> for 2 <sup>0</sup> large bursts	
VanAllen Observations of Solar Cosmic Rays, November 12 - 23, 1960 Presented at American Phys. Soc. 4/26/61, Wash., D.C.										Exp. VII 878 km 619 886 802 897 881 849		Time Long. Lat. 2330(12) -59.4 +44.4 0356(13) +112.5 -48.1 0230(14) -102.9 +46.7 2130(15) +135.2 -44.3 0240(18) -102.6 +50.4 0130(21) -90.3 +50.4 0042(23) -89 +50.4	Flux (cm <sup>-2</sup> sec <sup>-1</sup> ) 2.1 x 10 <sup>4</sup> 1.1 x 10 <sup>3</sup> 1.2 x 10 <sup>4</sup> 1.3 x 10 <sup>4</sup> 98 980 10		Detectors respond to protons >30 Mev and alphas >120 Mev.
VanAllen "Satellite Shows Wide Ray Threat" New York Times Sunday, Nov. 27, 1960									"Two weeks ago Explorer VII detected the most lethal outburst of solar radiation in its thirteen month lifetime."			Thirteen bursts were recorded in 13 months. The others varied from 10 to 210/cm <sup>2</sup> sec.	10 <sup>4</sup> /cm <sup>2</sup> sec. with E>20 Mev 50 Roentgen total for event		



## II. RADIATION ENVIRONMENT WITHIN THE SPACECRAFT

Much of the earlier research in this area has considered the radiation dose within a spherical vehicle or shield comprised of one or two uniformly distributed elementary materials. This choice of geometry, material and material distribution greatly simplifies the work, but gives a limited approximation to the actual situation because manned space vehicles are not hollow spheres of lead or aluminum. Also, early manned space vehicles are greatly limited in weight and volume, so the use of chambers to specifically shield against radiation may not be feasible.

Because of this, one of the first steps in providing radiation safety is to determine the shielding effects of the structure and other components of the actual spacecraft. This gives a detailed picture of the radiation from which to compare a number of alternate configurations with consideration to radiation dose. It also is possible to compare alternate materials and distributions for maximum protection. This information can be used to determine optimum placement of interior equipment and "spot" shielding against radiation. The basic features of the IBM 7090 shielding codes follow.

- (1) The vehicle surface is divided into a number of sections (448 for the Model 410) and represented as an area, distance and angle to a given interior dose measurement point. The geometrical analysis of the vehicle for the proton secondary program is different and is described later.
- (2) The radiation transmission properties of actual compound materials (such as cobalt-nickel-chromium-tungsten steel or nylon-phenolic ablator) are determined. These material properties are considered as different thicknesses for each section (20 materials in as many as 10 layers in each section). Remotely located materials in the aft modules are also considered.
- (3) Compound rather than simple energy spectra are used for each of the radiation constituents. These spectra can change form and intensity as functions of time and position.
- (4) The emergent energy spectrum (within the vehicle) is determined and an effective RBE is determined for each incident spectrum. This can be done for each area of the command module.
- (5) The dose rate, total dose and geometric dose distributions are calculated at any time or position or at mission termination. The dose distribution is useful in determining where the structure should be shielded to eliminate hot spots.

~~CONFIDENTIAL~~

- (6) Secondary neutron and gamma dose rates, doses and geometric dose distribution are computed.
- (7) By adding additional reaction production inputs we can do the same for other secondaries such as mesons.
- (8) The dose distribution through the human body at varying depths can be determined during the initial computations by considering the body as a number of layers of additional material. Because a limit of ten layers per run exists, a new computation using the vehicle-emergent spectrum as a man-incident spectrum is begun, and dose distribution over and within the body may be obtained in very great detail.

~~CONFIDENTIAL~~



### III. PROGRAM FOR EVALUATING RADIATION DOSES FROM PROTONS

The vehicle surface is divided into a number of small area elements  $dA$  (Fig. III-1). The number of protons ( $dN$ ) per square centimeter per second having an energy between  $E$  and  $E + dE$  and contained within a cone of solid angle ( $d\Omega$ ) incident on the area element ( $dA$ ) is determined from the proton differential kinetic energy spectrum

$$dN = F(E, t) dE d\Omega$$

where  $F(E, t)$  is the proton energy distribution function.

Range tables for a number of elementary materials of the spacecraft were used in the program (Aron, Hoffman and Williams, 1949, Rich and Madey, 1954). Proton range tables also were compiled for 10 compound materials of the spacecraft. A maximum of 10 different material layers can be considered in any calculation. Table III-1 shows the materials considered in the incident particle calculations.

The proton energy corresponding to a given incident energy after passing through a particular material is obtained from the tabulated range energy tables. Using a value  $E_i$  for the incident energy, the proton range  $R_i(M_{jj}', E_i)$  was determined. The residual range  $Y_{ij}(j')$  was then computed from the relation

$$Y_{ij}(j') = R_i(M_{jj}', E_{ij}(j'-1)) - L_{jj}'$$

where  $L_{jj}'$  is the actual thickness of material through which the proton passes for the  $j$  area element, and  $E_{ij}(j'-1)$  is the energy of the proton after passing through the preceding material. For the first material, this energy corresponds to the incident energy. The energy of the proton after passing through the material is determined by using the energy in the range-energy tables which corresponds to the residual range. This procedure was repeated for all materials and equipment.

The number of protons emerging with energy  $E_{ij}'$  is the same as the number which are incident with energy  $E_i$ , (neglecting straggling), so the number of protons incident with  $E_i$  which pass through the  $j$  area element and emerge with energy  $E_{ij}'$  is

$$dN_{ij} = F(E_i, t) dE d\Omega_j; E_{ij}'(E_i) > 0.$$

$$dN_{ij} = 0; E_{ij}' \leq 0.$$

The proton energy spectrum is determined by establishing up to 250 energy groups between the energies 0 and 700 Mev. When an emergent proton energy was computed, the energy group containing this emergent energy was ascertained, and the number of protons previously computed was added to that group. In this

~~CONFIDENTIAL~~

TABLE III-1  
Apollo Materials

<u>Code No.</u>	<u>Material</u>	<u>Code No.</u>	<u>Material</u>
1	Hydrogen	11	Foamed polyurethane
2	Carbon	12	Beryllium
3	Oxygen	13	Superalloy
4	Ablator, I	14	Fused silica
5	Insulator ADL-17	15	Equipment composite
6	Water	16	Copper
7	Glass phenolic honeycomb	17	
8	Aluminum	18	Components composite
9	Insulator Linde Super I	19	
10	Nylon-phenolic ablator, II	20	Lead

manner, the internal proton differential kinetic energy spectrum is obtained. The number of protons per square centimeter per second emerging with energy between  $E'$  and  $E' + dE'$  and contained within a cone of solid angle ( $d\Omega$ ) is

$$dN = KF' (E' t) dE' d\Omega .$$

If the dose rate corresponding to a proton flux of one proton per square centimeter per second is  $Q_P (E')$ , then the dose rate is

$$dD' = KF_1 (E', t) Q_P (E') dE' d\Omega .$$

~~CONFIDENTIAL~~

The exact nature of the function  $Q_p(E')$  depends on the radiation dose units used, but it generally measures the rate at which energy is deposited in some material. The dose rate was measured in units of RAD per second, so that

$$Q_p = \frac{1}{100\rho} \left[ \frac{dE}{dX} \right]_{\text{water}} \text{ rad/sec/proton/cm}^2\text{-sec}$$

where  $\rho$  is the mass density of water and  $\left[ \frac{dE}{dX} \right]_{\text{water}}$  is the energy deposited per centimeter of water, measured in ergs per centimeter.

This represents the dose rate measured by a small detector in the interior of the vehicle, resulting from protons passing through the area element  $dA$  and emerging with energy between  $E'$  and  $E' + dE'$ . The total radiation dose rate from primary protons measured by this detector is the sum of the dose rates from all area elements and proton energy increments. This summation is performed by integrating over all emergent proton energies and over the entire solid angle. By locating the origin of a coordinate system at a point in the vehicle interior where the radiation dose is computed, the integration over the solid angle can be transformed to an integral over the surface of the vehicle, by the relation

$$d\Omega = \frac{dA \cos \Theta}{r^2}$$

where  $r$  = the distance from the origin to the differential area element ( $dA$ )

$\Theta$  = the angle between the normal to  $dA$  and the line drawn from the origin to  $dA$ .

Thus, the total dose rate is

$$D' = \int_S \int_0^\infty K_F(E', t) Q_p(E') \frac{\cos \Theta}{r^2} dE dA$$

The value of the dose rate as a function of time can be obtained by numerical integration and then the radiation dose

$$D = \int_0^{t_f} D' dt$$

~~CONFIDENTIAL~~

can be evaluated using the time dependence given by the differential kinetic energy spectrum. For solar flare protons, the energy distribution function is represented by

$$F(E, t) = K E^{-a} \quad 0 \leq t \leq t_0$$

$$F(E, t) = K [C_1 (t-t_0) + 1]^{-b} E^{-a}; t \geq t_0$$

where  $t_0$  = the length of time during which the intensity is approximately constant  
 $t$  = the time in hours after the arrival of the initial proton flux. For example, the energy spectrum for protons arriving from the sun on 12 May 1959 was represented with the following values.

$$a = 4.8$$

$$b = 3/2$$

$$C_1 = 1$$

$$t_0 = 1$$

$$K = 9.39 \times 10^9 \text{ protons-mev}^{-4.8} / \text{cm}^2\text{-sec-mev-ster}$$

(peak value 5/12/59)

The constant  $a$  is approximately the same for most solar flare events, although the intensity measured by  $K$  is different. The values of  $t_0$  and  $C_1$  are not firmly established. Some data indicate that  $C_1$  should have the value  $1/24$  so time is effectively measured in days, and  $t_0$  should have a value of several days. There also is evidence of more rapid time decays of intensity, one giving a value of  $b = 2$  and another an exponential decay such that the intensity varies as  $e^{-0.575t}$ . The IBM programs are capable of handling complex spectra (up to 10 terms) which vary in time and space. This flexibility is incorporated even though current data do not call for this much detail.

~~CONFIDENTIAL~~

For the proton constituent in the inner Van Allen Belt, the basic proton differential kinetic energy spectrum shown in Fig. I-2 is represented by

$$dN = 0.117 K(a, \lambda, \phi) E^{-0.742} \quad 10 < E < 56.5 \quad \text{Mev}$$

$$dN = 0.808 K(a, \lambda, \phi) E^{-1.22} \quad 56.5 < E < 130 \quad \text{Mev}$$

$$dN = 4.387 K(a, \lambda, \phi) E^{-1.57} \quad 130 < E < 320 \quad \text{Mev}$$

$$dN = 52.42 K(a, \lambda, \phi) E^{-2.00} \quad 320 < E < 700 \quad \text{Mev}$$

where  $K(a, \lambda, \phi)$  is proton flux at an altitude  $a$ , latitude  $\lambda$  and longitude  $\phi$ . The values of proton flux are tabulated for the inner Van Allen radiation belt relative to a polar coordinate system the origin of which is located at the center of the inner radiation belt. The location of this origin varies in altitude and latitude as a function of longitude, in accordance with the real magnetic field of the earth. By connecting the trajectory program to the radiation program, the coordinates of trajectory points and the time interval between trajectory points are inputs to the radiation program. After the coordinates of a trajectory point are inserted, the value of the proton flux is determined from the tabulated values. Using this value for the proton flux, the radiation dose rate at that trajectory point is computed. From the dose rates at all trajectory points within the inner Van Allen radiation belt and the time interval between trajectory points, the radiation dose is evaluated by numerical integrations.

~~CONFIDENTIAL~~

~~CONFIDENTIAL~~

ER 12018



#### IV. PROGRAM FOR EVALUATING RADIATION DOSES FROM ELECTRONS AND BREMSSTRAHLUNG

The surface is divided into a number of small area elements as previously. The number of electrons ( $dN$ ) per unit area per unit time having energy between  $E$  and  $E + dE$  and contained within a cone of solid angle ( $d\Omega$ ) incident on an area element ( $dA$ ) located at the point ( $x, y, z$ ) is

$$dN = F(E, x, y, z, \alpha, \beta, t) dE d\Omega \quad (1)$$

where  $\alpha$  = the angle made by the axis of the cone with the normal to the area element  $dA$  at the point ( $x, y, z$ )

$\beta$  = the angle which the projection of the axis of the cone onto the area element makes with an arbitrary line tangent to the area element at the point ( $x, y, z$ ).

If the particle radiation is isotropic, the differential kinetic energy spectrum is independent of angles  $\alpha$  and  $\beta$ . The incident radiation is assumed to be isotropic for the present application, and the differential kinetic energy spectrum is a function of the spatial coordinates and time. For this case, Eq (1) is written in the form

$$dN = F(a, \lambda, \phi, t) dE d\Omega \quad (2)$$

where  $a$  = the altitude

$\lambda$  = the latitude,

$\phi$  = the longitude

$t$  = the time at which the vehicle is at these space coordinates.

The particles incident on  $dA$  enter the walls of the compartment. These particles which penetrate the walls emerge with an energy less than the incident energy. The amount of energy loss (neglecting straggling) can be determined by integrating the differential equation for the stopping power of the material. The energy transfer from the incident particle is possible because of ionization of the material, the production of Bremsstrahlung, nuclear transformation, pair production and/or fission.

The particle energy range here is limited to that for which electronic excitation (including ionization) and Bremsstrahlung production in the attenuating material are the dominant energy transfer interactions. Consequently, the particle energy dissipated per unit length of material transversed is

$$\left[ \frac{dE}{dx} \right] = \left[ \frac{dE}{dx} \right]_I + \left[ \frac{dE}{dx} \right]_B \quad (3)$$

~~CONFIDENTIAL~~

where  $\frac{dE}{dx}_I$  is the energy per unit length dissipated due to ionization and atomic excitation of the material and  $\frac{dE}{dx}_B$  is the energy per unit length dissipated due to Bremsstrahlung production in the material. The relative importance of these terms is often given by the approximate equation

$$\frac{\left[\frac{dE}{dx}\right]_B}{\left[\frac{dE}{dx}\right]_I} = \frac{EZ}{1600 mc^2} \quad (4)$$

where  $E$  = the energy of the particle

$m$  = the mass of the particle

$c$  = the velocity of light

$Z$  = the atomic number of the stopping material.

Thus, for incident particle energies which are small relative to the rest mass energy ( $mc^2$ ) of the incident particle, the Bremsstrahlung production is not significant.

Theoretical expressions have been developed for the energy dissipated per unit length of material traversed because of ionization and atomic excitation and because of the production of Bremsstrahlung. These expressions neglect straggling and are written as general relations

$$\left[\frac{dE}{dx}\right]_I = -G_I(E) \quad \text{and}$$

$$\left[\frac{dE}{dx}\right]_B = -G_B(E)$$

Using these relations, the total energy per unit length of material traversed dissipated by the incident particle is

$$\frac{dE}{dx} = -G(E)$$

where  $G(E) = G_I + G_B(E)$ .

The emergent particle energy, neglecting straggling, is determined by integrating this differential equation. If the actual thickness of material presented

~~CONFIDENTIAL~~

to the particles is  $T$ , then

$$\int_0^R dx = - \int_E^0 \frac{dE}{G(E)}$$

$$R = H(E)$$

where  $E$  = the incident particle energy

$R$  = the range of the electron in the material. For ionization and Bremsstrahlung losses, the Bethe-Heitler relationships are used. The electron energies are determined in the same manner as proton energies in the preceding section (from residual range after passing through the material).

The number of electrons which emerge with energy  $E_{1j}'$  are equal to the number which are incident with energy  $E_{1j}$ , neglecting straggling.

Thus, the number of electrons incident with energy  $E_1$  which pass through the  $j$  area element and emerge with energy  $E_{1j}'$  is

$$dN_{1j} = F(E_j, t) dE d\Omega_j; E_{1j}'(E_1) > 0$$

$$dN_{1j} = 0; E_{1j}' \leq 0. \quad (5)$$

The electron energy spectrum was determined by establishing up to 250 energy groups between 0 Kev and 3 Mev. When an emergent electron energy is computed, the energy group containing this emergent energy is ascertained, and the number of electrons as previously computed is added to that group. The internal electron differential kinetic energy spectrum is then obtained. The number of electrons per square centimeter per second emerging with energy between  $E'$  and  $E' + dE'$  and contained within a cone of solid angle ( $d\Omega$ ) again is

$$dN = K F'(a, \lambda, \phi, t) dE' d\Omega. \quad (6)$$

The radiation dose rate corresponding to a flux of 1 electron per square centimeter per second is represented by  $Q(E')$  so the radiation dose rate  $dD'$  from a single differential area element and from electrons with energy between  $E'$  and  $E' + dE'$  is

$$dD' = Q F'(a, \lambda, \phi, t) dE' d\Omega. \quad (7)$$

~~CONFIDENTIAL~~

The total particle radiation dose rate then is obtained by numerically integrating this expression over all energies  $E'$  and over the entire solid angle.

$$D' = Q(E') F' (a, \lambda, \phi, t) dE' d\Omega. \quad (8)$$

The quantity of energy per unit length of path traversed  $\frac{dE}{dx}_B$  deposited by the primary electrons is transformed to short wave length electromagnetic radiation. Because the relaxation length for very short wave length electromagnetic radiation in matter is usually much longer than the relaxation length for particles passing through matter, the electromagnetic radiation (bremsstrahlung) may contribute significantly to the radiation dose in the interior of the compartment. In the following discussion, the bremsstrahlung production is assumed to be radiated in the same direction (forward) as the radiating particle. For particles with relativistic energy, the bremsstrahlung radiation is nearly all radiated forward. This approximation is very good for particles with energy far greater than the rest mass energy of the particle.

The number of interactions  $W(\nu)$  per unit area per unit solid angle per unit length per unit time producing photons with a frequency between  $\nu$  and  $\nu + d\nu$  is described by

$$W(\nu) = \int_0^{E'(L)} \max N_0 \sigma(E', \nu) F' dE' d\nu \quad (9)$$

where  $N_0$  = the number of atoms per unit volume of stopping material

$F'$  = the number of electrons per unit area per unit energy per unit time with energy near  $E'$  as defined previously

$\sigma(E', \nu)$  = the cross-section for bremsstrahlung production of photons with frequency near  $\nu$

$L$  = the distance the particle has penetrated into the stopping material. The photons produced are emitted in the forward direction, and some are absorbed by the stopping material. The net change in number of photons per unit area per unit time per unit length per unit solid angle is

$$\frac{dn}{dL} + \mu n = W(\nu). \quad (10)$$

If no electromagnetic radiation is incident on the vehicle skin, the number of photons per unit area per unit time per unit solid angle at a depth  $L$  can be written

$$n = F_B(L, \nu, a, \lambda, \phi, t) \quad (11)$$

where  $F_B(L, \nu, a, \lambda, \phi, t) = e^{-\mu L} \int_0^L e^{\mu L'} W(\nu, E', L', a, \lambda, \phi, t) dL'$

~~CONFIDENTIAL~~

The electromagnetic radiation dose rate corresponding to a flux of one photon per square centimeter per second is represented by  $Q_B(\nu)$  so the electromagnetic dose rate  $dD'$  from a single differential area element and from photons with a frequency between  $\nu$  and  $\nu + d\nu$  is

$$dD'_B = Q_B(\nu) F_B(L, \nu, a, \lambda, \phi, t) d\nu d\Omega.$$

The total bremsstrahlung radiation dose rate is obtained by integrating this expression over all frequencies  $\nu$  and over the entire solid angle  $\Omega$ .

$$D'_B = \int_{\Omega} \int_{\nu_{\min}}^{\nu_{\max}} Q_B(\nu) F_B(L, \nu, a, \lambda, \phi, t) d\nu d\Omega. \quad (12)$$

Eq (8) represents the radiation dose rate received from particle radiation, and Eq (12) represents the radiation dose rate received from the resulting Bremsstrahlung radiation. The total dose rate ( $D'_T$ ) received is the sum of these two dose rates then is

$$D'_T = D' + D'_B. \quad (13)$$

The integrated radiation dose ( $D$ ) is determined by integrating Eq (13) over the time during which the vehicle is exposed to radiation.

$$D = \int_{t_0}^{t_f} D' dt \quad (14)$$

In evaluating this integral, the dose rate ( $D'$ ) represents the radiation dose rate from all sources. This integral can be transformed to an integral over the vehicle trajectory. If the position of the vehicle is  $r$ , the vehicle speed is

$$V = \frac{dr}{dt}$$

Eq (14) can be written:

$$D = \int_{r_0}^{r_f} \frac{D'}{V} dr \quad (15)$$

To evaluate this line integral, Eq (15) is integrated along the trajectory where  $r_0$  and  $r_f$  respectively are, the distance of the initial and final positions of the vehicle from the origin of the coordinate system.

~~CONFIDENTIAL~~

For the Van Allen Belt electrons, the differential kinetic energy spectrum shown in Fig. I-4 is represented by

$$dN = 1.041 \times 10^{-2} K(a, \lambda, \phi) E^{-1.1315}, 20 < E < 95 \text{ Kev}$$

$$dN = 2.233 \times 10^{-1} K(a, \lambda, \phi) E^{-0.8087}, 95 < E < 165 \text{ Kev}$$

$$dN = 2.486 \times 10^1 K(a, \lambda, \phi) E^{-1.7345}, 165 < E < 195 \text{ Kev}$$

$$dN = 2.041 \times 10^8 K(a, \lambda, \phi) E^{-4.749}, 0.195 < E < 3 \text{ Mev}$$

where  $K(a, \lambda, \phi)$  is the electron flux at altitude  $a$  latitude  $\lambda$  and longitude  $\phi$ . The electron fluxes were tabulated for the Van Allen Belts relative to a polar coordinate system positioned in the same manner as the proton fluxes. This radiation program also is connected to the trajectory program on the IBM 7090 and is evaluated in the same manner as the program for protons.

~~CONFIDENTIAL~~

## V. SECONDARY PARTICLE RADIATION DOSE DUE TO PROTON NUCLEAR INTERACTIONS.

### A. GEOMETRY

For the evaluation of radiation dose from secondary particles formed in the walls of the command module of a spacecraft, the geometry is determined differently. The analytical model consists of shells bounded by concentric ellipsoids of revolution; each shell defines a different material region. The geometrical configuration of the model is depicted in Fig. V-1. These surfaces are not necessarily parallel, but are specified to approximate actual bounding surfaces for the materials in a command module. Several variations desired of the material regions include: (1) cases where the thickness of a material region at the semiminor axis is less than or greater than the thickness at the semimajor axis and (2) cases where the vector  $A_1$  is not in the plane which contains the  $X' Y'$  axes. These geometrical cases are shown in Figs. V-2a through V-2d. The various equations for the computation of geometrical quantities for the above cases are given in Chapter V, Section E.

The number of numerical integrations to be performed over the variables  $\phi$ ,  $\cos \theta$  and  $r''$  will determine the number of secondary particle source points. These selected quantities are based on the configuration and vary with different configurations.

### B. PHYSICS

When charged particles pass through matter, one of several effects is nuclear interaction. The method discussed in this section concerns the formation of secondary particles by proton interaction with the nuclei in the walls of the command module of a spacecraft, and the computation of radiation dose inside the command module due to these secondary particles.

The proton radiation considered comes from solar flares and the Van Allen Belt. The solar flare proton energy flux is assumed to be distributed isotropically in outer space (this assumption also applies to Van Allen radiation). Protons are entering the surface of the command module in like proportions from all directions. In the computation of the volume source strength described in Chapter V, Section E, the summation over the incident angle  $\psi$  is accomplished by the IBM 7090 by accumulating the sum of proton fluxes within a large number of internal proton energy groups. Scattering of the protons on entering the material regions is negligible.

At the surface of the first encountered material region, the proton energy range and energy flux spectrum is that of the external proton radiation environment. After entering the first encountered material region, the proton energy range depends on the material and thickness encountered. An internal

~~CONFIDENTIAL~~

spectrum results, having a form different from the external spectrum, but the number of protons with external energies between  $E_0$  and  $E_0 + dE_0$  is equal to the number of protons with internal energies between  $E$  and  $E + dE$ . The proton spectrum and energies of protons within a material region are designated as the internal energy flux spectrum and the internal energies. The internal spectrum and energies are functions of the external energy; therefore, the external energy is used in the computation of both internal fluxes and energies.

A restriction on the proton energy is necessary for determining the acceptability of the proton flux of a particular proton energy group. Only those protons with energy capable of causing the nuclear reaction being considered are actually used in the dose rate computation. The energy of the proton at the surface or any point in a material region falls within the energy range covered by the reaction cross section for the particular nuclear reaction under consideration. The reaction cross section energy range is defined by  $(\epsilon_{\min})_m$  and  $(\epsilon_{\max})_m$ .

The external and internal proton energy grouping schemes are each divided into four intermediate energy ranges, each with a constant energy interval.

The internal proton energy is computed from the range energy relationship. Then, the internal proton energy group is determined, and the proton flux is tabulated for that energy group. The proton flux is accumulated until the  $j$ 's and  $\gamma$ 's are exhausted. This yields the total proton flux at each source point in the material regions. The energy-dependent data for that particular proton energy group is used jointly with the computed internal proton energy and flux in the group to compute the volume source strengths for each source point. The radiation dose rate is computed for each acceptable energy group and for a particular reaction in each material region. Energy grouping is discussed in Chapter V, Section C, "Energy Groups" subsection.

The external proton energy flux and external energies are used in computing the volume source strengths at the surface of the first encountered region. For all other volume source strength computations, the internal proton energy flux and energies are used. The volume source strength for an energy in a specific energy group at a particular point in the material region is used in computing the radiation dose rate from that particular point. The equations necessary for the computations are presented in Chapter V, Section E. The computation of radiation dose follows the general procedure stated below.

- (1) The first energy group and proton flux is determined.
- (2) The volume source strength for the energy which falls into the current energy group is computed for  $r''_m = 0$ .
- (3) The first term in the numerical integration over  $r''_m$  is computed.

~~CONFIDENTIAL~~



- (4) The current value of  $r''_m$  is increased by  $\Delta r''$  and the volume source strength for the energy which falls into the current energy group is computed.
- (5) The corresponding term in the numerical integration over  $r''_m$  is computed.
- (6) Steps (4) and (5) are repeated until  $r''_m = r''_{om}$ .
- (7) The final term in the numerical integration over  $r''_m$  is the first term in the numerical integration over  $\cos \Theta (\phi)$ .
- (8) The current value of  $\cos \Theta (\phi)$  is increased by  $\Delta \cos \Theta (\phi)$ .
- (9) Steps (2) through (8) are repeated until  $\cos \Theta (\phi) = 1.0$ .
- (10) The final term in the numerical integration over  $\cos \Theta (\phi)$  is the first term in the numerical integration over  $\phi$ .
- (11) The current value of  $\phi$  is increased by  $\Delta \phi$ .
- (12) Steps (2) through (11) are repeated until  $\phi = 2 \pi$ .
- (13) The final result is the radiation dose rate from the  $m^{\text{th}}$  material for the  $j^{\text{th}}$  proton energy group.
- (14)  $j$  is increased by 1 and steps (2) through (14) are repeated until all applicable energy groups have been considered.
- (15) The summation over the energy groups is performed yielding the dose rate from the  $m^{\text{th}}$  material region.
- (16) Steps (2) through (15) are repeated until the dose rate contributions from all the material regions have been computed.
- (17) The summation over the material regions is performed yielding the total dose rate.
- (18) The total dose is computed.

### C. SPECIFIC REACTION TYPES

In general, this method may be used to compute the radiation dose from secondary particles resulting from an A (a,b) B reaction, where A is the target nucleus, a is the incident proton, b is the emitted (secondary) particle, and B is the recoil nucleus.

~~CONFIDENTIAL~~

Currently of interest are the  $A(p, xn)B$ ,  $A(p, xp)B$  and the  $A(p, \gamma)B$  type reactions.

In the first reaction, a neutron or a number of neutrons (depending on the value of  $x$ ) may be emitted as secondary particles. The  $(p, n)$ ,  $(p, 2n)$  . . . . reactions are, in general, the dominant reactions for protons of energy greater than 1.0 Mev. The threshold energy for a  $(p, n)$  reaction with stable target nuclei always exceeds 0.78 Mev. Actually, the  $(p, n)$  threshold energies are very high for the light nuclei and the lighter intermediate nuclei. This threshold energy is used for establishing value on the minimum proton energy,  $(\epsilon_{\min})_m$ , which would be considered in the computation of volume source strength due to secondary neutrons formed by a  $(p, n)$  reaction. The maximum energy  $(\epsilon_{\max})_m$  to be considered also depends on the reaction being considered. The following examples describe the limiting energies  $(\epsilon_{\min})_m$  and  $(\epsilon_{\max})_m$  for the three types of proton-neutron reactions that may be considered.

Example 1:  $(p, n)$  reaction

How  $(\epsilon_{\min})_m$  is selected for this reaction is stated above. The selection of  $(\epsilon_{\max})_m$  is made by inspection of the plot of reaction cross-section versus proton energy.

Example 2:  $(p, 2n)$  reaction

Both  $(\epsilon_{\min})_m$  and  $(\epsilon_{\max})_m$  are selected upon inspection of the plot of reaction cross-section versus proton energy.

Example 3:  $(p, xn)$  reaction

Both  $(\epsilon_{\min})_m$  and  $(\epsilon_{\max})_m$  are selected upon inspection of the plot of reaction cross-section versus proton energy.

There are existing data which give the average energy of the secondary neutron particle and the value of  $x$  and  $(p, xn)$  reaction cross section. For a  $(p, n)$  or  $(p, 2n)$  reaction, the number of secondary particles is known, but the average neutron energy is generally not given and the method of computation is not firmly established. The average energy of secondary neutrons must be selected through available data and expected average neutron energies from the particular reaction being studied.

Protons with an energy below the threshold value produce only elastic scattering, inelastic scattering  $(P, P')$ ,  $(P, \gamma)$ , radiative captures and perhaps  $(P, \alpha)$  reactions. Of importance in this evaluation is the  $(P, \gamma)$  reactions where a gamma ray is emitted.

~~CONFIDENTIAL~~

In the  $A(P, \gamma)B$  reaction, a gamma ray is emitted in the transition of the recoil nucleus to the ground state. This process is important for protons with energies over 0.5 Mev. The reaction cross section is generally highly resonant, and if this is the case, only one proton energy will have a large value of reaction cross-section. Only a single proton energy is considered. To ensure a reaction, the quantities  $(\epsilon_{\min})_m$  and  $(\epsilon_{\max})_m$  are assigned values slightly below and slightly higher than the resonant proton energy. The energy of the gamma ray and the value of the reaction cross section are inputs determined from basic data. If the cross-section data for a  $(P, \gamma)$  reaction indicates a reaction similar to the  $(P, n)$  reaction, the selection of  $(\epsilon_{\min})_m$  and  $(\epsilon_{\max})_m$  is made in the same manner as for the  $(P, n)$  reaction.

The macroscopic reaction cross-section data for input will be prepared by

$$\Sigma_{mj} = f_w f_n \frac{\rho N_o}{A} \sigma_{mj} \times 10^{-24}$$

where

$f_w$  = weight fraction of the element in the material region

$f_n$  = the natural abundance of the isotope being considered

$\rho$  (grams/cu cm) = the density of the element being considered

$N_o$  = Avagadros' number ( $6.023 \times 10^{23}$  atoms/gram-atom)

$A$  = the atomic weight of the element being considered

$\sigma_{mj}$  = the macroscopic reaction cross-section in barns

$10^{-24}$  = the conversion from barns to sq cm.

The absorption cross-section data for input is prepared by using the following relationships.

For elements

$$\Sigma_{Rmj} = \frac{\rho N_o}{A} \sigma_{Rmj} \times 10^{-24}$$

where  $\sigma_{Rmj}$  = the microscopic cross section (barns) for the element being considered.

All other terms have been previously defined.

~~CONFIDENTIAL~~

For compounds

$$\sum R_{mj} = \rho_m \sum_{\mu} (f_w)_{\mu} (\sum R_{mj})_{\mu}$$

where

$$(\sum R_{mj})_{\mu} = \frac{N_0}{A} (\sigma R_{mj})_{\mu} \times 10^{-24}$$

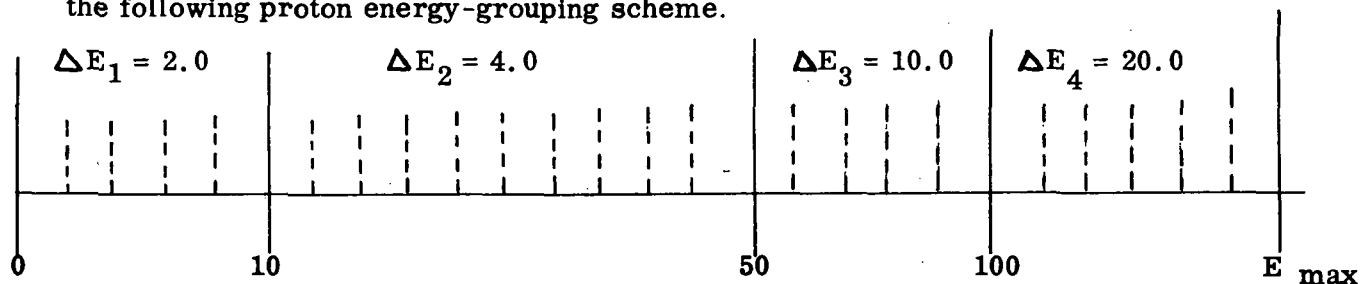
$\rho_m$  = the density (grams/cu cm) of the  $m^{\text{th}}$  material region

$(f_w)_{\mu}$  = the weight fraction of the element in the material region

subscript  $\mu$  denotes the  $\mu^{\text{th}}$  element in the material region.

All other terms have been previously defined.

Energy groups. Input data which are energy dependent are determined by the following proton energy-grouping scheme.



$\Delta E_1$  for  $J=1$  to 5

$\Delta E_2$  for  $J=6$  to 15

$\Delta E_3$  for  $J=16$  to 20

$\Delta E_4$  for  $J=21$  to 65 (The maximum number of energy groups)

The average energy of each proton energy group is computed by

$$\bar{E}_J = \frac{E_J + E_J + 1}{2.0}$$

The energy-dependent input data are determined for the average energy of the  $j^{\text{th}}$  energy group and listed accordingly.

The variable energy interval widths,  $\Delta E_1$ ,  $\Delta E_2$ ,  $\Delta E_3$  and  $\Delta E_4$  are set internally in the machine program. Application of the various energy interval widths depends on the value of  $J$  as shown above.

~~CONFIDENTIAL~~

## D. ANALYTICAL TERMS

<u>Algebraic Name</u>	<u>Definition</u>
$X', Y', Z'$	- The axes of the coordinate system of each elliptical surface the origin of which is at $0'$ .
$X, Y, Z$	- The axes of the coordinate system the origin of which is at the dose point, $0$ .
$\hat{i}, \hat{j}, \hat{k}$	- Unit vectors along the $X', Y'$ and $Z'$ axes, respectively.
$i$	- Subscript $i$ denotes the elliptical surface $i = 1, 2, 3 \dots, i_{\max}$ .
$0'$	- A point which is the center of a family of elliptical surfaces. It is also the origin of the "primed" coordinate system.
$Z'$ axis	- The axis of symmetry for all the ellipsoids. They are ellipsoidal surfaces of revolution about the axis. These surfaces all extend from the positive (or negative) $Z'$ axis downward (or upward) to a given value of $z_i$ along $Z'$ .
$\vec{A}_i$	- Vector in space measured from point $0'$ to a point on the $i^{\text{th}}$ elliptical surface extremity.
$\vec{B}_i$	- Vector in space measured from point $0'$ to point $0$ , the dose point.
$\vec{C}_i$	- Vector in space measured from point $0$ to a point in the $i^{\text{th}}$ elliptical surface extremity.
$\theta_i$	- Polar angle measured from the $Z$ -axis to a vector $r_{e_i}$ in space in the $X, Y, Z$ coordinate system for $i^{\text{th}}$ elliptical surface.
$\phi$	- Azimuthal angle measured from the $X$ -axis to a vector $r_{e_i}$ projected in the $X, Y$ plane of the $X, Y, Z$ coordinate system.
$\vec{r}_{e_i}$	- A vector measured from the origin $0$ to a point on the $i^{\text{th}}$ elliptical surface, (centimeters).
$m$	- Subscript $m$ denotes the material region $m = 1, 2, 3, \dots, m_{\max}$ .
$\vec{r}_m$	- A vector measured from the origin $0$ to a point in the $m^{\text{th}}$ material region, (centimeters).

~~CONFIDENTIAL~~

- $\vec{r''}_m$  - A vector measured from the outermost of two elliptical surfaces which defines the  $m^{\text{th}}$  material region to a source point in the direction of the origin 0 (centimeters).
- $r''_{om}$  - The magnitude of the difference between the vectors  $(r_e)_{i-1}$  and  $r_{e_i}$ , measuring the thickness of a material region for specific values of the angles  $\phi$  and  $\theta$  (centimeters).
- $\psi$  - Angle measured from the normal at the source point to the axis of the cone of solid angle at which the protons are entering the material region.
- $a_i$  - Semiminor axis of the  $i^{\text{th}}$  elliptical surface (centimeters).
- $b_i$  - Semimajor axis of the  $i^{\text{th}}$  elliptical surface (centimeters).
- $z_o$  - Displacement of the origin 0 along the  $Z'$  axis from the  $0'$  origin (centimeters).
- $x_o$  - Displacement of the origin 0 along the  $X'$  axis from the  $0'$  origin (centimeters).
- $y_o$  - Displacement of the origin 0 along the  $Y'$  axis from the  $0'$  origin (centimeters).
- $i_{\text{max}}$  - Total number of elliptical surfaces.
- $(T_2)_i$  - The distance perpendicular to the  $X'$  axis measured from the  $X'$  axis to the point on the  $i^{\text{th}}$  elliptical surface extremity (centimeters).
- $(T_4)_i$  - The distance perpendicular to the  $Z'$  axis measured from the  $Z'$  axis to the point on the  $i^{\text{th}}$  elliptical surface extremity (centimeters).
- $m_{\text{max}}$  - Total number of material regions.
- $E_o \text{ max}$  - Maximum energy of protons in the external energy flux spectrum (Mev).
- $E_o \text{ min}$  - Minimum energy of protons in the external energy flux spectrum (Mev).
- $K_k$  - Intensity normalization factor of protons in the external energy flux spectrum (protons per centimeter squared per second per Mev - Mev $^{-\alpha}$  - steradian).

~~CONFIDENTIAL~~



- $C_m$  - Exponent in the range-energy relationship for the  $m^{\text{th}}$  material region.
- $K_{1m}$  - Constant factor in the range-energy relationship for the  $m^{\text{th}}$  material region (grams per centimeter squared per Mev $^{-9}$ ).
- $\alpha_{k,t}$  - Exponent in the external proton-spectrum energy relationship.
- $\rho_{Dm}$  - Density of the material in the  $m^{\text{th}}$  material region (grams per cubic centimeter).
- $K_{2m,j}$  - Number of secondary particles per primary particle formed in the  $m^{\text{th}}$  material region by protons in the  $j^{\text{th}}$  energy group.
- $\Sigma_{m,j}$  - The reaction cross-section for protons in the  $j^{\text{th}}$  energy group for the  $m^{\text{th}}$  material region (centimeters) $^{-1}$ .
- $E_{Rm,j}$  - Average energy of the secondary particles formed by the protons in the  $j^{\text{th}}$  energy group in the  $m^{\text{th}}$  material region (Mev).
- $K_{3j}$  - Secondary particle flux-to-dose-rate conversion factor for the secondary particle energy corresponding to the  $j^{\text{th}}$  proton-energy group/RAD per hour per secondary particle (Mev) per centimeter squared per second).
- $R_{m,j}$  - Absorption cross-section for secondary particles in the  $m^{\text{th}}$  material region where the secondary particle energy corresponds to the  $j^{\text{th}}$  proton energy group (centimeters) $^{-1}$ .
- $\tau_o$  - The length of time during which the intensity is approximately constant (hours).
- $\tau$  - The length of time after arrival of the solar flare (hours).
- $d$  - The time constant which describes the decay of the proton intensity.
- $(\epsilon_{\text{max}})_m$  - Maximum energy of protons which are being considered for the nuclear reaction in the  $m^{\text{th}}$  material region (Mev).
- $(\epsilon_{\text{min}})_m$  - Minimum energy of protons which are being considered for the nuclear reaction in the  $m^{\text{th}}$  material region (Mev).
- $C_1$  - A constant selected to adjust the units on the times  $\tau$  and  $\tau_o$ , if units of hours are used,  $C_1 = 1$ , if days  $C_1 = 24$ .

~~CONFIDENTIAL~~

- $D_{mj}$  - Secondary radiation dose rate from the  $j^{\text{th}}$  energy group and  $m^{\text{th}}$  material region (RAD/hour).
- $(D_M)_m$  - Secondary radiation dose rate from the  $m^{\text{th}}$  material region (RAD/hour).
- $D_T$  - Total secondary radiation dose rate (RAD/hour).
- $D_{TT}$  - Total secondary radiation dose (RAD).
- $D_{m\ell j}$  - Secondary radiation dose rate from the  $\ell$  reaction for the  $j^{\text{th}}$  energy group and from the  $m^{\text{th}}$  material region (RAD/hour).

~~CONFIDENTIAL~~

## E. EQUATIONS

1. Secondary Particle Dose Rate Formed on the Surface of the First Encountered Material Region

The number of protons ( $dN(E_0)$ ) per square centimeter per second, having an energy between  $E_0$  and  $E_0 + dE_0$  are contained within a cone of solid angle ( $d\Omega$ ) incident on the surface of the first encountered material region as determined from the external proton differential kinetic energy spectrum

$$dN(E_0, \Omega) = K_k(E_0) e^{-\alpha_{kt}} dE_0 d\Omega$$

where

$$d\Omega = 2\pi \sin \psi d\psi$$

$$0 \leq \psi \leq \pi/2.$$

Integration over the variable  $\psi$  gives

$$dN(E_0) = 2\pi K_k E_0 e^{-\alpha_{kt}} dE_0.$$

This reduces to the following equation, which is the proton flux for an energy within the  $j$ th proton energy group.

$$N_{mj} = 2\pi K_k (\bar{E}_{oj}) e^{-\alpha_{kt}} (\Delta E)_j.$$

The limits on  $E_0$  are

$$E_{0\text{Min}} \leq E_0 \leq E_{0\text{Max}}.$$

The secondary particle volume source strength in units of Mev/cu cm - sec per  $j$ th energy group for the  $m$ th material region is

$$S_{vmj} = 2\pi K_k \sum_{mj} K_{2mj} (\bar{E}_{oj}) e^{-\alpha_{kt}} E_{Rmj} (\Delta E)_j.$$

The differential radiation dose rate due to secondary particles formed on the surface of the first encountered material region ( $m = 1$ ) is

$$dD_{mj} = \frac{1}{4\pi} K_{3mj} S_{vmj} e^{-\sum_{m=1}^{m\text{max}} \sum_{Rmj} r_{om}''} d[\cos \theta(\phi)] d\phi dr_m''$$

where the limits on  $\phi$  and  $\cos \theta(\phi)$  are

~~CONFIDENTIAL~~

$$0 \leq \phi \leq 2\pi$$

$$\cos [\Theta(\phi) \max] \leq \cos \Theta(\phi) \leq 1.0.$$

The above equation for the differential dose rate is numerically integrated to give the dose rate for the  $j^{\text{th}}$  energy group and the  $m = 1$  material region (at the surface).

The computation of  $S_{v_{mj}}$  is a direct procedure for this case, since no geometrical quantities are involved. In the computation of  $D_{mj}$ , the geometrical quantities involved are  $\phi$ ,  $\cos \Theta(\phi)$  and all of the  $r_{ei}$  for a particular value of  $\phi$  and  $\cos \Theta(\phi)$ . The computation of  $D_{mj}$  is performed by using the external proton energy selected for each  $j$  energy group for a particular point on the surface of the  $m = 1$  material region. The equation for  $D_{mj}$  is used to compute the first term required in the summation of radiation dose rate over the variables  $r_m''$ ,  $\cos \Theta(\phi)$  and  $\phi$  (actually it is the value of one of the contributors to dose rate for the case where  $r_{m-1}'' = 0$ ). It is possible that there may be no contribution from the surface for a particular  $j$  energy group because of no external energy falling into the energy group being considered.

## 2. Secondary Particle Dose Rate Formed Internally in the Material Regions or at the Surface of Internal Material Regions

Expressing the internal differential proton kinetic energy flux at a distance  $r_m''$  in the  $m^{\text{th}}$  material region necessitates deriving the internal flux spectrum from the external flux spectrum using the range-energy relationships. The range-energy relationships are applicable to a proton energy range from 1.0 Mev to 1000 Mev. The range corresponding to an external energy,  $E_0$ , in the  $m^{\text{th}}$  material region is

$$R(E_0) = K_{1m} (E_0)^{C_m}.$$

At any point in a material region, the energy is equal to the internal proton energy,  $E$ ; this is shown by

$$R(E_0) - \frac{\rho dm r_m''}{\cos \psi} = K_{2m} E^{C_m}$$

~~CONFIDENTIAL~~

where  $\frac{\rho_{dm} Y_m''}{\cos \psi}$  is equal to the distance that the external energy  $E_o$  has traveled. The difference between  $E_o$  and  $E$  is the energy loss by ionization. The relationship between  $E_o$  and  $E$  from the range equations is

$$E_{mj} = \left[ (\bar{E}_o)_j^{C_m} - \frac{\rho_{dm} Y_m''}{K_{lm} \cos \psi_j} \right] \frac{1}{C_m}$$

This equation is used to compute a value of  $E$ , at a particular point in a material region, other than on the surface of the first encountered material region which falls in a particular energy group. In the computation of volume source strength, the value of  $E$  must fall into the same energy group as the initial value of  $E$  for the case where  $\cos \psi_j = \cos \psi_{\max}$  which is the initial value of  $\cos \psi_j$ ; otherwise the energy used in the initial computation is decreased by the appropriate  $\Delta E$ , and the computation is repeated until the value of  $E$  falls into the same energy group as  $E$  of the initial computation. The computed energy  $E$  is stored for computation use when the particular energy group under which it falls is being considered. For the initial computation,  $E$  is determined by setting the value of  $E_{o_{\min}}$  equal to  $E_o$ , performing the computation, and testing for the energy group acceptability.

In the computation of  $E$  for  $m = 2, 3, \dots, m_{\max}$ , the emergent energy computed at the inner surface of each material region is used in the above equation to compute the internal energies for points in the next material region. This procedure continues until the emergent energy for the  $m-1$  material region has been computed. This emergent energy is used in the above equation to compute the internal energies at source points of interest. To achieve this, the emergent energies at the inner surfaces are stored for use in the computations when needed.

The internal differential proton energy flux expressed in terms of the external energy  $E_o$  for the  $m^{\text{th}}$  material region and the  $j^{\text{th}}$  proton energy group is

$$N_{mj} = 2\pi K_k (\bar{E}_{oj})^{-\alpha_{kt}} (\Delta E)_j (\Delta \cos \psi)_m$$

where the limits on  $\cos \psi$  are

$$(\cos \psi_{\max}) \leq \cos \psi \leq 1.0$$

$(\cos \psi_{\max})_m$  is computed from the following equation:

~~CONFIDENTIAL~~

$$(\cos \psi_{\max})_m = \frac{\rho_{dm} \gamma''_{om}}{K_{1m} \left[ (E_{\max})_{m-1}^{C_m} - (E_{\min})_m^{C_m} \right]}$$

where  $(E_{\min})_m$  is the cutoff energy; below this energy, the particular reaction under consideration cannot occur.  $(E_{\max})_{m-1}$  for  $m = 1$  is equal to  $E_{o_{\max}}$ .

For  $m = 1$ ,  $(E_{\max})_m$  is computed from

$$(E_{\max})_m = \left[ (E_{o_{\max}})^{C_m} - \frac{\rho_{dm} \gamma''_{om}}{K_{1m}} \right] \frac{1}{C_m}$$

and for  $m = 2, 3, \dots, m_{\max}$

$$(E_{\max})_m = \left[ (E_{\max})_{m-1}^{C_m} - \frac{\rho_{dm} \gamma''_{om}}{K_{1m}} \right] \frac{1}{C_m}$$

In the computation of  $N_{mj}'$ , the values of  $N_{mj}$  computed for the  $m^{\text{th}}$  material region and for all  $j$ , are used in the following manner.

- (1) The internal energy  $E_{mj} \gamma$  is computed for the current value of indices.
- (2) The energy group  $j'$  within which  $E_{mj} \gamma$  falls, is determined.
- (3) The values of  $N_{mj}$  are stored in a table for the particular  $j'$  energy group for the current value of index  $m$  and for a particular value of index  $\gamma$  at a particular source point.
- (4) The quantities  $N_{mj}$  in the table are accumulated whenever a particular value of  $j$  and  $\gamma$  causes  $N_{mj}$  to fall into the same  $j'$  energy group.
- (5) The result is a table which contains values of  $N_{mj}'$  for a particular source point.
- (6) This procedure is used to compute  $N_{mj}'$ , the internal proton flux for the  $j'$  energy group, for each source point in all material regions except at the surface of the first encountered material region.

~~CONFIDENTIAL~~



The volume source strength for the  $j^{\text{th}}$  energy group is then computed from the following:

$$S_{v_{mj'}} = E_{Rmj'} \sum_{mj'} K_{2mj'} N_{mj'}.$$

Since the equations for the computation of volume source strengths for a particular point in the  $m^{\text{th}}$  material region (and for each  $j^{\text{th}}$  energy group) have been stated both for points on the surface of the first encountered material region and for all other points in the  $m = 1$  material region, or for all points in the  $m = 2, 3, \dots m_{\text{max}}$  material region, the next step is to derive the dose rate equation.

The differential radiation dose rate from secondary particles formed in the  $m^{\text{th}}$  material region is expressed by the following:

$$dD_{mj'} = K_{3mj'} S_{v_{mj'}} \frac{dV_m}{4\pi(r_m)^2} e^{-\sum \frac{\text{mean free paths}}{\lambda}}$$

The volume element,  $dV_m$ , is equal to  $(r_m)^2 \sin \theta d\theta d\phi dr_m$ ; where  $r_m$  is the distance from the dose point to a point in the  $m^{\text{th}}$  material region at which the source strength  $S_{v_{mj'}}$  is located. By the use of the relationship  $r_m = r_{e_{i-1}} - r_m''$ , the direction of integration is reversed so that the volume source strength corresponding to the variable  $r_m''$  may be used directly in the dose rate equation.

The limits on  $r_m''$  are

$$r_{e_{i-1}} - r_{e_i} \geq r_m'' \geq 0$$

where

$$r_{e_{i-1}} - r_{e_i} = r_{om}''.$$

By reversing the limits, the minus sign in front of integral is cancelled and the limits on  $r_m''$  are

$$0 \leq r_m'' \leq r_{om}''.$$

~~CONFIDENTIAL~~

The total number of mean free paths for the secondary particles to get to the dose point is expressed as

$$e^{-\sum_l \text{mean free paths}} = e^{-\sum R_{mj'} r_m''} e^{-\sum_{m=1}^{m \max} \sum R_{mj'} r_{om}''}.$$

This expression is the attenuation of the secondary particles through all the remaining material regions.

The fully expressed equation for the computation of the differential radiation dose rate from secondary particles formed in the  $m^{\text{th}}$  material region by the  $j^{\text{th}}$  proton energy group is

$$dD_{mj'} = \frac{1}{4\pi} K_{3mj'} S_{Vmj'h} e^{-\sum R_{mj'} r_m''} e^{-\sum_{m=1}^{m \max} \sum R_{mj'} r_{om}''} dr'' d[\cos \theta(\phi)] d\phi$$

where the limits on  $\phi$ ,  $[\cos \theta(\phi)]_m$  and  $r_m''$  are

$$0 \leq \phi \leq 2\pi; \quad [\cos \theta(\phi)_{\max}]_m \leq [\cos \theta(\phi)]_m \leq 1; \quad 0 \leq r_m'' \leq r_{om}''.$$

The above equation is numerically integrated for the computation of  $D_{mj'}$ .

### 3. Total Radiation Dose Rate and Dose

The total dose rate from the  $m^{\text{th}}$  material region, due to secondary particles formed by protons within the prescribed proton energy range, is expressed by

$$(D_M)_m = \sum_{j=j \min}^{j \max} D_{mj}.$$

The total dose rate from all material regions due to secondary particles is expressed

$$D_T = \sum_{m=1}^{m \max} (D_M)_m.$$

The total dose determined by integrating over the time of duration of the solar flare is expressed by the following equations. The restrictions on their use are placed alongside each equation.

~~CONFIDENTIAL~~

$$D_{TT} = D_T \tau$$

$$j_0 \leq \tau \leq \tau$$

$$D_{TT} = D_T \frac{1}{C_1^{(d-1)}} \left\{ C_1^{(d-1)} \tau_0 + 1 - \left[ C_1 (\tau - \tau_0) + 1 \right]^{-d+1} \right\};$$

$$\tau > \tau_0 \quad d > 1.0.$$

#### 4. Computation of Geometrical Quantities

Computation of  $(r_e)_i$ . The equation of an ellipsoid displaced from the origin  $0'$  by  $x_0, y_0$ , and  $z_0$ , and having a new origin at 0 for the  $i^{\text{th}}$  elliptical surface is

$$\frac{(x_i + x_0)^2}{a_i^2} + \frac{(y_i + y_0)^2}{a_i^2} + \frac{(z_i + z_0)^2}{b_i^2} = 1.$$

The transformations from rectangular to spherical coordinates are:

$$x_i = r_{ei} \sin \theta_i \cos \phi$$

$$y_i = r_{ei} \sin \theta_i \sin \phi$$

$$z_i = r_{ei} \cos \theta_i.$$

Substitution for  $x_i, y_i$ , and  $z_i$  yields

$$r_{ei} = \frac{-B_i + \sqrt{B_i^2 - A_i C_i}}{A_i}$$

where

$$A_i = \left( \frac{\sin^2 \theta_i}{a_i^2} + \frac{\cos^2 \theta_i}{b_i^2} \right)$$

$$B_i = \frac{x_0 \sin \theta_i \cos \phi}{a_i^2} + \frac{y_0 \sin \theta_i \sin \phi}{a_i^2} + \frac{z_0 \cos \theta_i}{b_i^2}$$

~~CONFIDENTIAL~~

$$C_1 = \left( \frac{x_o^2}{a_1^2} + \frac{y_o^2}{a_1^2} + \frac{z_o^2}{b_1^2} - 1 \right).$$

Special cases. The computation of  $\left[ \cos \theta (\phi)_{\max} \right]_1$  (for the cases in Figs. V-2a and V-2b) follows.

From Fig. V-1, the vectors  $\vec{A}_1$ ,  $\vec{B}_1$  and  $\vec{C}_1$  can be expressed as:

$$A_1 = (\cos \phi \hat{i} + \sin \phi \hat{j}) \rho_1$$

$$B_1 = x_o \hat{i} + y_o \hat{j} + z_o \hat{k}$$

$$C_1 = \vec{A}_1 - \vec{B}_1$$

where

$$\rho_1 = a_1$$

For surfaces which extend down to  $z_1 = 0$  along  $Z'$ , where the extremity of the surface is in the plane which contains  $a_1$ .

$$C_1 = (\rho_1 \cos \phi - x_o) \hat{i} + (\rho_1 \sin \phi - y_o) \hat{j} - z_o \hat{k}$$

Applying direction cosines to determine  $\left[ \cos \theta (\phi)_{\max} \right]_1$  yields

$$\cos \left[ \theta (\phi)_{\max} \right]_1 = \frac{-z_o}{\sqrt{\rho_1^2 + x_o^2 + y_o^2 + z_o^2 - 2\rho_1(x_o \cos \phi + y_o \sin \phi)}}$$

The computation of  $\cos \left[ \theta (\phi)_{\max} \right]_1$  (for the cases in Figs. V-2c and V-2d) follows.

In Figs. V-2b and V-2c, the quantities  $(T_1)_1$  and  $(T_4)_1$  are inputs for a surface which is cutoff at some given value of  $z_1$  along  $Z$  rather than in the plane of the semiminor axis,  $a_1$ . As a result, the only change is in the quantity  $\rho_1$ . In this case,  $\rho_1 = \left[ (T_1)_1^2 + (T_4)_1^2 \right]^{1/2}$  and the preceding equation for  $\cos \left[ \theta (\phi)_{\max} \right]_1$  is applicable.

~~CONFIDENTIAL~~

### 5. Computation of Secondary Radiation Dose due to Van Allen Belt Proton Radiation

To generalize this method requires several changes in the data and in the manner of computing the secondary radiation dose rate and dose. The first change involves making the quantities  $K$  and  $\alpha$  time dependent;  $K_k$  is a function of the altitude, latitude and longitude;  $\alpha_k$  is a function of the altitude. Subscript  $k$  denotes the number of time intervals required as the vehicle proceeds along its trajectory. Values for both  $K_k$  and  $\alpha_k$  are obtained for print-out points,  $a_k$ ,  $\lambda_k$  and  $\Phi_k$  along the trajectory. The length of time,  $(dt)_k$ , in the proper time unit between printout points along the trajectory are also obtained from trajectory data.

The secondary radiation dose rate,  $(D_T)_k$ , is computed separately for each set of values of  $K_k$  and  $\alpha_k$ .

The average secondary radiation dose rate is then computed by

$$(\bar{D}_T)_k = \frac{(D_T)_k + (D_T)_{k+1}}{2}$$

The secondary radiation dose is computed by summing over all time intervals.

$$D_{TT} = \frac{1}{C_2} \sum_{k=1}^{k \max} (\bar{D}_T)_k (dt)_k$$

### 6. Computation of Secondary Proton Radiation - $(P \times P')$ Reaction

To compute the radiation dose rate due to secondary protons formed in the walls of a command module necessitates changing the method beyond the computation of  $E$  and  $N$  values. The method to be used is described below.

The computation of the  $E$  and  $N$  values for the primary protons is stated in Chapter V, Section E. The average energy of secondary protons,  $E_R$ , results from a particular  $j'$  energy group within which the  $E$  value falls; however, the secondary proton energy most probably falls within an energy group less than the  $j'$  group. First, it is necessary to determine the  $j''$  energy group within which  $E_R$  falls. By using the following equations, the value of the secondary proton energy at the innermost surface is determined.

~~CONFIDENTIAL~~

$$E_{R_{mj}''j'''} = \left( E_{R_{mj}''}^{Cm} - \frac{P_{dm} r_m''}{K_{lm}} \right)^{1/Cm} \quad (16)$$

The  $j'''$  corresponds to the energy group within which  $E_R$  falls after ionization of the secondary proton as it passes through the remainder of the region of origin. The expected value of  $r''$  depends on the location of the source point. That is, if the source point considered is located at the second source in the first region, then  $r''$  is determined from

$$r_{m,2}'' = r_{om}'' - r_{m,1}''$$

The energy value computed by using Eq (16), is used in

$$E_{R_{mj}''j'''} = \left( E_{R_{mj}''}^{Cm} - \frac{P_{dm} r_{om}''}{K_{lm}} \right)^{1/Cm} \quad (17)$$

Equation (17) is used to compute the energy at the innermost surface, unless the region which is being considered is the last region, then Eq (16) is used alone.

The flux value corresponding to  $E_{R_{mj}''j'''} is then computed from$

$$N_{R_{mj}'} = N_{mj'} \cdot K_{2_{mj'}} \sum_{mj'} (\Delta r'')_m$$

This secondary proton flux value is then placed in a  $j''''$  table. The location within the table is determined by finding what  $j''''$  the  $E_R$  value at the innermost surface falls within.

The differential secondary proton radiation dose rate is expressed

$$dD_{mj'} = N_{R_{mj}'} \cdot K_{3_{mj'}} d(\cos \theta) d\phi dE$$

Integration of the above equation is performed numerically to determine the dose rate from all regions and energy groups. The radiation dose computation is performed in the same manner as prescribed for the (P,  $\gamma$ N) reaction.

~~CONFIDENTIAL~~

## VI. RESULTS AND CONCLUSIONS

Before proceeding to the results, it may be worthwhile to discuss some important effects of the energy spectrum form. The experimental data obtained so far cover small portions of the energy spectrum of these particles and required considerable interpolation and extrapolation to yield a more comprehensive distribution.

As an example, the peak flux measurement of solar protons on May 12, 1959 indicated approximately 51.5 protons/sq cm-sec-steradian with energies of at least 105 Mev, and an integral spectrum varying with energy to the  $-3.8$  power. Extrapolating this relationship to 20 Mev (below the cutoff energy of the thinnest material layer in either the L2C, M-1-1 or Model 410 configurations), a value of  $2.812 \times 10^4$  protons/sq cm-sec-steradian with energy of at least 20 Mev is obtained.

Returning to the case of a hollow aluminum sphere, Fig. VI-1 shows how the spectral distribution of these particles would affect the dose. The ascending portion of the curves is determined because aluminum which is thinner than approximately 0.6 gm/sq cm (the range of a 20 Mev proton in aluminum) retards the particles without stopping any of them. The less energetic particles are more efficient in depositing energy and yield an increased dose. For approximately 0.8 gm/sq cm, the dose is the same for each spectrum; for 10 g/sq cm, the steepest spectrum ( $a = 5.5$ ) deposits about 1/10 the dose of the flattest spectrum ( $a = 4.0$ ); and for 100 g/sq cm, this difference increases by another order of magnitude.

This illustrates quite clearly that the same total number of particles can produce very different radiation dosages, depending upon how this number is distributed with energy. To evaluate the effect of assuming different spectral forms of the measured data from the event of May 1959, the spectra is standardized to the measured flux of protons approximately between 110 and 220 Mev. The effect of this is shown in Fig. VI-2. The total number of particles above 20 Mev now differs, and the effect is most evident at small absorber thicknesses. Fig. VI-2 shows that small changes in the spectral distribution of the particles are insignificant to the dose within absorber thicknesses anticipated in early manned vehicles (approximately 8 to 10 g/sq cm).

Returning to the first two configurations under examination, the average dose from the proton event following the flare of May 10, 1959 would have been 37.51 RAD within the aft cone L2C (similar to the Mercury capsule) command module and 31.1 RAD within the forward cone M-1-1 command module. Flux was assumed constant for 29 hours before peak flux measurement and after this it decayed as a  $t^{-3/2}$  exponential.



~~CONFIDENTIAL~~

At that time, it was not possible to consider detailed placement and composition of equipment within the command module. The calculations considered equipment of a composite material distributed uniformly over the interior surface of the vehicle. The internal equipment, whose weight is about that of the structure, will greatly affect the radiation dose the crew receives. Omitting the equipment results in an average dose of 1306 RAD and 397 RAD within the L2C and M-1-1 vehicles, respectively. The basic difference in radiation protection between the two configurations is difficult to detect when the internal equipment is included. This arises primarily from the logarithmic decrease of dose versus absorber thickness seen in both of the last figures.

The IBM 7090 program for each configuration also was run for the other previously discussed spectra, and for two compound spectra with the form of the spectrum changing below 100 Mev (as indicated in some preliminary data from the solar events of Autumn 1960). The results of these calculations are summarized in Table VI-1. The second and fourth data columns show large differences between the two early configurations. The Mercury shape gives consistently higher doses because of protons through the forward quadrants which do not have much absorbing material. The heat shield for this design is on the aft bulkhead. The M-1-1 design has its heat shield primarily on the front and forward sides. The heat shield on the back of the L2C is largely wasted for radiation attenuation because that region already contains the mission module, tanks, fuel and engine assemblies. The L2C design also shows greater sensitivity to changes in the spectral characteristics of the particles (an increase of 6 times from  $a = 4.0$  to  $a = 5.5$  as contrasted to a factor of 2.5 for the other design). Introducing the command module equipment (columns 1 and 3) gives almost equal doses between the two configurations, but there is a large implicit error in assuming the equipment as a uniform smear. This will be discussed later. Variations in the spectral form are far less significant when the 4 gm/sq cm of equipment are included (column 3). This also could have been seen by the convergence of the curves of Fig. VI-2 at thicknesses below 10 gm/sq cm. The table also shows the results of an analysis to determine the dose inside the mission module storm cellar. At this point, the crew is heavily shielded both front and back by the command module and the massive tanks and propellants, respectively.

The calculations show that the dose decreased from 59.2 RAD to 12.5 RAD to 3.54 RAD as aluminum weights of 500 and 1000 and 2000 pounds were wrapped in the form of an open-ended cylinder within the mission module. The positioning of this radiation storm cellar is shown in Fig. III-1. Its axis coincides with the primary axis and its dimensions are 46 inches in diameter and 65 inches long. This analysis did not consider onboard equipment or material in the mission module, so allowance can be made for this by reducing the aluminum shield plates by 350 pounds. It appears that the mission module storm cellar is feasible.

~~CONFIDENTIAL~~

TABLE VI-1  
Summary of Dose by Configuration

PROTON DIFFERENTIAL SPECTRUM	DOSE INSIDE FORWARD CONE COMMAND MODULE (M-1-1)		DOSE INSIDE AFT CONE COMMAND MODULE (L2C)		DOSE INSIDE MISSION MODULE STORM CELLAR (WITHOUT MISSION MODULE EQUIPMENT)		
	WITH EQUIPMENT *	WITHOUT EQUIPMENT	WITH EQUIPMENT *	WITHOUT EQUIPMENT	PLUS 2000 LB A1	PLUS 1000 LB A1	PLUS 500 LB A1
E <sup>-2.5</sup> @ 20 - 100 MEV			18.96				
E <sup>-4.8</sup> @ 100 - 700 MEV			11.51 30.47				
E <sup>-3.5</sup> @ 20 - 100 MEV			21.66				
E <sup>-4.8</sup> @ 100 - 700 MEV			11.51 33.17				
E <sup>-4.0</sup> @ 20 - 700 MEV		203	28.65	508			
E <sup>-4.5</sup> @ 20 - 700 MEV		308	33.85	915			
E <sup>-4.8</sup> @ 20 - 700 MEV	31.1	397	37.51	1306	3.54	12.5	59.2
E <sup>-5.0</sup> @ 20 - 700 MEV		469	40.15	1655			
E <sup>-5.5</sup> @ 20 - 700 MEV		718	47.79	3015			

\*4 GM/CM<sup>2</sup> UNIFORMLY DISTRIBUTED

INTERIOR PROTON DOSES (RAD) FOLLOWING THE SOLAR FLARE ON  
MAY 10, 1959. (E<sup>-4.8</sup>), FOR OTHER SPECTRA, THE DATA ARE STANDARDIZED  
TO THE FLUX OF PROTONS BETWEEN THE MEASUREMENT INTERVAL OF  
110-220 MEV.

~~CONFIDENTIAL~~

From this, the command module or re-entry portion of a modular manned lunar spacecraft appears to offer considerable protection against the radiation from solar flare protons, and proper positioning of equipment within the command module offers further protection to the crew.

For finer examinations the dose per unit solid angle for each of the area elements of the two configurations, omitting the equipment, was calculated (Figs. VI-3 and VI-4). The positional variation of dose is very large in both configurations - - six orders of magnitude in the M-1-1, and almost seven in the L2C configuration. Most of this is caused by the extremely small doses coming through the mission module. These figures also show the regions which contribute to the much larger dose within the L2C and the relative inefficiency of the aft mounted heat shield.

Returning to the computer input data, the exact material thicknesses and angle-to-dose point can be found and used to determine equipment positioning to reduce the dose. Of course, it is not possible to position equipment in a manner optimum for radiation safety, but spot shielding in proximity to the crew then is used to shield any remaining hot spots.

An alternative to this course is the radiation storm cellar previously mentioned. The dose distribution inside this cylinder is shown in Fig. VI-5. The numbers are omnidirectional dosages (the dose that is received if corresponding absorber thickness occur over the entire surface) and should be divided by  $4\pi$  for comparison with Figs. VI-3 and VI-4. The absorber thicknesses through the command module, applicable to forward angles 0 to 55 degrees, include the command module equipment. This adds more than 8 gm/sq cm everywhere in this sector, because the equipment is seen twice by the penetrating proton and at an angle large enough that its effective thickness is increased.

It is not possible to choose between the storm cellar and the command module until the most efficient command module layout is made, but it appears that pound-for-pound spot shielding in the command module is more efficient than the mission module storm cellar. This cylinder also will be rather cramped quarters for three men for a period of a day, and it is very unlikely that the crew will be able to perform any duty functions while in such a storm cellar.

Previously, we have used the RAD unit for dosage measurement, but the most widely used unit for expressing the biological dose is the REM, although it is far from ideal. The RBE, a conversion factor from physical to biological dose for protons, is related to the energy deposition rate, and is a function of the particle kinetic energy. To determine the RBE, the emergent energy spectrum is calculated. This is shown in Fig. VI-6 for the M-1-1 configuration (including equipment as a uniform 4 gm/sq cm). Table VI-2 shows the RBE by emergent energy groups and the weighted average RBE for the entire emergent spectrum. The two RBE evaluations used are shown and referenced in the table. It is emphasized that the RBE inside the command module is far less than it would be for a recoil proton spectrum, as near a reactor.

~~CONFIDENTIAL~~

TABLE VI-2

## RBE of Solar Protons Within M-1-1 Command Module

Energy (Mev)	% of Total No. Particles	RBE*	(RBE) x (%)
> 14	91.26	1	91.26
14-13	1.104	1	1.104
13-12	0.777	1.02	0.793
12-11	0.922	1.05	0.968
11-10	0.954	1.1	1.049
10- 9	0.796	1.16	0.923
9- 8	0.727	1.27	0.923
8- 7	0.641	1.44	0.923
7- 6	0.604	1.65	0.997
6- 5	0.543	1.90	1.032
5- 4	0.649	2.22	1.441
4- 3	0.447	2.67	1.193
3- 2	0.288	3.30	0.950
2- 1	0.185	4.47	0.827
1- 0	0.108	8.5	0.918
Total	100.005		105.301
	Mean RBE		1.05

Energy (MEV)	% of Total No. Particles	RBE**	(RBE) x (%)
≤ 50	51.63	1.0	51.63
> 50	48.37	5.0	241.85
Total	100.00		293.48
	Mean RBE		2.93

\* International Recommendations on Radiological Protection, Brit. J. Radiol., 1951, 1954, 1955, as cited in Radiation Shielding, by B. T. Price, C. C. Horton and K. T. Spinney, Pergamon Press, New York 1957

Proton Radiation Hazards in Space, by H. J. Schaefer, Astronautics, February, 1961

\*\* C. A. Tobias, quoted in Proceedings of Conference on Radiation Problems in Manned Space Flight, NASA TN D-588 December, 1960

Total Emergent Particles =  $9.216 \times 10^2 / \text{Cm}^2 \text{Sec}$

Total Incident Particles =  $3.532 \times 10^5 / \text{Cm}^2 \text{Sec}$

~~CONFIDENTIAL~~

The third configuration analyzed was the Model 410. This design is basically similar to the M-1-1 command module but has a heavier heat shield. On that basis, an anticipated reduction in dose to about 2/3 of the 31.1 RAD found for the earlier configuration is expected, but the initial calculation made for the Model 410 gave 75.03 RAD, an increase of 2.5 times over the M-1-1. The reason for this increase became apparent after examining the individual areas. The Model 410 dosage calculations were made with the command module equipment actually positioned according to the inboard profile. The large dose came from regions where there was no equipment other than wires. These regions around the top surface also were far enough aft to have relatively little heat shield, and high dosages were noted for a few regions through the aft bulkhead. Although the regions with equipment generally had more than 4 gm/sq cm, the dose was controlled by the areas without equipment. This is a consequence of the logarithmic decrease of dose with absorber (Fig. VI-2). This may be visualized by considering two areas of 8 gm/sq cm each with equal doses through them. Removing 4 gm/sq cm from one and adding it to the second increases the first dose 5.9 times and decreases the second dose 2.83 times (a net increase by a factor of 3.1). The significance of the results for the Model 410 are twofold. First the calculations made with equipment or any of the materials uniformly smeared are just poor approximations. Second, unless the calculation procedure is capable of handling the detail of the configuration any results may be grossly in error.

Spot shielding and repositioning of equipment can be used to reduce the dose within the Model 410 command module. Temporarily, an approach to determine the amount of shielding required to reduce the dose by a factor of two was chosen. This is achieved most efficiently in proximity to the crew. It can be achieved by adding from 2.86 to 5.44 g/sq cm over the solid angle which subtends 56 of the original areas. A total of 94.1 pounds was sufficient to reduce the dose to 33.73 RAD. The initial dose distribution over the surface of the Model 410 command module is shown in Fig. VI-7. The reduced doses using spot shielding also are shown as inserts on the same figure. Fig. VI-8 and Table VI-3 show, respectively, the Model 410 emergent energy spectrum and RBE. Table VI-4 summarizes the most important features which the early configurations showed as well as the dosage numbers for Model 410. The dose an unprotected man receives (assuming that particle cut off below 20 Mev) also is shown for comparison.

The next step is to determine an optimum layout of command module equipment to further reduce the dosage and dosage variations and eliminate some spot shielding.

The previous dosage values apply to the total dose measured within the vehicle at an altitude of about 30 km (where the balloon measured data was obtained). To account for the shadow effect of the earth these values should be multiplied by 1.8. (The atmospheric cut off of approximately 100 Mev already has been taken into account by extending the measured spectrum below the energy necessary to penetrate the thinnest layer of the spacecraft.)

~~CONFIDENTIAL~~

TABLE VI-3

## Proton RBE Within 410 Command Module

## Solar Flare Particles

Energy (Mev)	% of Total No. Particles	RBE	(RBE) x (%)
> 14	86.845	1	86.845
14-13	1.113	1	1.113
13-12	1.476	1.02	1.505
12-11	1.551	1.05	1.629
11-10	1.561	1.10	1.717
10-9	0.487	1.16	0.565
9-8	1.355	1.27	1.721
8-7	1.526	1.44	2.197
7-6	1.293	1.65	2.133
6-5	0.620	1.90	1.178
5-4	0.321	2.22	0.713
4-3	0.826	2.67	2.205
3-2	0.462	3.30	1.525
2-1	0.362	4.47	1.618
1-0	0.200	8.5	1.700
Total	100.00		106.664
	Mean RBE		1.07

 $3.532 \times 10^5$ /sq cm-sec

Total Incident Particle Flux

 $8.803 \times 10^2$ /sq cm-sec

Total Emergent Particle Flux

0.25%

Emergent Flux / Incident Flux

TABLE VI-4

Radiation Dose From Solar Protons Following Class 3+ Flare on May 10, 1959

	Unprotected Man	Within L2C	Within M-1-1	Within Model 410
Without Command Module Equipment	18,009 RAD	1306 RAD	397 RAD	
With Command Module Equipment Uniformly "Smeared"			31.1 RAD	
With Equipment Actually Positioned				75.03 RAD
With Spot Shielding				33.7 RAD

ER 12018

~~CONFIDENTIAL~~~~CONFIDENTIAL~~

It appears that a non-incapacitating dose of about 35 (RAD) X 1.05 (RBE) X 1.82 (free space correction) = 67 REM is received by the crew in the Model 410 command module from a flare event similar to the flare of May 10, 1959. Although this is one of the largest flare events ever recorded, doubt still remains as to where this event actually ranks in frequency of occurrence.

In ER 11245M a design criterion procedure was developed to give the details of dose vs probability vs mission length vs absorber. The use of this procedure is limited by input data on the events themselves and the numbers shown are only for illustration. There still are not enough data to properly use the IBM program and it is necessary to evaluate the hazard on a discrete-event basis.

Of the five documented events reported in ER11245M, only the event following the flare of July 14, 1959 had a larger measured flux than that from the May 10, 1959 flare. Better data from both of these events currently is available, and have already used this new data on the May event in the calculations. For the July event, Winckler (Table I-1) has deduced the free space peak flux of protons as  $N = 5.5 \times 10^6/\text{sq cm-sec}$ ;  $40 \leq E \leq 500$  Mev.

The kinetic energy exponent for this event is given as,  $a = 4.5$ . Extending this to 20 Mev gives an integral unidirectional flux of

$$N = 4.95 \times 10^6/\text{sq cm-sec-steradian}, E \geq 20 \text{ Mev.}$$

Brown and D'Arcy have measured the spectrum for this event after 17 hours (Table I-1) as

$$N(E) dE = 6 \times 10^8 E^{-4.5} dE \quad 100 \leq E \leq 400 \text{ Mev.} \\ \text{protons/sq cm-sec-steradian-Mev.}$$

The flux given by Winckler gives

$$N(E) dE = 6.1 \times 10^{12} E^{-4.5} dE.$$

It appears this event as measured at Minneapolis and College, Alaska, had a very rapid decay with time, so a slower decay pattern given by Winckler ( $t^{-2}$ ) is used for a more pessimistic estimate. Using these data as a base, the dose within the Model 410 command module is estimated as 360 REM.

Table I-1 also shows the event of July 16, 1959 (the last of three July 1959 events) which Anderson and Enermark approximate as

$$N(E, t) = 15 \times 10^{10} t^{-3} E^{-4}, \quad 85 \leq E \leq 300 \text{ Mev., } t \geq 1.2 \text{ days} \\ \text{Particles/sq cm-sec}$$

The flux of protons above 20 Mev at  $t = 1.2$  days after the flare peak equals  $4.32 \times 10^4$  protons/sq cm-sec-ster,  $E \geq 20$  Mev. This is 1.53 times greater than the peak flux of May 10, 1959. Data are not available to evaluate this flux for earlier times. Without knowing the rise time we can only assume the peak measured flux is a fair average of the earlier flux. The dose rate within the Model 410 from this event would be

$$2.04 \times 1.53 \times .825 = 2.58 \text{ REM/hr}$$



~~CONFIDENTIAL~~

as scaled from the dose rate on May 12, 1959 (including the free space and spectrum correction factors). Using this rate as a constant for 1.2 days (28.8 hrs) gives a dose 74.2 REM, to which must be added the integrated flux after 1.2 days. This is  $2.2238 \times 10^9$  particles/sq cm-steradian or an additional 37.2 REM which gives a total of 111.4 REM within the Model 410 command module for this event.

Examination of Table I-1 shows one other series of events with high fluxes, which occurred during November, 1960. Van Allen has given the time integrated flux of protons with energies greater than 30 Mev as

23:37/14 Nov

$$\int J_0 dt = 1.0 \times 10^9/\text{sq cm}$$

20:42/12 Nov

00:00/16 Nov

$$\int J_0 dt = 4.2 \times 10^9/\text{sq cm}$$

13:30/12 Nov

From his data and that presented by Ney and Stein (1961), the exponent of the integral energy spectrum is 3, so the total flux above 20 Mev would have been

$$14.2 \times 10^9/\text{sq cm} \text{ or } 1.13 \times 10^9/\text{sq cm-steradian}$$

From calculations within the Model 410, a flux of  $5.11 \times 10^4$  protons/sq cm-sec-ster above 20 Mev gave 2.04 REM/hr or  $8.85 \times 10^7$  protons/sq cm-steradian = 1 REM. A free space correction factor of 1.36 should be applied to Dr. Van Allen's fluxes (average altitude of Explorer VII  $\sim 850$  km) and a correction factor of 2.85 to account for the flatter spectrum. The total dose from this event would have been

$$\frac{1.13 \times 10^9}{8.85 \times 10^7} \times 2.85 \times 1.36 = 49.5 \text{ REM}$$

~~CONFIDENTIAL~~

ER 12018

over the period from the very beginning of the class 3+ flare (13:23 UT on Nov 12, 1960) including a second class 3+ flare (02:07 UT on Nov 15, 1960) and up to 00:00 on the 16th of November.

An examination of Table I-1 shows that a number of other events do not show significant proton fluxes and the resulting dosages are not significant. The next most intense events seen from Table I-1 and data obtained after its preparation occurred April 1, 1960 and September 3, 1960. Peak fluxes for these events are given as about 4-5/sq cm-sec-steradian ( $E > 30$  Mev) by Van Allen. Fichtel and Guss (1961) reported a flux of 15/sq cm-sec-steradian ( $E > 20$  Mev) measured approximately 13 hours after the class 3 flare on September 3, 1960. The remaining data on proton events show fluxes of approximately 0.1 to 2.0/sq cm-sec-ster.

Although particle emissions from the sun are not infrequent occurrences, apparently only a few events would have resulted in significant doses to the crew within the command module. These were:

50 REM following series of solar flares on November 12, 1960

67 REM following solar flare on May 10, 1959

111 REM following solar flare on July 16, 1959

360 REM following solar flare on July 14, 1959

Most of these are compound events. Enough warning time may be available to abort the mission and return to the earth before a large dose is received. Even with no warning, the time span of these events is long enough that if abort is initiated just after the flare sighting or after initial measurement of the arrival of the particles, the crew can return to earth before the full dosage from the compound events is received.

~~CONFIDENTIAL~~

As previously mentioned, these events can not be defined for occurrence probability, but from the data available it appears that an event giving a dose of 50-67 REM occurs approximately once a year near the period of maximum sunspot activity, while an event of 360 REM usually occurs once every two years. For a 14-day mission, the probability of 67 REM is about 0.037 and is about 0.018 for 360 REM.

During the past 20 years, there have been a number of solar events comprised of particles with energies of one Bev to tens of Bev. These occur approximately once every three or four years. The most famous occurred February 23, 1956. The data on these events has been generally limited to neutron monitors on the ground, but Explorer VII made some measurements on May 6 and 7, 1960 which showed a flux of about 1.0/sq cm-sec-steradian ( $E > 30$  Mev). From the monitor data, it generally had been concluded that, in free space, these events would be more of a hazard than events containing particles in the tens to hundreds of Mev region. This does not appear to be absolutely true, although the reason for the characteristically greater particle energy is unknown in these events.

Foelsche (1961) has estimated the dose from the February 23, 1956 event and showed values (under 10 g/sq cm) which were smaller than from the July 14, 1959 "low energy" event. His numbers were approximately 350 REP for July 14, 1959 and 120 REP (35-200) for February 23, 1956.

Without ignoring the uncertainties in ranking these events on a probability basis, it is reasonable to expect that the overall probability can be reduced by scheduling flights during periods of reduced flare activity. By using seasonal occurrence trends, the probability of an event during a specific mission can be halved, and by using grouped occurrences, the probability can be reduced further. Adamson (1961) has indicated the overall reduction to be a factor of 2.4. There is a corresponding increase in encountering more than one event, and Adamson has estimated this to be two times. The mission will be terminated before a second event can reach full development, so this factor can be discounted. It has been shown by Goedeke (1961) that solar activity seasons are systematically displaced from year to year. If this particular trend is evidenced in future measurements, seasonal launch scheduling actually may offer a reduction of four to five times in the probability of encountering a significant solar flare particle event. It also is emphasized that these events decrease in frequency during the solar sunspot cycle minimum. Although recent events have indicated that this decrease is not as great as previously believed, it appears reasonable to decrease any probabilities obtained from data of the recently completed solar maximum five times when considering a period of minimum solar activity (1963 to 1964).

The dose rate from protons at the heart of the inner Van Allen Belt is 5.21 REM/hr within the Model 410 command module (without any spot shielding). The emergent energy spectrum obtained is shown in Fig. VI-9. The shape of

~~CONFIDENTIAL~~

this spectrum is quite different than the spectra from solar protons. This is due to the different incident spectrum. The dose distribution within the Model 410 is shown in Fig. VI-10.

The RBE calculated from the Van Allen protons is shown in Table VI-5, and is slightly lower than the value obtained for the flare particles. The flatter incident spectrum has a smaller proportion of emergent particles near termination energy so it has a lower RBE. A scatter is evident in the emergent energy spectrum at low energies (which has been smoothed only in the curve plotting but not in the RBE determinations). This is at least partially due to the fact that this spectrum is the sum of the individual spectra of each area. The individual areas, which are comprised of different materials and thicknesses, have different emergent spectra. By plotting the individual spectra, a determination is possible to see whether scatter is completely physical or if any of it is due to degradation in the accuracy with which the machine program computes very low emergent energies.

These individual emergent spectra also can be used as man incident spectra to determine in great detail the internal dose distribution within the man. Accounting can be made for the effects of mutual shielding among the crew and self-shielding by the body of each man. These factors, which reduce the dose, previously have been neglected.

The total proton dose has been calculated that would be received on four different lunar trajectories leaving the earth, and on one re-entry trajectory. These are shown on Fig. VI-11 through VI-15. The largest dose (0.63 RAD) is encountered on an equatorial flight injected at 0 degrees longitude. A dose of 0.56 RAD is received on the flight injected from 21.7 degrees S, 102.6 degrees E, at an inclination of 35 degrees. The two other flights (injection north of the equator) received 0.06 RAD each. The re-entry trajectory resulted in a dose of 0.31 RAD.

The absolute maximum and minimum inner Van Allen Belt proton doses can be determined by a large number of trajectories. However, Fig. VI-11 (0.626 RAD) is probably very close to the maximum dose and Fig. VI-14 (0.06 RAD) is probably the minimum dose transit at a 35-degree inclination.

An earlier report (ER 11245M) discussed trajectory shaping and relaxation of range launch azimuth requirements as means to avoid the inner Van Allen Belt. These procedures evolved from early estimates of the dose received through this region. Earlier estimates contained an ignorance factor of 10 because of the overestimate of RBE, but the emergent spectrum within the Model 410 yields an effective RBE of only 1.01. The value of 10 for RBE had been developed from analogies to the recoil proton spectrum near reactors. This analogy does not apply to either the Van Allen or solar flare spectra within the command module.

~~CONFIDENTIAL~~TABLE VI-5

## Proton RBE Within Model 410 Command Module

Van Allen Belt Particles			
Energy (Mev)	% of Total No. Particles	RBE	(RBE) x (%)
> 14	98.018	1	98.018
14-13	0.190	1	0.190
13-12	0.232	1.02	0.237
12-11	0.233	1.05	0.245
11-10	0.233	1.1	0.256
10-9	0.086	1.16	0.100
9-8	0.191	1.27	0.243
8-7	0.237	1.44	0.341
7-6	0.175	1.65	0.289
6-5	0.118	1.90	0.224
5-4	0.053	2.22	0.118
4-3	0.091	2.67	0.243
3-2	0.058	3.30	0.191
2-1	0.051	4.47	0.228
1-0	0.033	8.5	<u>0.280</u>
Total	100.00		101.203
	Mean RBE		1.01

Total Incident Particle Flux	$3.091 \times 10^4$ /sq cm-sec	} at center of belt
Total Emergent Particle Flux	$5.254 \times 10^3$ /sq cm-sec	
Emergent Flux / Incident Flux		17.00%

~~CONFIDENTIAL~~

Also, early estimates did not account properly for the decrease in ambient proton flux experienced within the spacecraft, and this also influenced the over-estimation of the dose severity from the Van Allen belt protons. The early estimates basically showed a peak ambient dose of 10 RAD/hr (or 100 REM/hr, using an RBE of 10); the new model gives a peak of 5.16 RAD/hr (or 5.21 REM/hr with an RBE of 1.01) within the Model 410 command module. The early estimate of the greater ambient dose in traveling through this region was 1.9 RAD (or 19 REM), but calculations now show only 0.626 RAD (0.63 REM) as the dose for the worst case. The net effect of this is a significant degradation of the inner belt proton hazard.

ER 11245M indicated that trajectories which avoid the inner region also would reduce the exposure in the outer region. This was based upon examination of the simplified models of the radiation belts, but detailed models of the belt support this general conclusion. However, this does not necessarily mean that any trajectory that results in a low inner belt proton dose also will give minimum exposure in the outer belt.

For example, Fig. VI-13 shows 0.064 RAD from protons of the inner belt, which represents the second lowest proton dose in traveling through the inner region. The inner belt bremsstrahlung contribution would have been proportionately lower than one received along the trajectory of Fig. VI-12 which gave the second highest proton dose. When these trajectories are followed through the outer region, both trajectories cross through the heart of the outer region. On the other hand, if the trajectory of Fig. VI-14 (which gave the lowest inner belt proton dose) is followed, it avoids the heart of the outer region. These effects are shown in Fig. VI-16.

The reason for these variations is simple. The belt inclination changes greatly with earth longitude as shown by Table VI-6. The trajectory which initially avoids much of the inner belt may change longitude in a manner such as to take it through the heart of the outer belt. It is not possible to eliminate the desirability of trajectory shaping without considering the resultant dosage from exposure to the electrons of both belts and the secondaries from the inner belt protons. Only approximations of the resulting dosages can be reported, for electron and bremsstrahlung calculations are not available.

The electron distribution model developed is applicable to normal conditions during solar maximum. (During solar minimum the belt would shrink in extent and intensity, but during disturbed sun conditions the intensity probably would increase.) Considering a path through the hearts of both belts enables an estimation of the maximum dose of the electron bremsstrahlung between 0.4 and 2.0 RAD (RBE of X-rays = 1) in the Model 410. There are a number of inherent uncertainties in such an estimate. The emergent bremsstrahlung spectrum actually is comprised of many spectra, limited by only the detail with which the incident spectrum is analyzed. Production and absorption of X-rays (most of which will be  $< 50$  Kev) is quite different for materials such as steel, carbon, aluminum and lead. The emergent spectra is heterogeneous in the

~~CONFIDENTIAL~~

TABLE VI-6  
Van Allen Belt--Reference Point Position

Reference Altitude* (km)	Latitude** (deg)	Longitude (deg)	Reference Altitude (km)	Latitude (deg)	Longitude (deg)
980	9.0	5	1445	9.2	105
1005	9.0	10	1445	8.9	110
1015	10.0	15	1435	8.7	115
1035	9.5	20	1420	8.4	120
1060	9.5	25	1400	8.2	125
1075	9.2	30	1380	8.0	130
1100	8.8	35	1350	7.8	135
1120	8.6	40	1325	7.4	140
1140	8.5	45	1300	7.2	145
1170	8.4	50	1270	7.0	150
1200	8.1	55	1240	6.6	155
1230	8.0	60	1225	6.2	160
1270	8.1	65	1205	5.5	165
1300	8.4	70	1190	4.8	170
1338	8.6	75	1170	4.0	175
1368	8.8	80	1160	3.5	180
1400	9.0	85	1150	2.5	-175
1420	9.2	90	1140	1.9	-170
1435	9.3	95	1130	1.1	-165
1445	9.3	100	1120	0.3	-160

~~CONFIDENTIAL~~

TABLE VI-6 (cont)

Reference Altitude* (km)	Latitude** (deg)	Longitude (deg)	Reference Altitude (km)	Latitude (deg)	Longitude (deg)
1110	-0.2	-155	595	-12.1	-50
1100	-0.8	-150	600	-10.4	-45
1085	-1.4	-145	625	-8.3	-40
1075	-2.0	-140	675	-5.8	-35
1065	-2.7	-135	705	-3.0	-30
1052	-3.2	-130	745	-0.1	-25
1040	-3.9	-125	795	+2.5	-20
1025	-4.6	-120	825	+4.7	-15
1015	-5.0	-115	860	+6.4	-10
1000	-6.0	-110	895	+7.8	-5
975	-7.0	-105	935	+8.6	0
950	-8.0	-100			
925	-9.0	-95			
895	-10.0	-90			
850	-11.1	-85			
805	-12.3	-80			
750	-13.1	-75			
705	-13.7	-70			
660	-14.0	-65			
625	-13.9	-60			
600	-13.4	-55			

\* of first particle contour line at axis of belt

\*\* of axis of belt



~~CONFIDENTIAL~~

TABLE VI-7

## Weight Fractions of Isotopes Present in the Command Module Materials

## (Forward Section)

Region Number and Material	Weight Fractions	
	<u>Carbon -12</u>	<u>Aluminum -27</u>
1. Ablator	0.6889	-
2. Super Alloy	-	-
3. Insulation	0.1333	0.3449
4. Water	-	-
5. Aluminum	-	1.000
6. Equipment	-	0.600

## (Aft Section)

Region Number and Material	Weight Fractions	
	<u>Carbon -12</u>	<u>Aluminum -27</u>
1. Structure and Engines	-	1.000
2. Oxygen	-	-
3. Hydrogen	-	-
4. Polyurethane Foam	0.5167	-
5. Glass Phenolic	0.2663	-
6. Equipment	-	0.600
7. Aluminum	-	1.000

Model 410. Furthermore, energy loss in the body is definitely a function of the energy (spectra), so any estimate is quite uncertain. This uncertainty believed to be is bracketed by the estimate of 0.4 to 2.0 RAD. This will be substantiated by the results of the detailed electron program.

~~CONFIDENTIAL~~

The Model 410 command module is used during the computation of secondary radiation dose from proton interaction during exposure to solar flare proton radiation and Van Allen inner belt proton radiation. Only secondary neutrons were considered in the analysis. This included both neutrons from the evaporation and cascade processes. The proton reactions considered are of type  $Al^{27}(p, xn)$  and  $C^{12}(p, xn)$ . The actual abundances of the target isotopes present in the material regions of the configuration are listed in Table VI-7.

Energy loss by ionization and excitation is determined for each material region by adding the contributions from various elements which comprise the region. Range energy relationships determined from the energy loss equations were used in evaluating the internal proton energy spectrum. The reaction cross sections, average secondary particle energies and number of secondary particles for both the evaporation and cascade processes were determined from data which were computed on the basis of the compound nucleus theory and by Monte Carlo techniques. For neutron attenuation the total neutron microscopic cross sections given by Hughes and Schwartz (1958) and Hughes, Magurno and Brussel (1960) were used.

Table VI-8 shows the contribution to radiation dose from secondary neutrons caused by exposure to solar flare spectrons and Van Allen inner belt protons. The measurements are made in the command module.

TABLE VI-8. Secondary Neutron Dose Rates and Doses

<u>Solar Flare</u>	<u>RAD/hr</u>	<u>(REM/hr)</u>	<u>(RAD)</u>	<u>(REM)</u>
May 10th	$4.52 \times 10^{-3}$	$4.34 \times 10^{-2}$	$1.45 \times 10^{-1}$	$1.39 \times 10^0$
<u>Van Allen</u> <u>Inner Belt</u>				
Peak dose rate	$7.55 \times 10^{-1}$	$5.57 \times 10^0$		

(The total radiation dose due to secondary neutrons received during flight through the inner Van Allen belt are given for two trajectories.)

Initial Conditions for Trajectory

<u>Trajectory</u>	<u>Altitude (km)</u>	<u>Latitude (deg)</u>	<u>Longitude (deg)</u>	<u>Radiation Dose (REM)</u>
Fig. VI-12	234.8	21.7S	102.6E	0.605
Fig. VI-11	234.8	0	0	0.687

~~CONFIDENTIAL~~

The secondary neutrons are expected to contribute a major portion of the secondary radiation dose. For example, the secondary protons will have energies considerably lower than the primary protons and therefore, relatively few are expected to contribute to the secondary radiation dose. It is expected that contributions of elements not considered because of a lack of basic data will not increase the given doses by more than a factor of 1.5 to 2. The reported secondary doses are expected to fall within a factor of 2 of a total secondary radiation dose.

Table VI-8 shows a peak dose rate at the heart of the Van Allen proton belt of 0.755 RAD/hr within the Model 410. The RBE used for evaporation neutrons was 10 and for cascade neutrons was 5. The resultant biological dose rate is 5.57 REM/hr. A total neutron dose of 0.687 REM is obtained along the trajectory which gave the highest proton dose (0.626 RAD, Fig. VI-11).

The relative dose neutrons produced by solar flare protons is considerably lower because of the steeper spectrum of the flare particles. For the May 10, 1959 event, a total of 0.263 RAD would have been received using the RBE's as before the biological dose from these neutrons is 2.53 REM and the combined biological dose for this event becomes  $67 \pm 2.5 \sim 70$  REM.

A galactic cosmic ray dose of 1.4 to 2.8 REM on a 14-day mission (ER 11245M) during solar cycle maximum and minimum, respectively, had been estimated earlier. No additional data has been found to change this estimate. A comprehensive evaluation of the dose from these particles requires interaction and biological effectiveness data which are not available.

### Conclusions

The analyses undertaken and described in this report show the significant radiation shielding afforded by the normal components of the Model 410 spacecraft. While the dosages to an unprotected man in the space environment may be greatly in excess of tolerable amounts, it appears that adequate radiation exposure protection is available within the Model 410 command module without compromising the spacecraft and its mission.

A normal mission should not expose the Apollo crew to more than about 2.2 to 9.4 REM (Table VI-9).

Most of the flights likely will result in an exposure of less than 5 REM since the full 14-day missions probably will coincide in time with the decreasing values of cosmic ray dose.

An emergency condition is represented by the occurrence of a large heavy particle flux from the sun, but an event of intensity sufficient to give a dose of about 70 REM has a probability no greater than about 0.037 by the end of a 14-day mission during sunspot cycle maximum.

~~CONFIDENTIAL~~

TABLE VI - 9

Normal Mission Dose Schedules Within  
The Model 410 Command Module

Sunspot Phase	Maximum (1968-1969)	Minimum (1963-1964)
Best trajectory (outgoing and incoming)		
Van Allen protons	0.12	0.12
neutrons*	0.28	0.28
electron bremsstrahlung	0.40	0.04
Cosmic rays (14-day total)	<u>1.40</u>	<u>2.80</u>
	2.20 REM	3.24 REM
Worst trajectory		
Van Allen protons	1.26	1.26
neutrons*	2.74	2.74
electron bremsstrahlung	4.00	0.40
Cosmic rays (14-day total)	<u>1.40</u>	<u>2.80</u>
	9.40 REM	7.20 REM
*Including a factor of two for reactions not considered		

**CONFIDENTIAL**

**CONFIDENTIAL**

VII. BIBLIOGRAPHY

1. Freden, S. C., and White, R. S., "Particle Fluxes in the Inner Radiation Belt," J. Geophys. Research, 1377-1383, 1960.
2. Holley, F. E., "Radiation Measurements to 1500 Kilometers with Atlas Pods," Air Force Special Weapons Center, TR 60-9, 1960.
3. Van Allen, J. A., and Frank, L. A., "Radiation Around the Earth to a Radial Distance of 107, 400 km," Nature, 183, 430-434, 1959a.
4. Van Allen, J. A., and Frank, L. A., "Radiation Measurements to 658,300 km with Pioneer IV," Nature, 184, 219-224, 1959b.
5. Van Allen, J. A., McIlwain, C. E., and Ludwig, G. H., "Radiation Observations with Satellite 1958E," J. Geophys. Research, 64, 271-286, 1959.
6. Van Allen, J. A., "The Geomagnetically Trapped Corpuscular Radiation," J. Geophys. Research, 64, 1683-1689, 1959.
7. Walt, M., Chase, L. F. Jr., Cladis, J. B., Imhof, W. L., and Knecht, D. J., "Energy Spectra and Altitude Dependence of Electrons Trapped in the Earth's Magnetic Field," Presented at the First International Space Science Symposium, Nice, France, 1960.
8. Winckler, J. R., and Bhavsar, P. D., "Low Energy Solar Cosmic Rays and the Geomagnetic Storm of May 12, 1959," J. Geophys. Research, 65, 2637-2655, 1960.
9. Yoshida, S., Ludwig, G. H., and Van Allen, J. A., "Distribution of Trapped Radiation in the Geomagnetic Field," J. Geophys. Research, 65, 807-813, 1960.
10. Aron, Hoffman and Williams, "Range-Energy Curves," Second Revision 1949, United States Atomic Energy Commission Report No. AECU-663.
11. Welch, J. A., "Theory of Geomagnetically Trapped Particles," Air Force Special Weapons Center, TN 60-29, 1960.
12. Anderson, K. A., "Preliminary Study of Prediction Aspects of Solar Cosmic Ray Events," National Aeronautics and Space Administration, TN-D-700, 1961.
13. Adamson, D., "Private communication" March 14, 1961.

~~CONFIDENTIAL~~

14. Dessler, A. J., "Letters to the Editor," J. Geophys. Research, 3487-3490, 1960.
15. "Manned Lunar Vehicle System, Feasibility Survey," -v- .1, 2.1-2.80, The Martin Company ER11245M, 1960.
16. Ney, E. P., and Stein, W., "Solar Cosmic Rays in November 1960," Presented at the American Geophysical Union, 42nd Annual Meeting, Washington, D. C., 1960.
17. Foelsche, T., "Protection Against Solar Flare Protons," Presented at the 7th annual meeting of the American Astronautical Society, Dallas, Texas, 1961.
18. Goedeke, A. D., "The Frequency of Occurrence of Solar Flare Radiation Events," Proc. Inst. Environmental Sciences, 325-334, 1961.
19. Hughes, D. J. and Schwartz, R. B., "Neutron Cross Sections," Brookhaven National Laboratory, BNL325, 1958.
20. Hughes, D. J., Magurno, B. A., and Brussel, M. K., "Neutron Cross Sections," Brookhaven National Laboratory, BNL325, Sept. 1, 1960.
21. Rich, M., and Madey, R., "Range-Energy Tables," University of California Radiation Laboratory, UCRL2301, 1954.

~~CONFIDENTIAL~~

CONFIDENTIAL

R-VIII-1

## VIII. ILLUSTRATIONS

CONFIDENTIAL

ER 12018



~~CONFIDENTIAL~~

~~CONFIDENTIAL~~

ER 12018

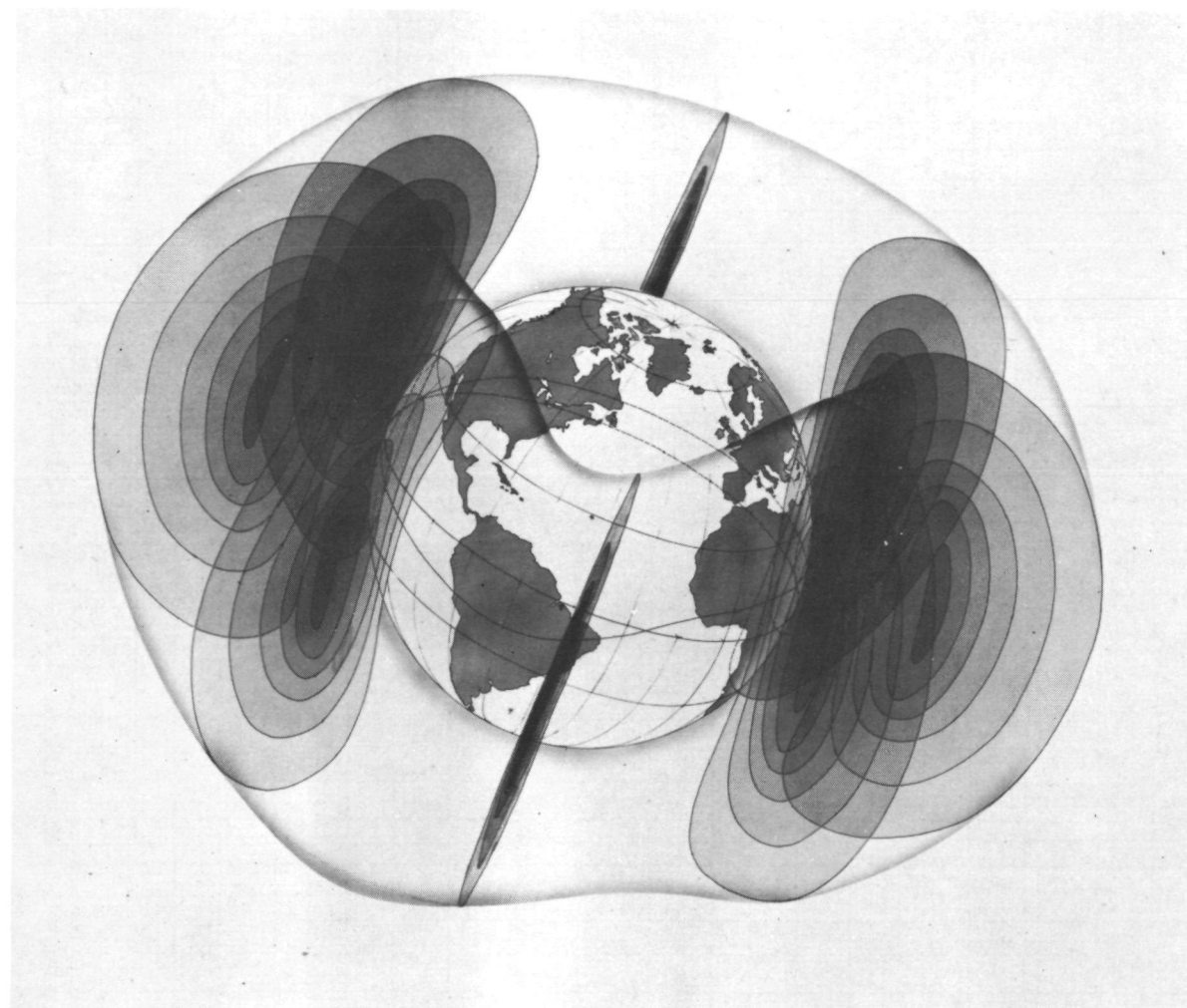


Fig. I-1. Inner Van Allen Belt

CONFIDENTIAL

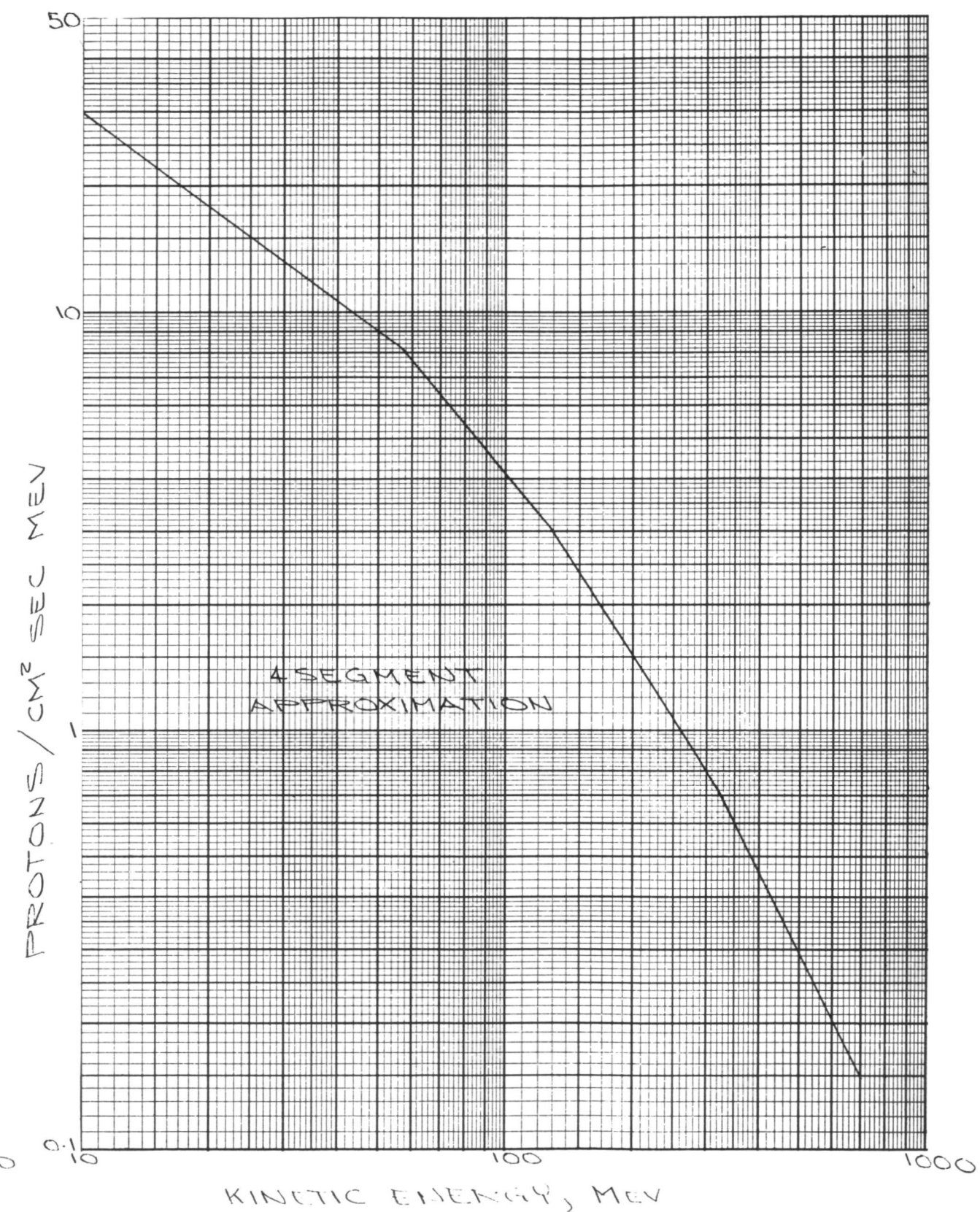
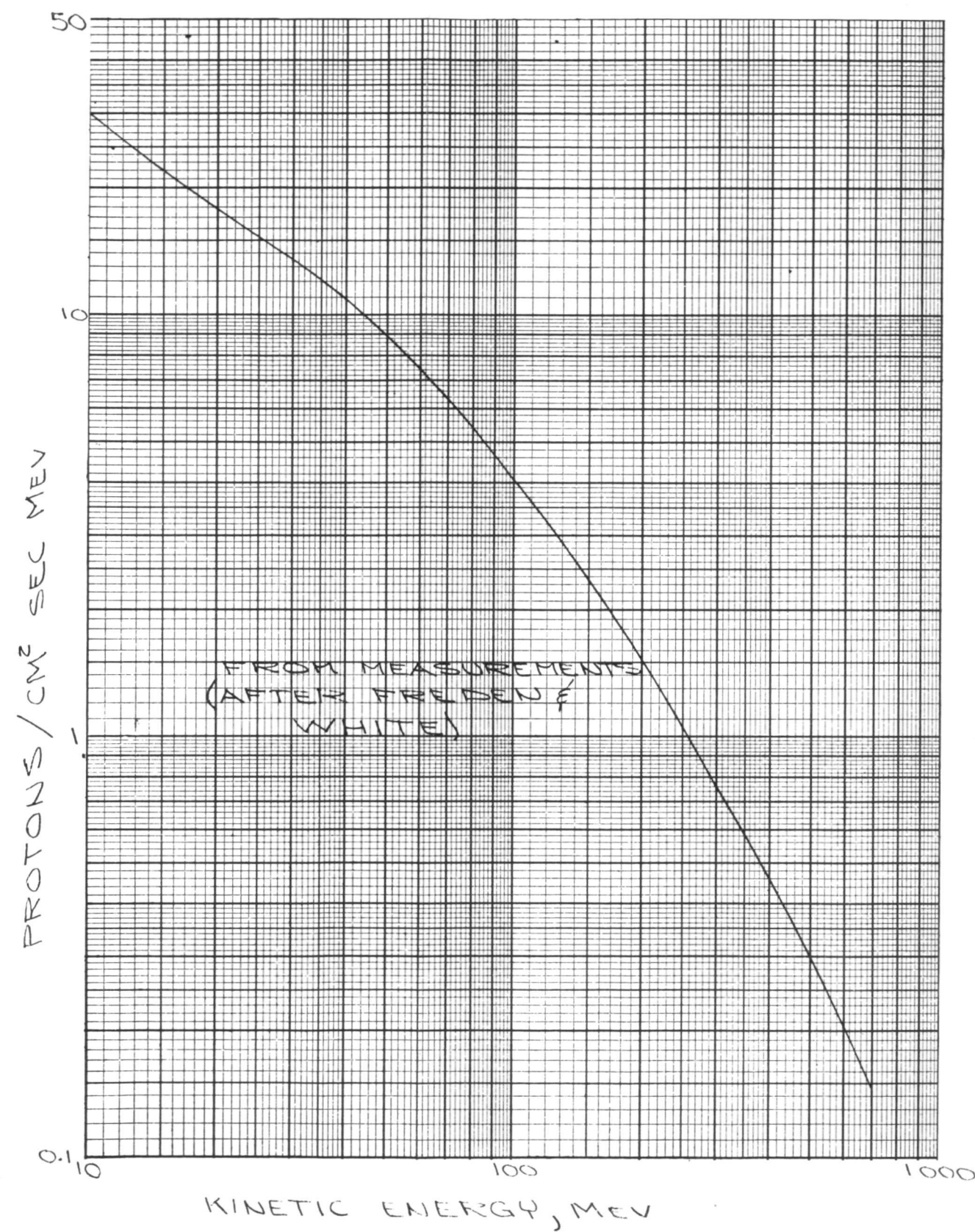


Fig. I-2. Proton Differential Kinetic Energy Spectrum for the Inner Van Allen Belt

CONFIDENTIAL

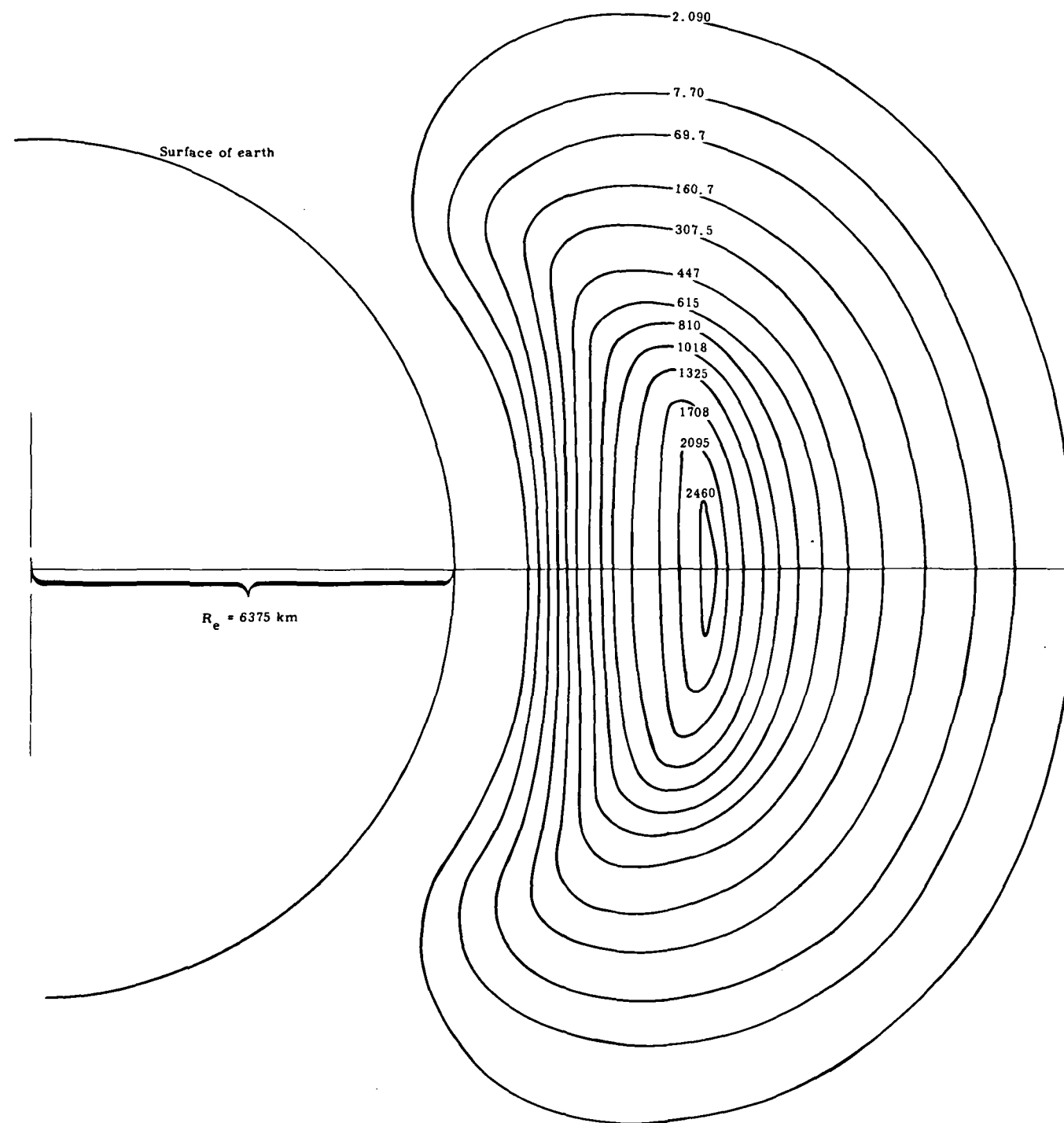


Fig. I-3. Flux of Protons in the Van Allen Belt



~~CONFIDENTIAL~~

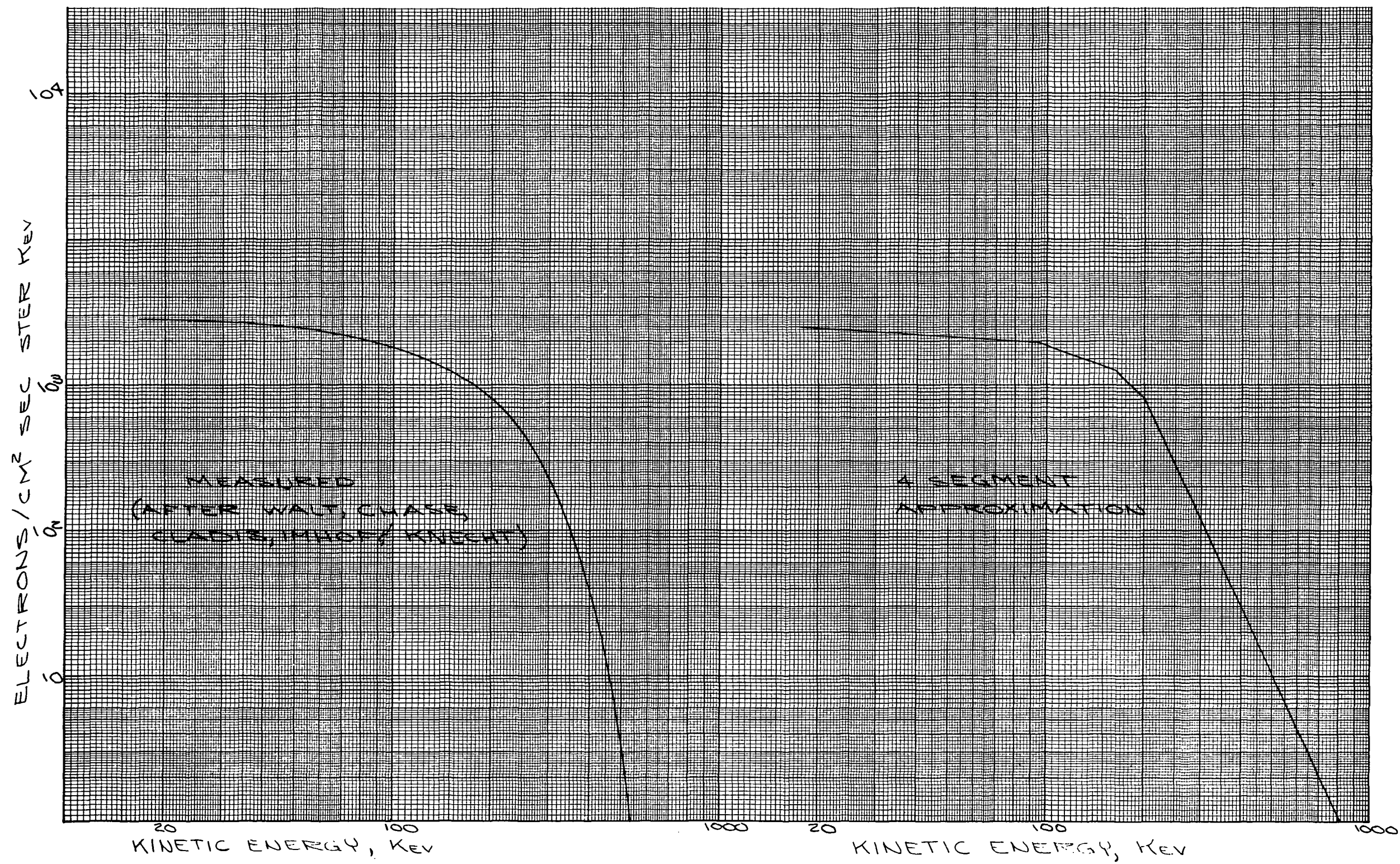


Fig. I-4. Differential Kinetic Energy Spectrum Van Allen Belt Electrons

~~CONFIDENTIAL~~

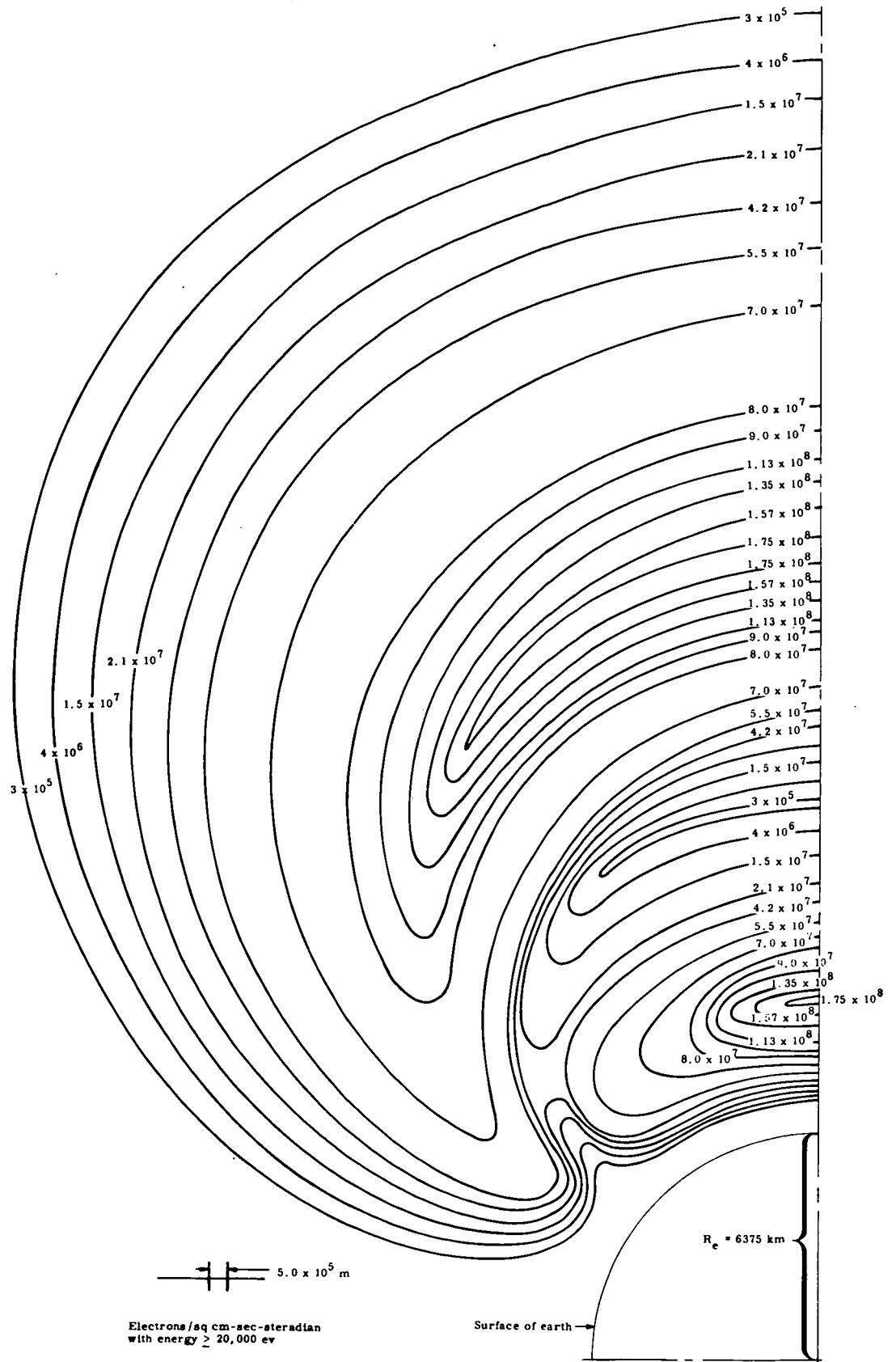
~~CONFIDENTIAL~~

Fig. 3. Flux of Electrons in the Van Allen Belts

Fig. I-5. Flux of Electrons in the Van Allen Belts

~~CONFIDENTIAL~~

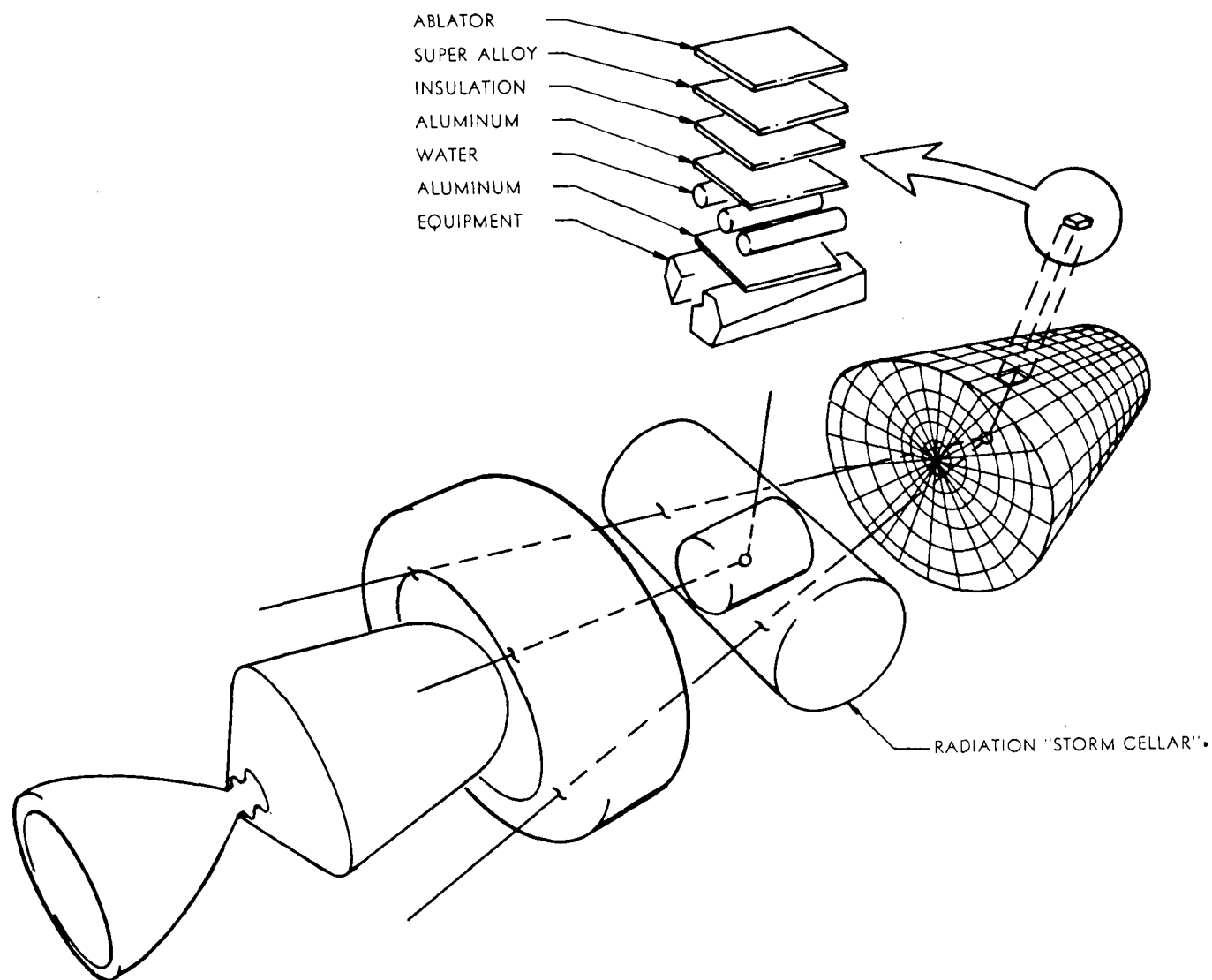


Fig. III-1. Geometrical Relationship Used in Calculation of Radiation Doses





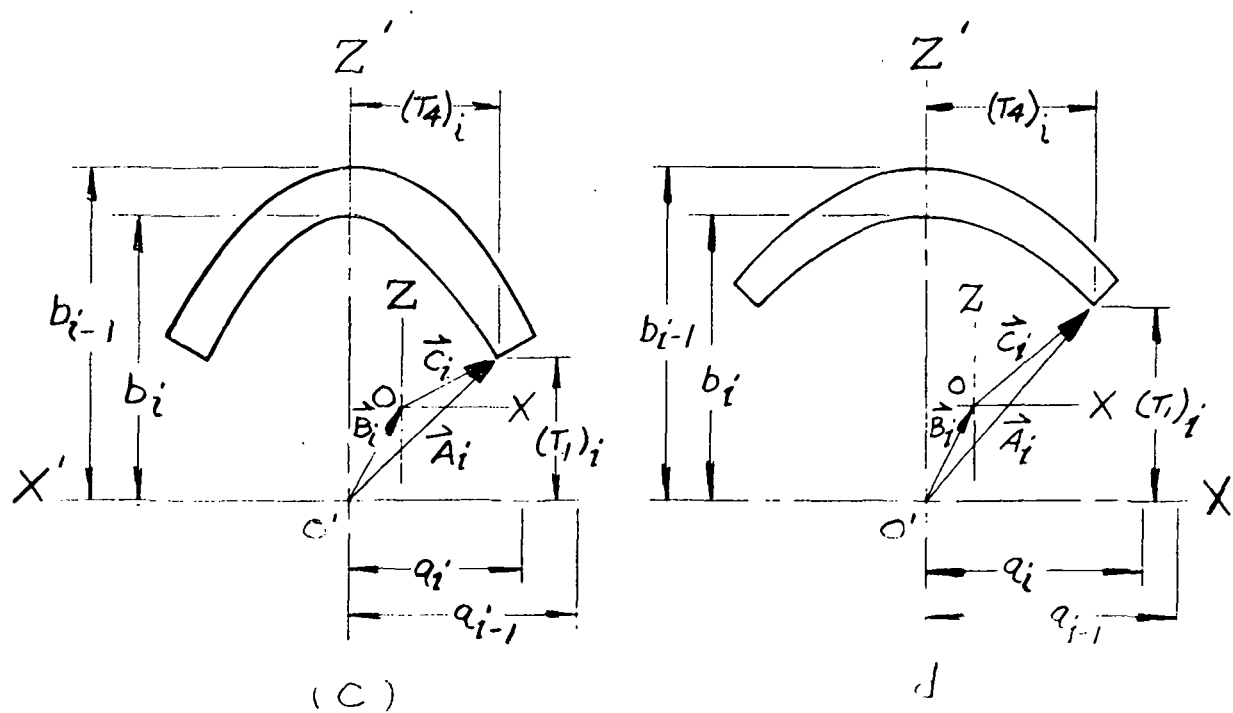
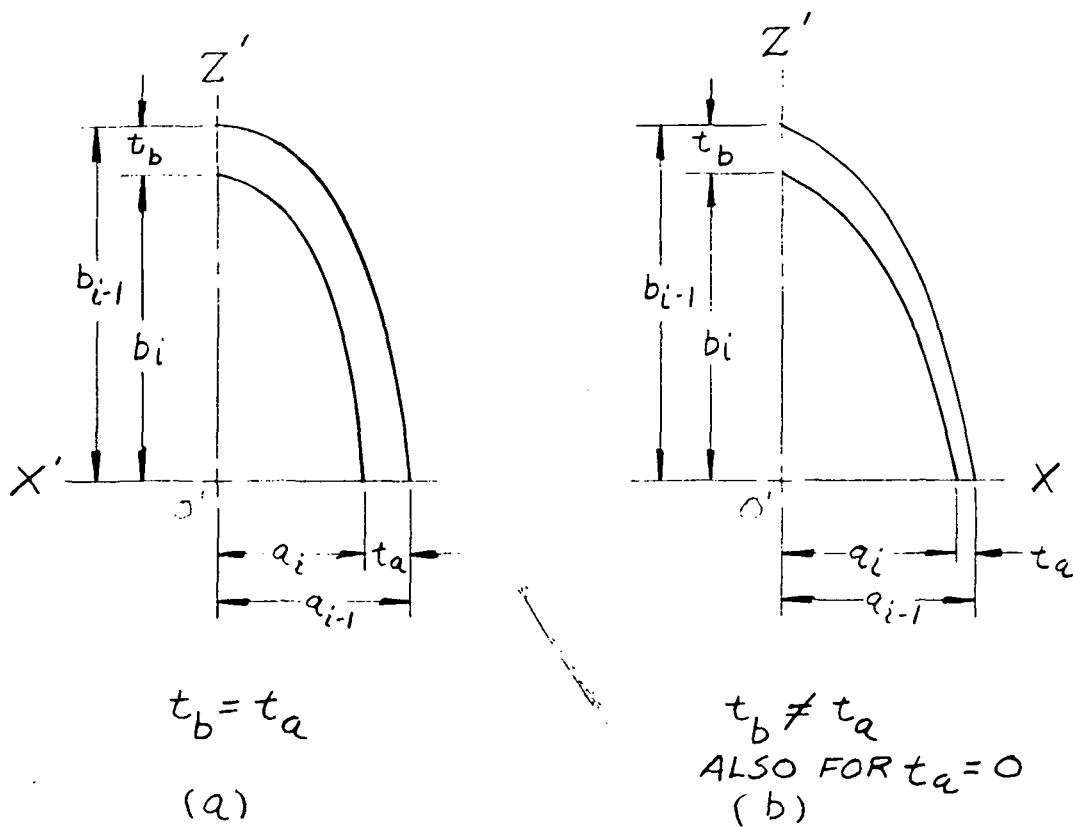
~~CONFIDENTIAL~~

Fig. V-2. Radiation Dose Evaluation--Special Cases

~~CONFIDENTIAL~~

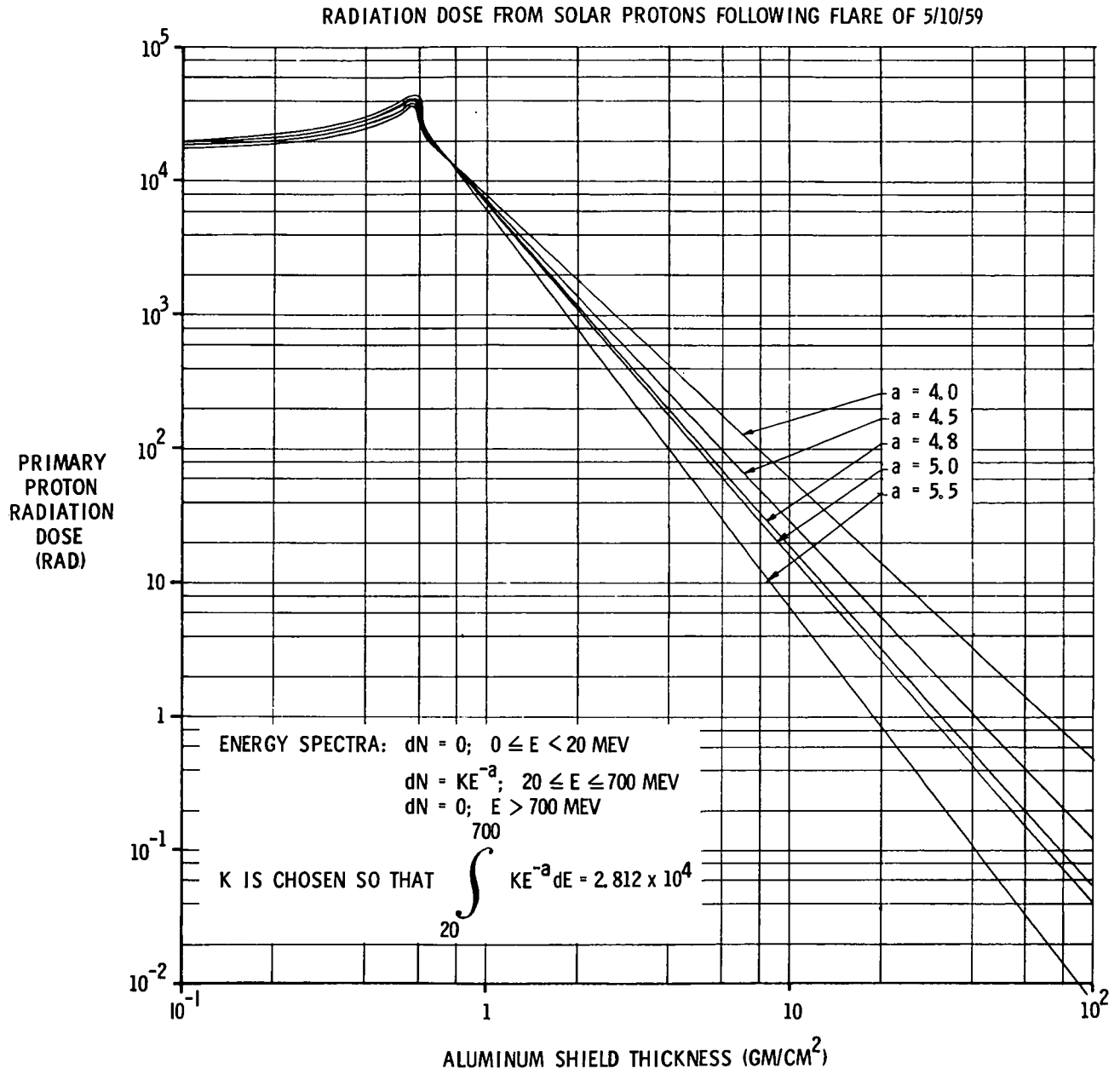


Fig. VI-1. Radiation Dose From Solar Protons Following Flare of May 10, 1959  
(Total Flux Equal)

~~CONFIDENTIAL~~

## RADIATION DOSE FROM SOLAR PROTONS FOLLOWING FLARE OF 5/10/59

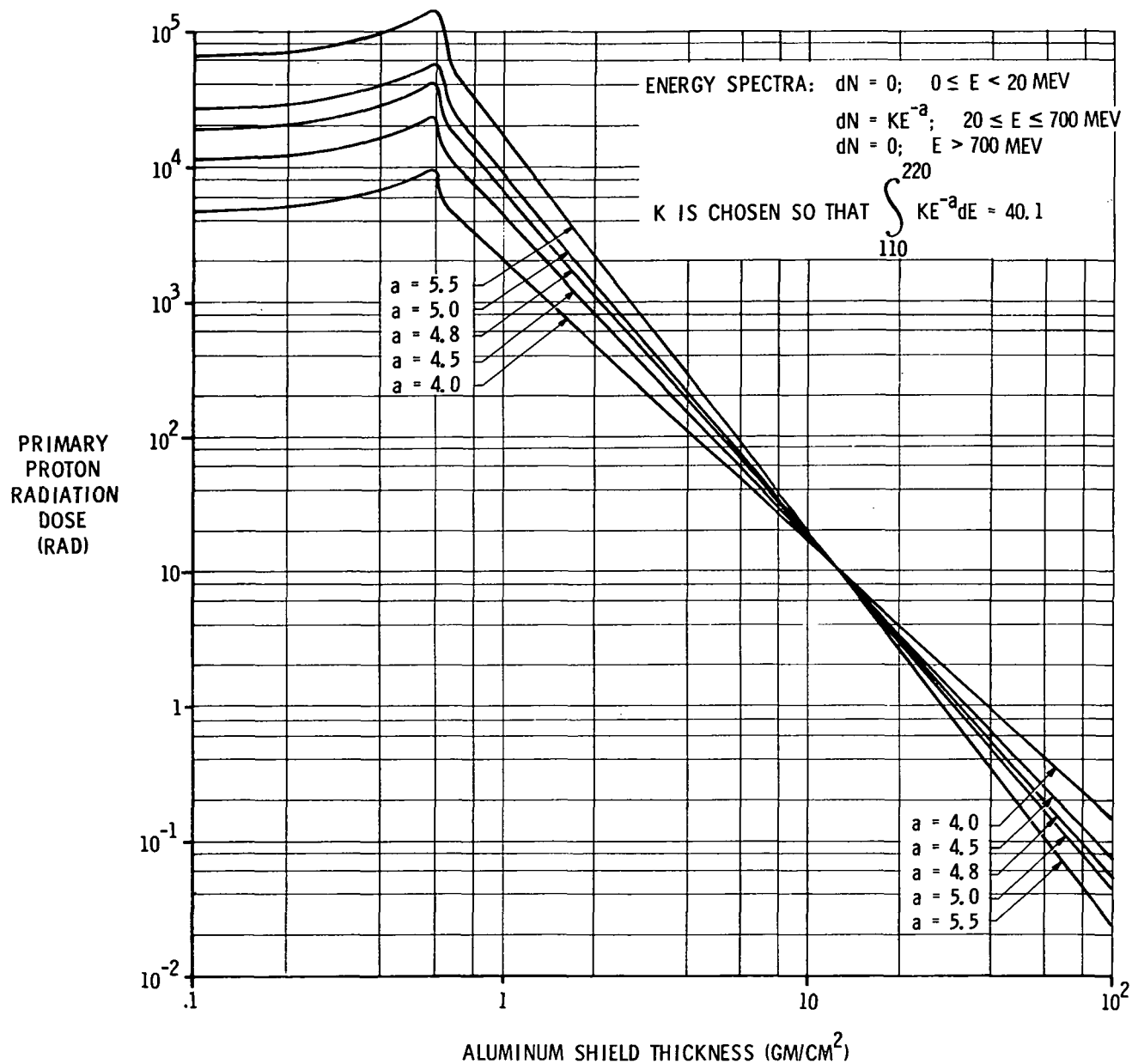


Fig. VI-2. Radiation Dose From Solar Protons Following Flare of May 10, 1959  
 (Flux at Measured Intervals Equal)

~~CONFIDENTIAL~~

ER 12018

~~CONFIDENTIAL~~

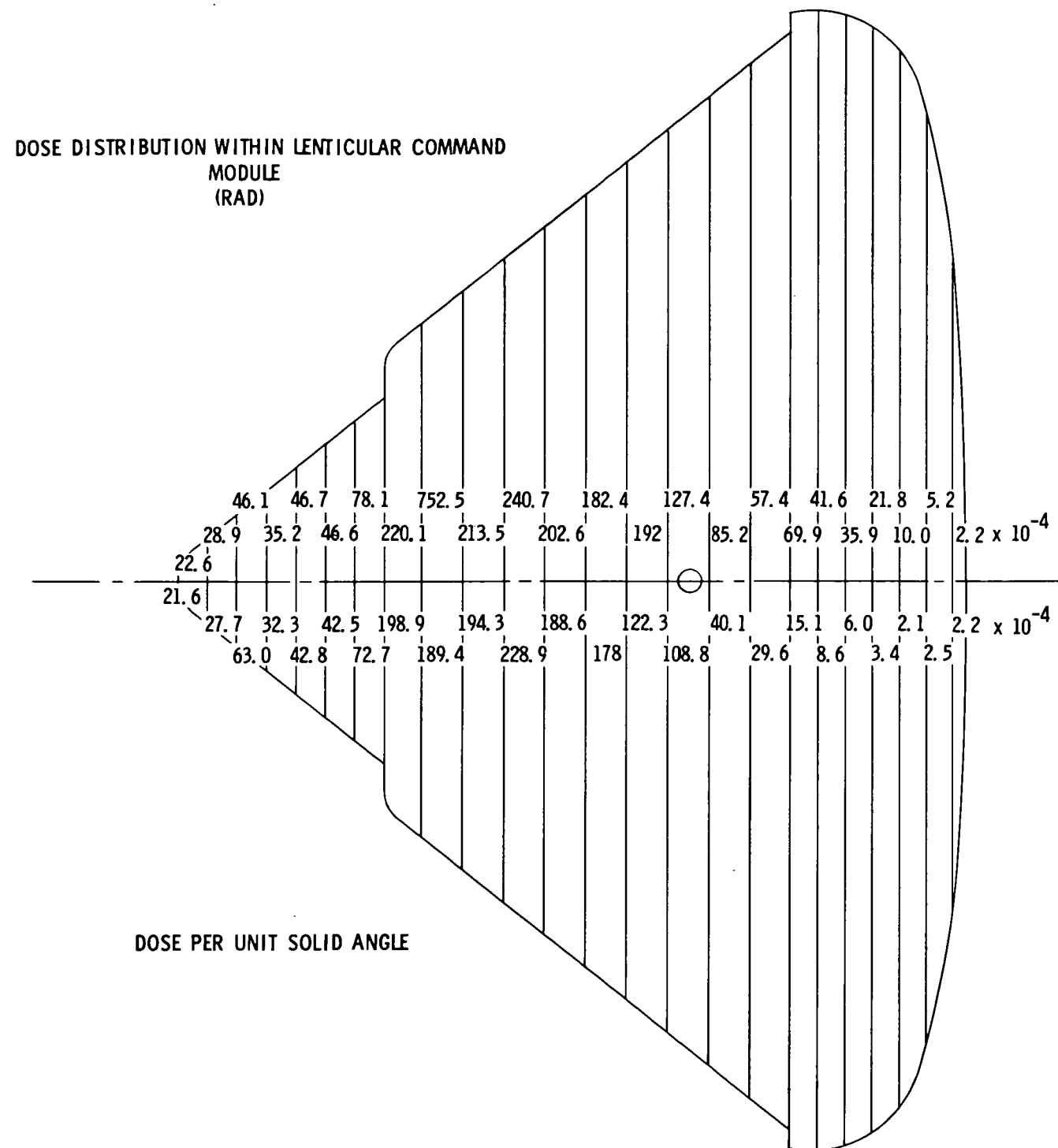
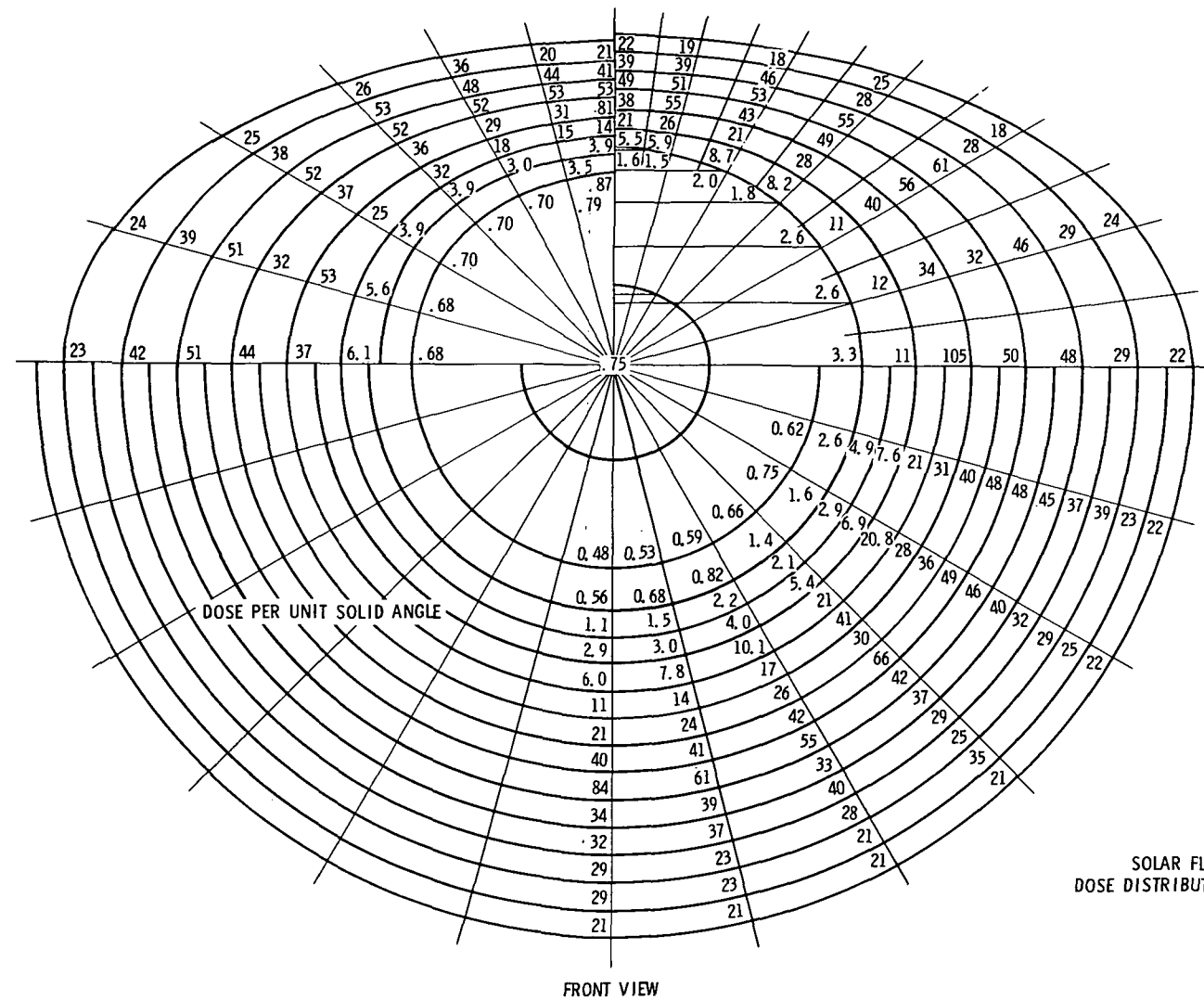


Fig. VI-3. Dose Distribution Within Command Module

~~CONFIDENTIAL~~

~~CONFIDENTIAL~~

SOLAR FLARE (MAY 10, 1959) RADIATION  
DOSE DISTRIBUTION WITHIN LIFTING BODY COMMAND  
MODULE (RAD)

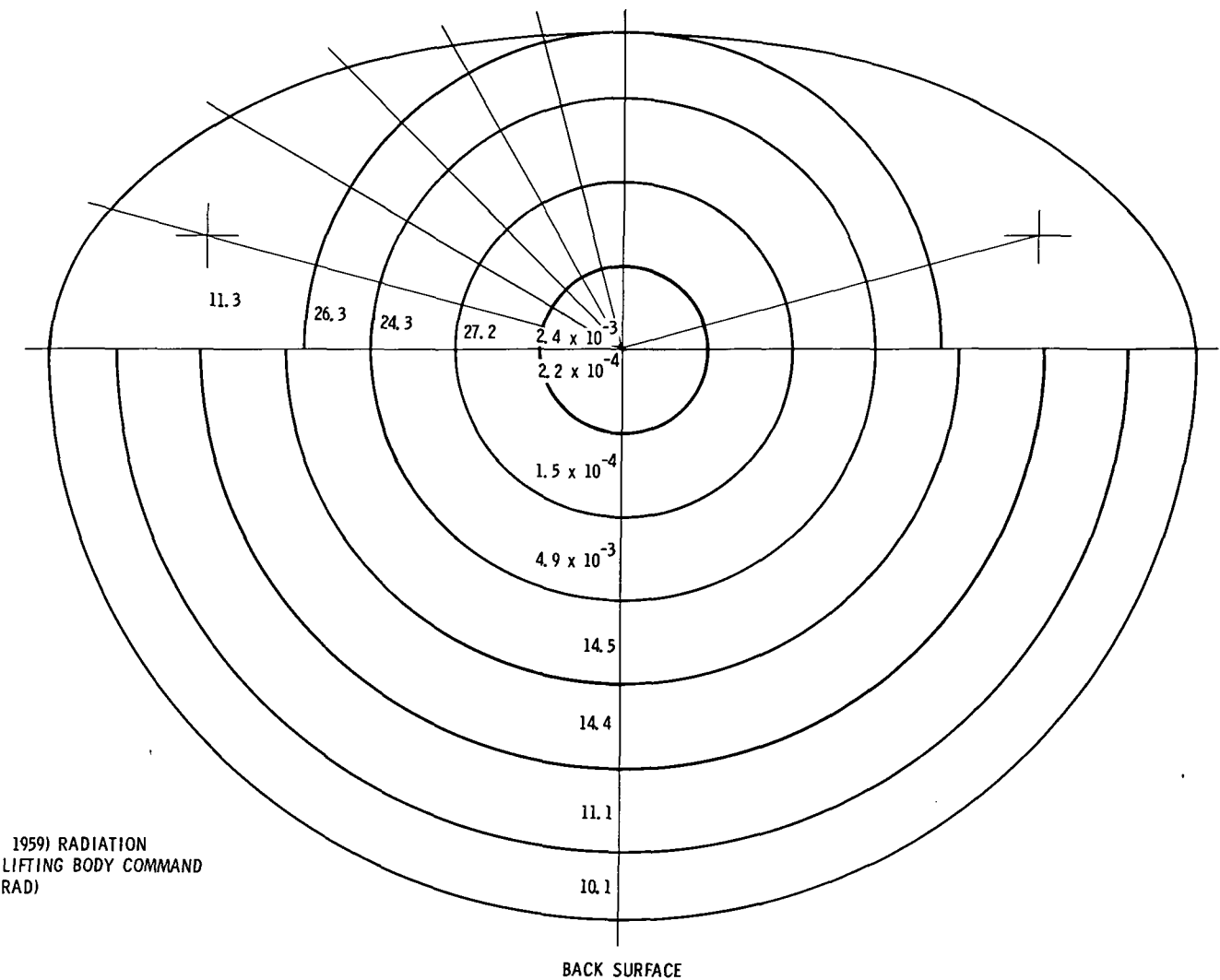


Fig. VI-4. Solar Flare Radiation

~~CONFIDENTIAL~~

~~CONFIDENTIAL~~

## SOLAR FLARE RADIATION DOSE INSIDE "STORM CELLAR"

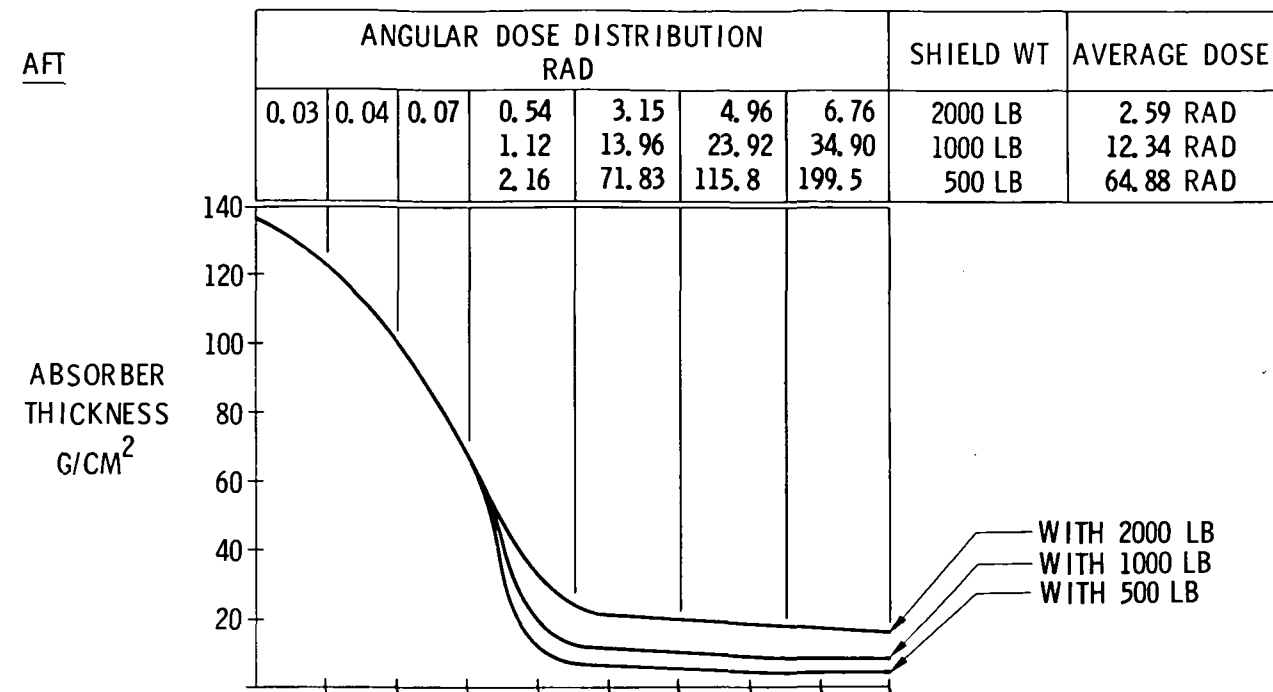
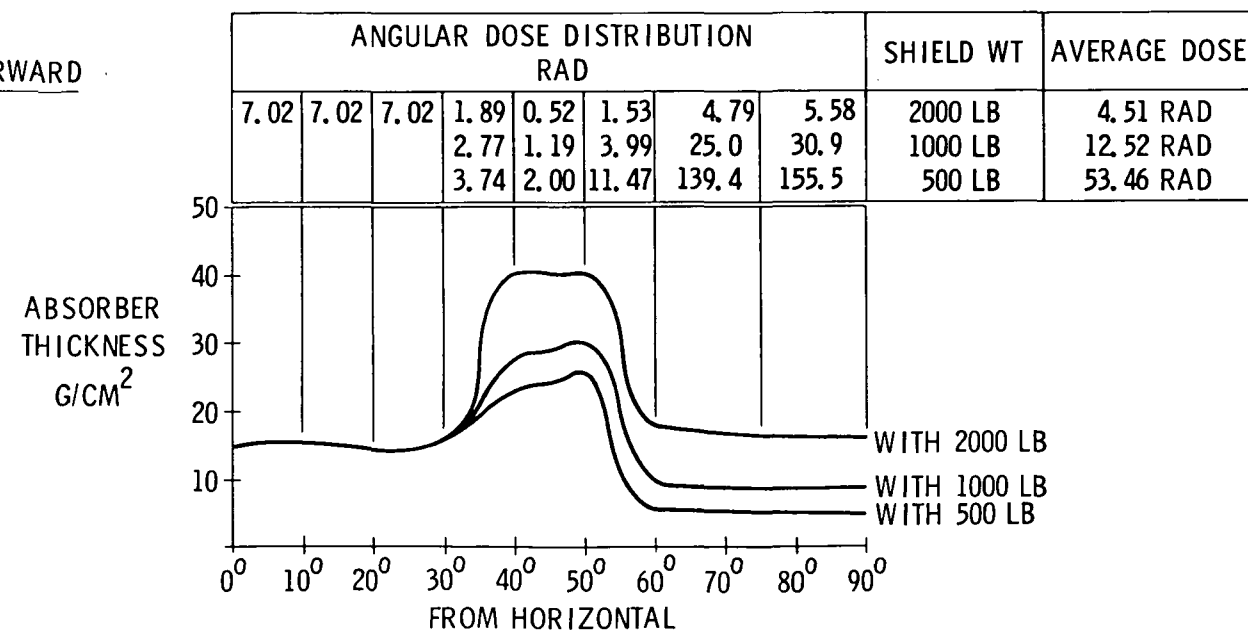
(NO MISSION MODULE EQUIPMENT CONSIDERED  
CLASS 3+ FLARE - 5/10/59)AFTFORWARD

Fig. VI-5. Solar Flare Radiation Dose Inside Storm Cellar

~~CONFIDENTIAL~~

~~CONFIDENTIAL~~

## Solar Flare Proton Emergent Energy Spectrum Inside M-1-1 Command Module\*

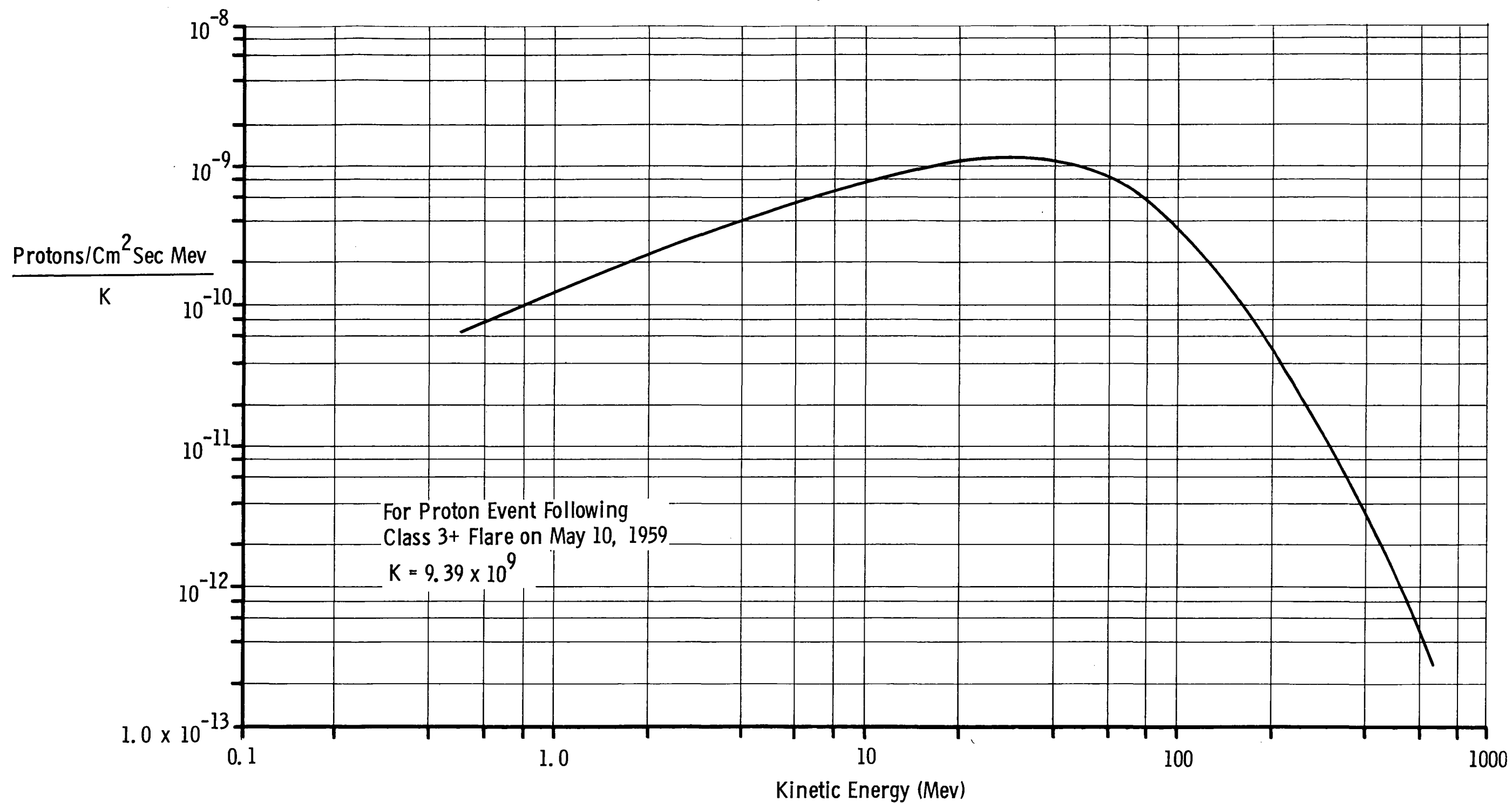
From Incident Spectrum of the Form  $KE^{-4.8}$ \*With Internal Equipment of 4 Gm/Cm<sup>2</sup>

Fig. VI-6. Solar Flare Proton Emergent Energy

~~CONFIDENTIAL~~

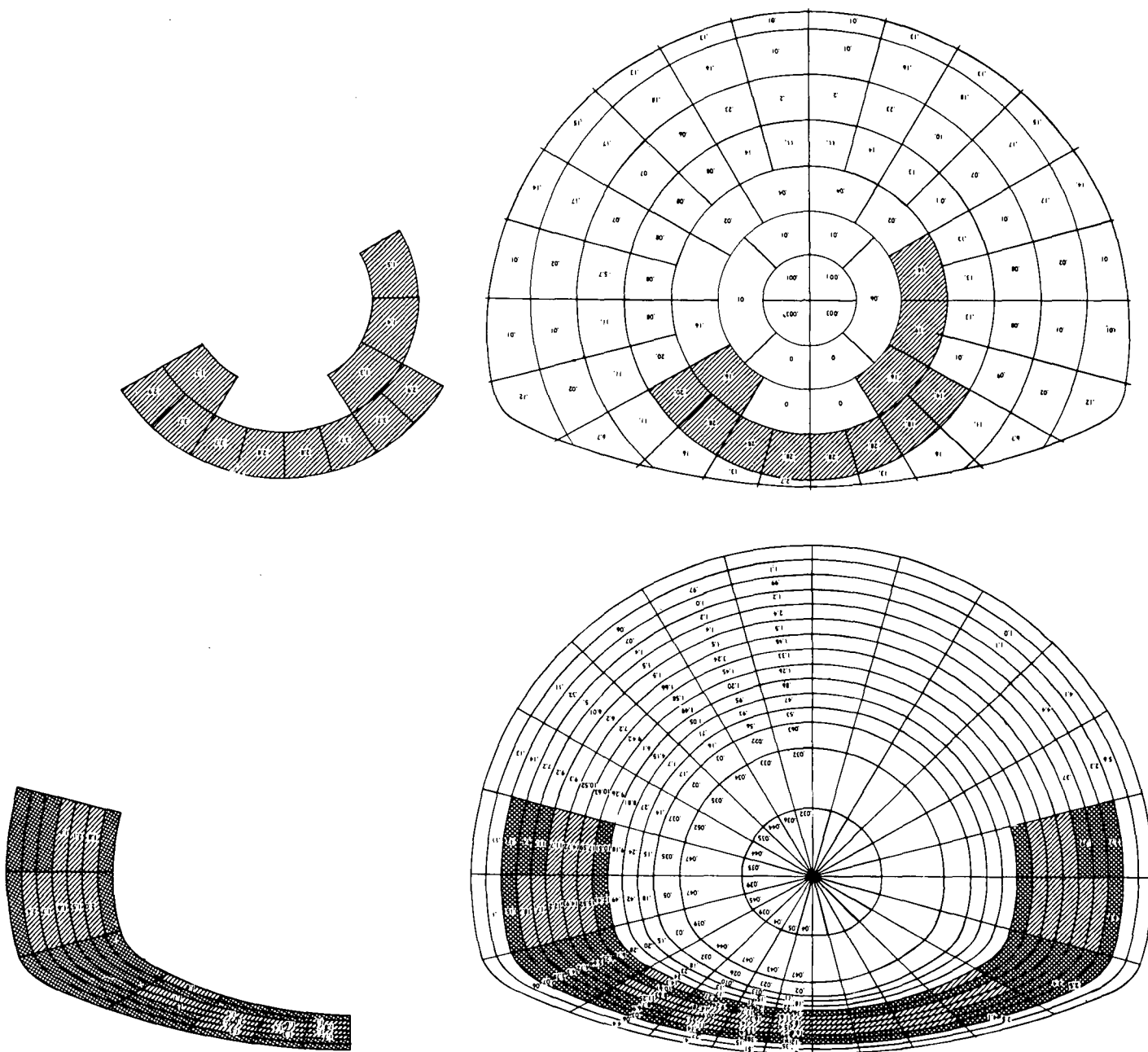


Fig. VI-7. Model 410 Command Module Dose Distribution



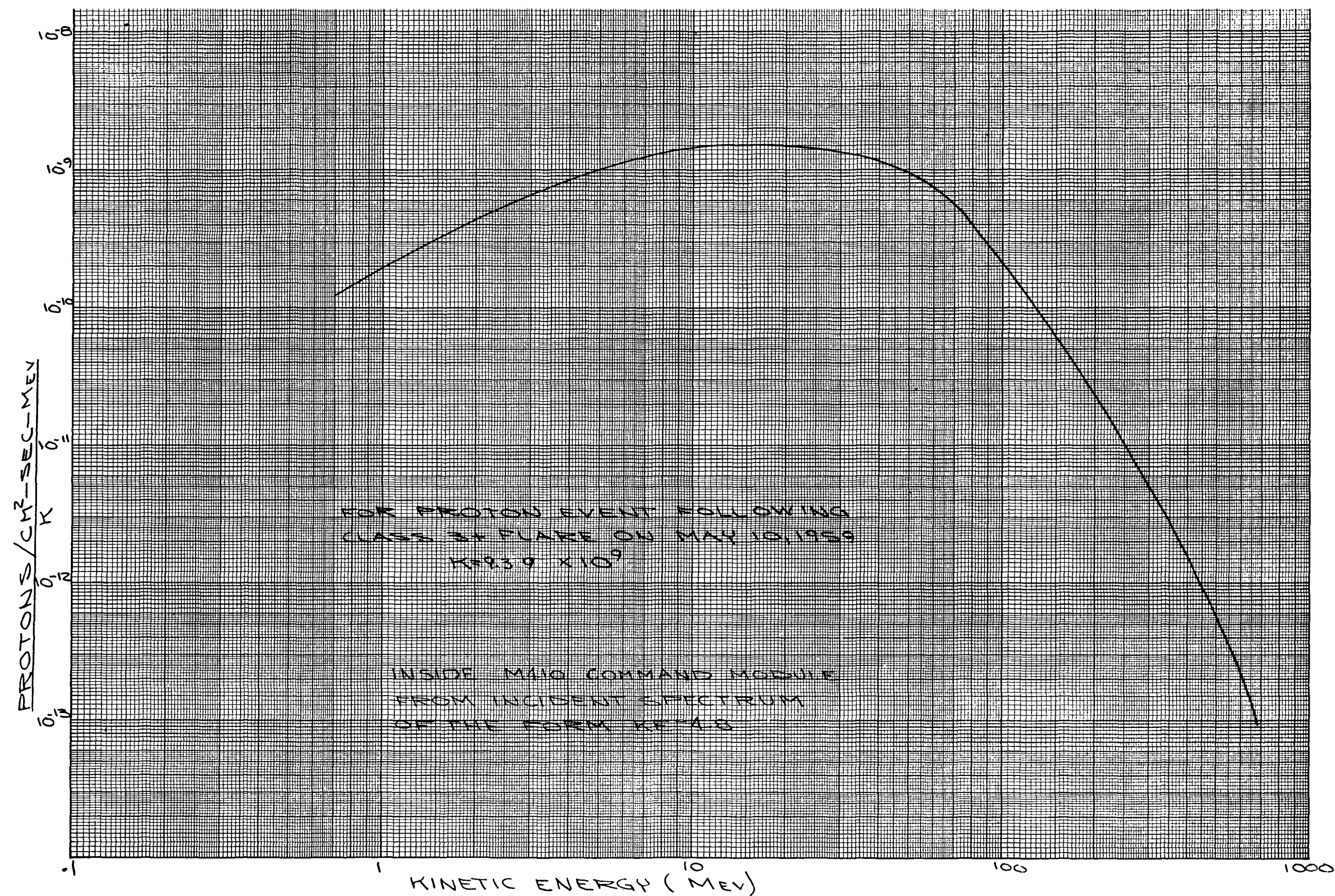
~~CONFIDENTIAL~~

Fig. VI-8. Solar Flare Proton Emergent Energy Spectrum

~~CONFIDENTIAL~~

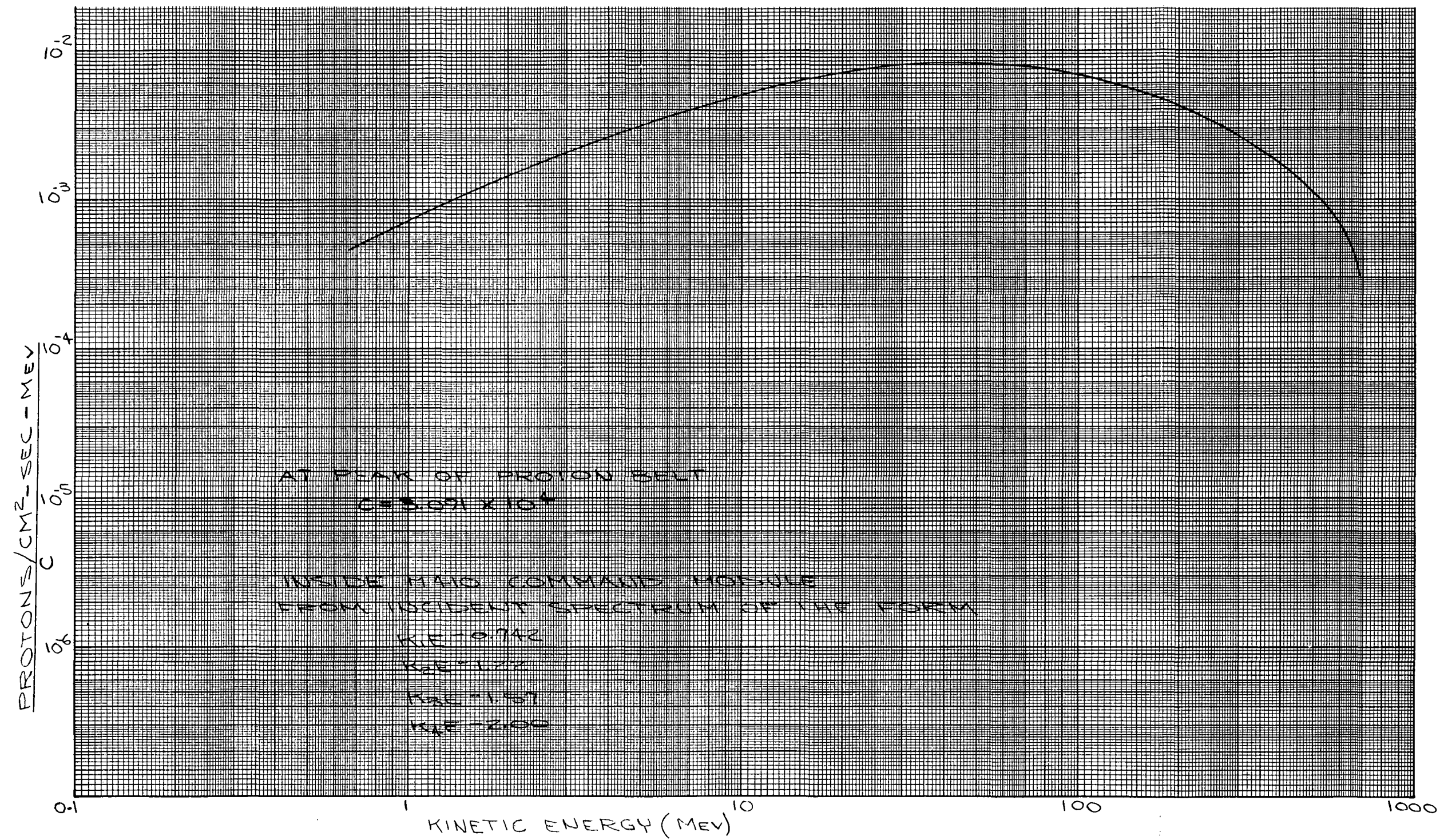


Fig. VI-9. Van Allen Belt Proton Emergent Energy Spectrum

~~CONFIDENTIAL~~



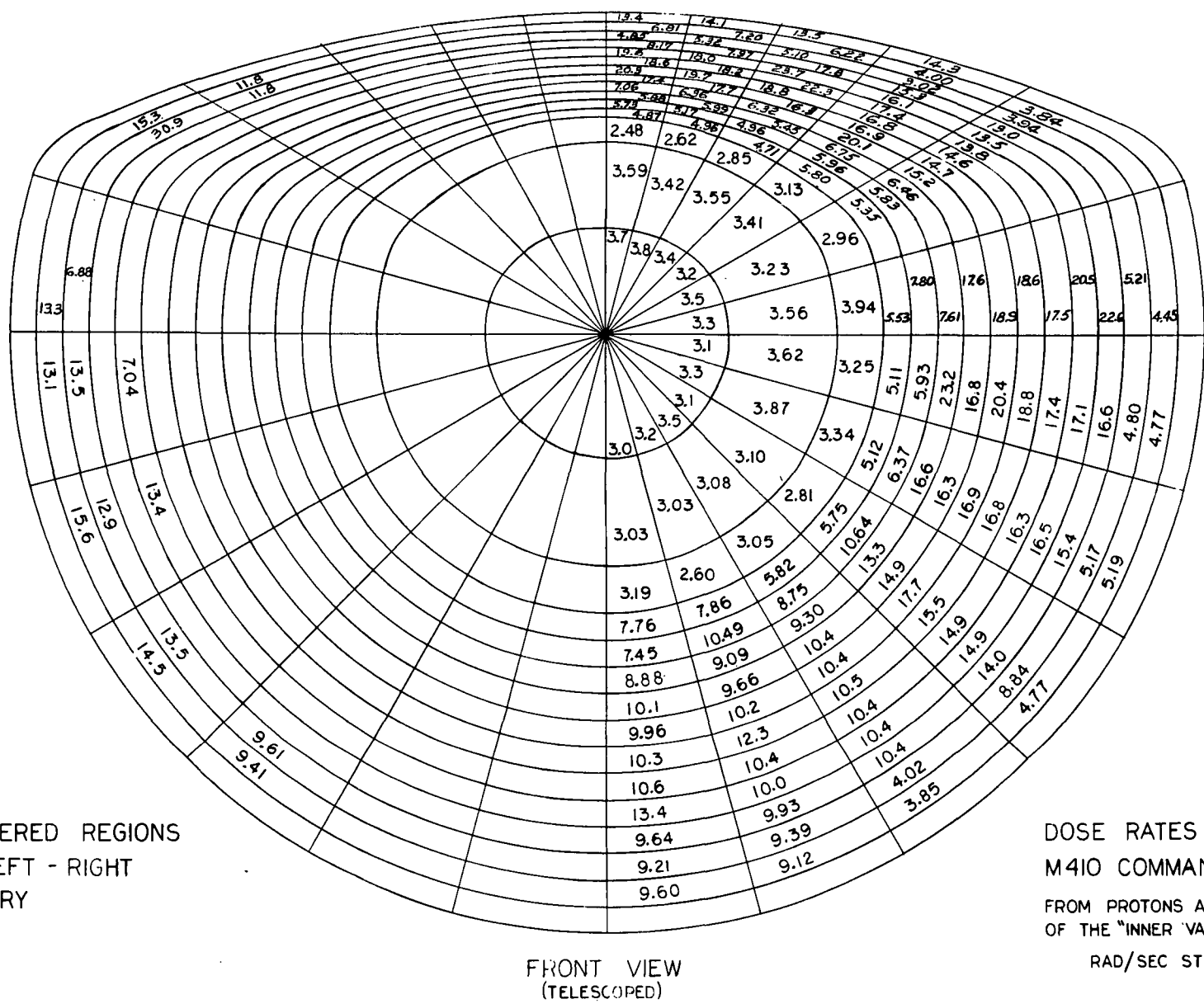


Fig. VI-10. Dose Rates Inside Model 410 Command Module

**CONFIDENTIAL**

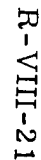


Fig. VI-10. Dose Rates Inside Model 410 Command Module (continued)

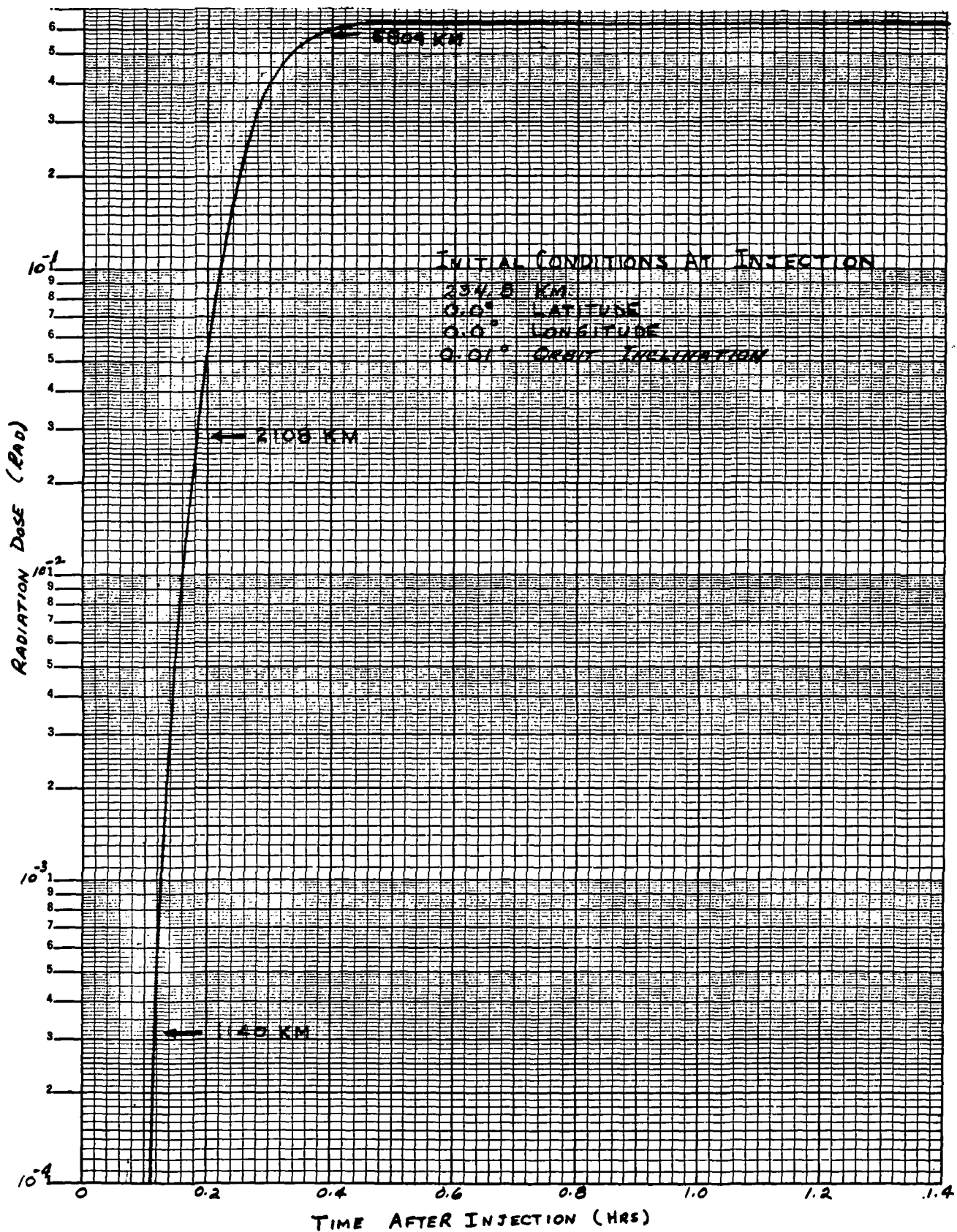


Fig. VI-11. Van Allen Belt Proton Dose Within Model 410 (case a)

~~CONFIDENTIAL~~

ER 12018

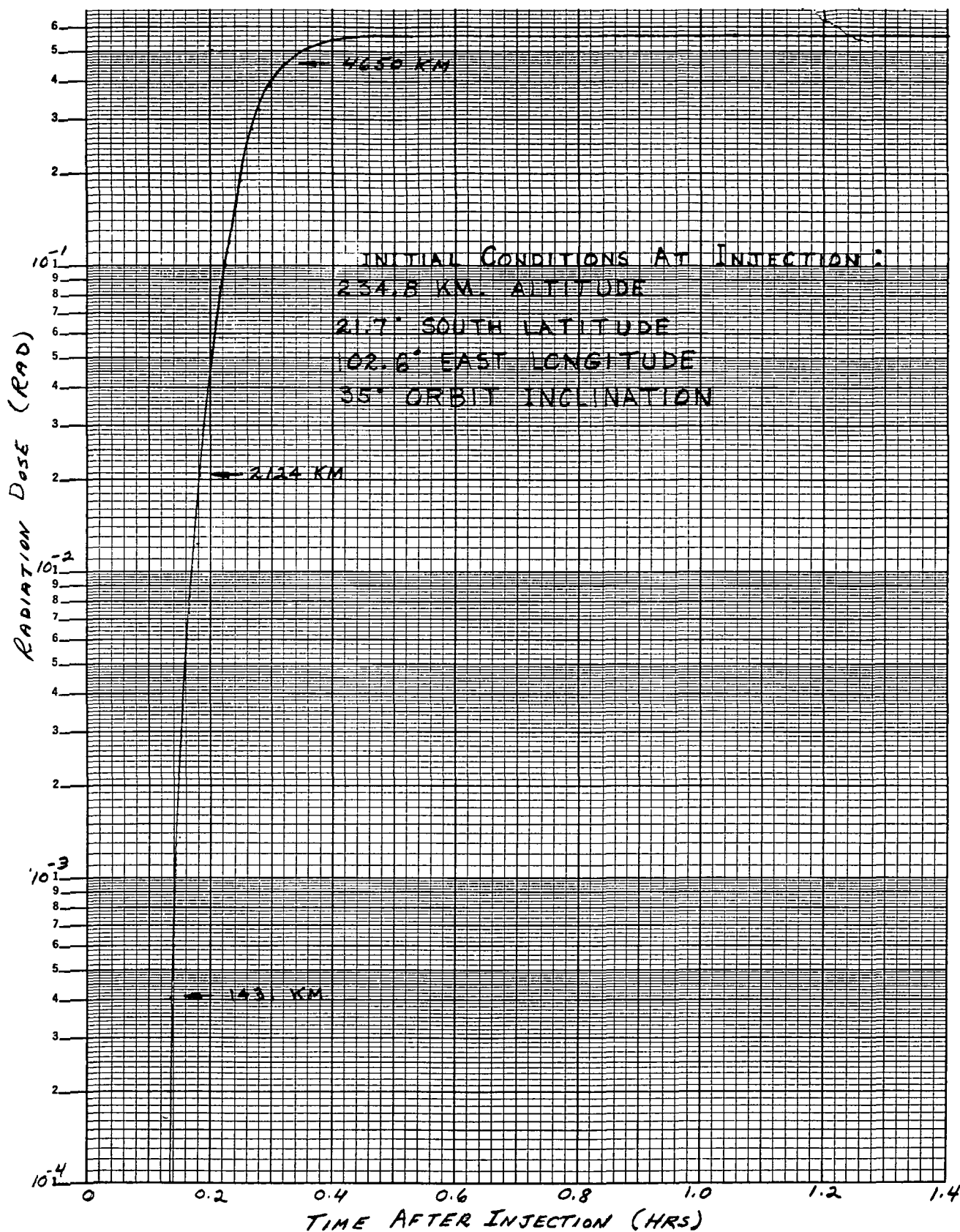


Fig. VI-12. Van Allen Belt Proton Dose Within Model 410 (case b)

~~CONFIDENTIAL~~

ER 12018

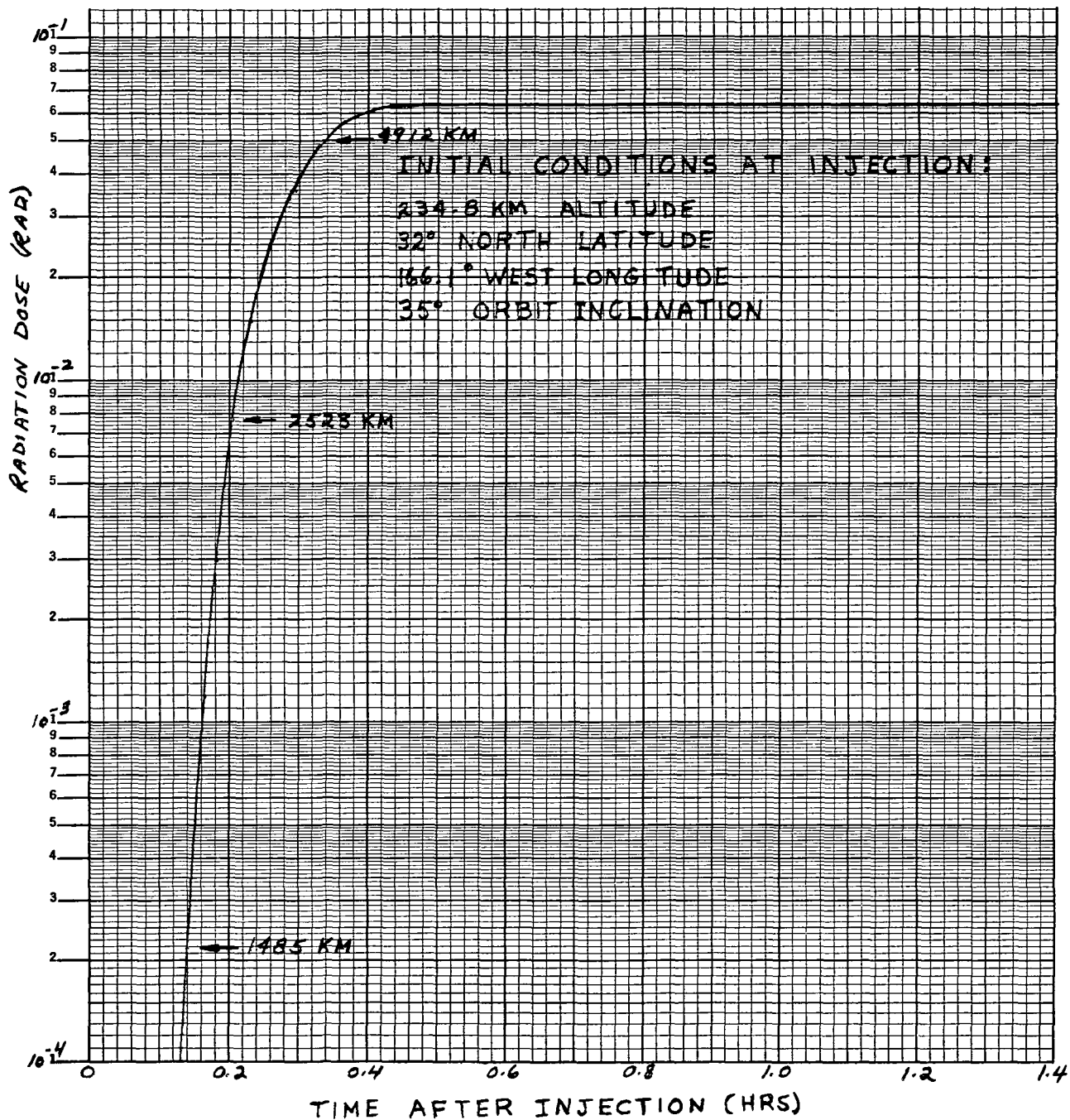
~~CONFIDENTIAL~~

Fig. VI-13. Van Allen Belt Proton Dose Within Model 410 (case c)

~~CONFIDENTIAL~~

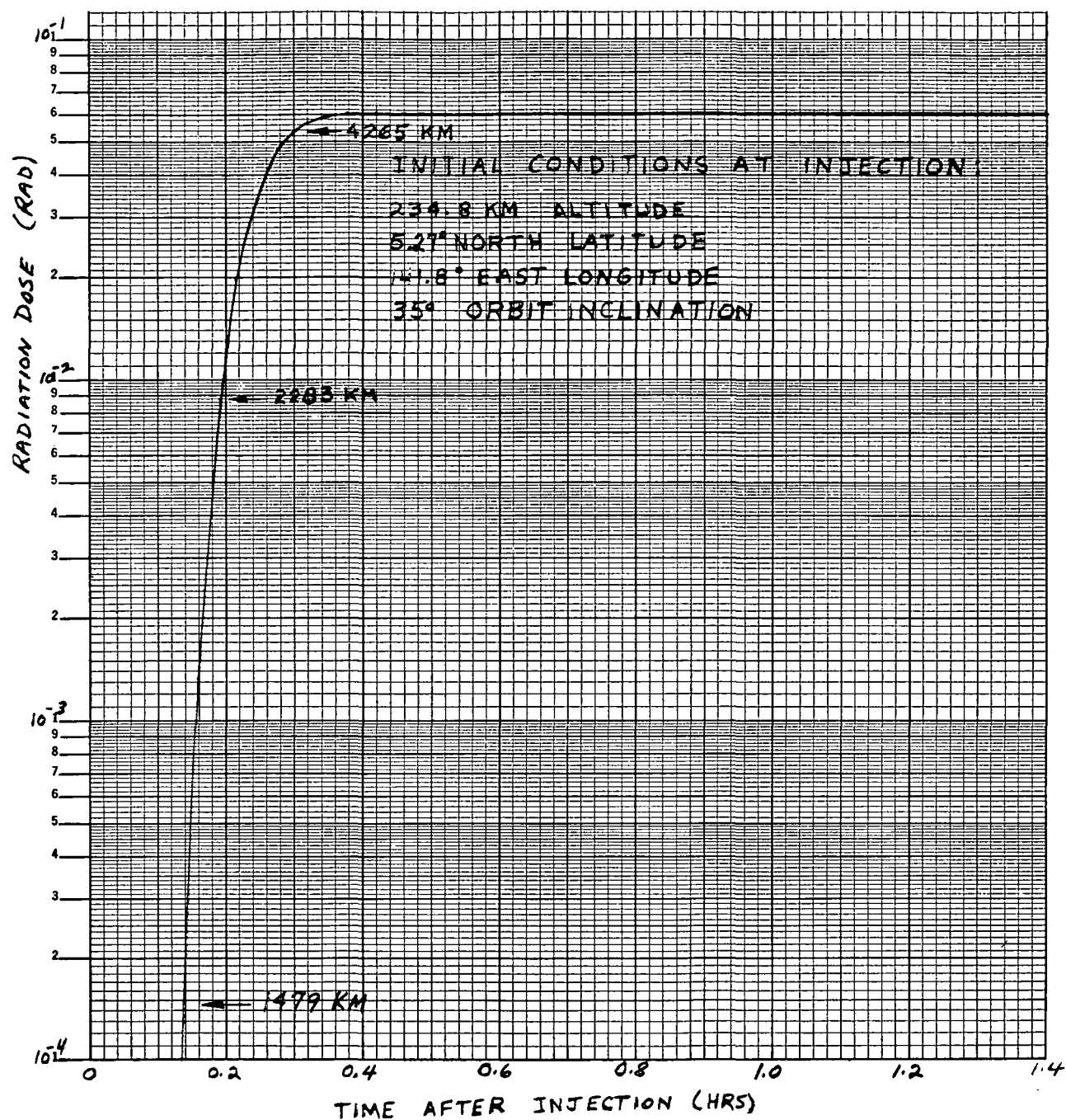


Fig. VI-14. Van Allen Belt Proton Dose Within Model 410 (case d)

CONFIDENTIAL

ER 12018



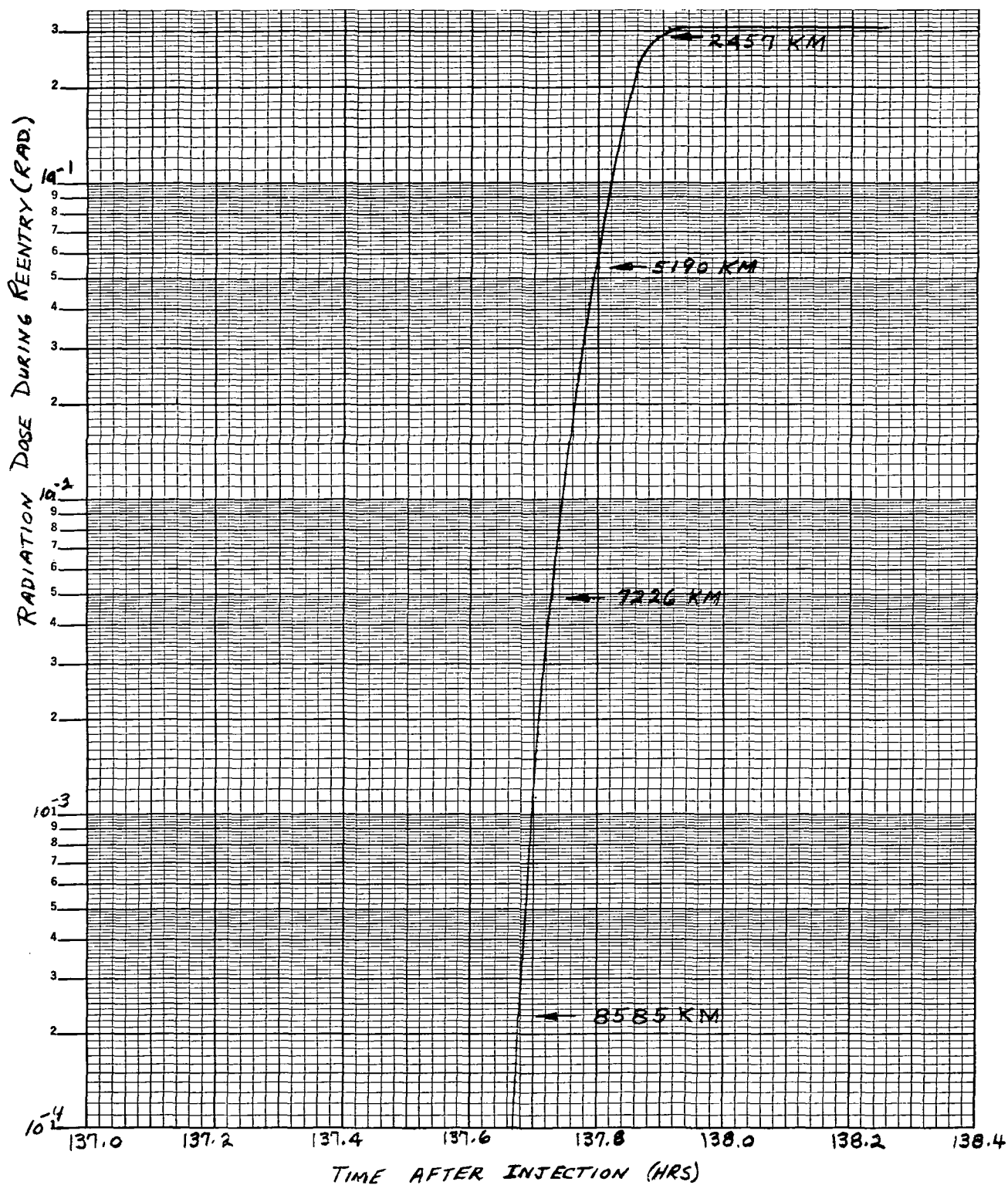
~~CONFIDENTIAL~~

Fig. VI-15. Van Allen Belt Proton Dose Within Model 410 (case e)

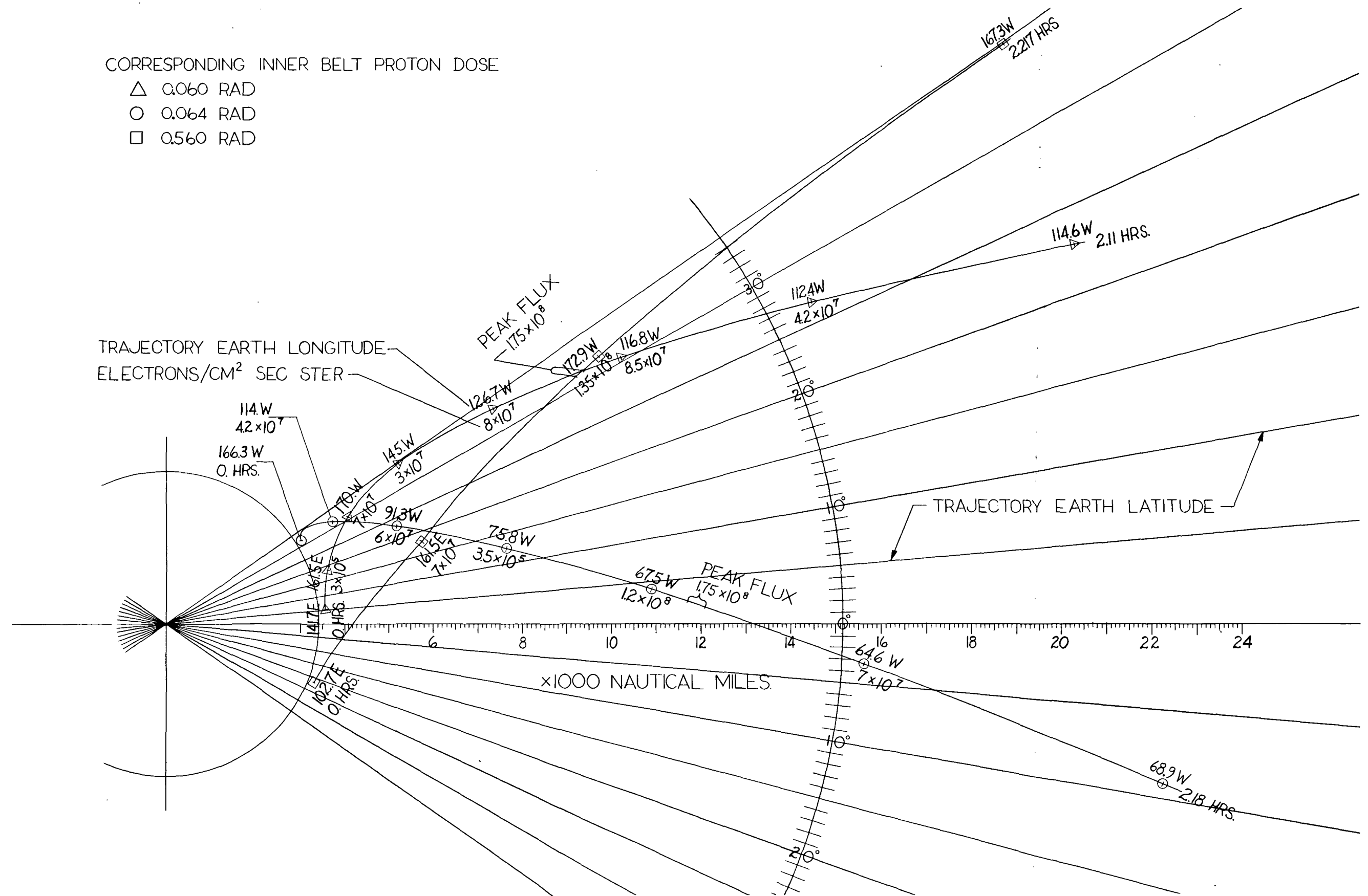


Fig. VI-16. Outer Belt Electron Flux Encountered on Three Lunar Trajectories

~~CONFIDENTIAL~~

~~CONFIDENTIAL~~

M-i

## PART II: Meteorite Environment

~~CONFIDENTIAL~~

ER 12018

~~CONFIDENTIAL~~

~~CONFIDENTIAL~~

~~CONFIDENTIAL~~

## SUMMARY

An investigation of the problem of meteorite impacts on the Apollo spacecraft indicates the effects of such impacts will be a major design consideration. The study analyses were aimed at the probability of no penetration of various critical components of the spacecraft.

Whipple's 1957 meteorite model (Ref. 1), used in the analyses, is the more comprehensive of the various investigations and is presented in a form suitable for engineering purposes. The Whipple 1957 model is compared with the more recent data of Bjork (Ref. 2) and Jonah (Ref. 3). Both models show an increase in the flux density of the meteorites over that of Whipple for the range of design meteorites for the spacecraft and will warrant further investigation as more data become available.

The probability analysis methods of Naumann (Ref. 5) were used in the investigation to establish the probability of meteorite impacts of given sizes according to Whipple's model. Using Naumann's methods, it was possible to determine the design meteorite in relation to the exposed surface area of the spacecraft component including time of exposure and the probability of no penetration.

To determine the skin thicknesses needed to resist meteorite penetration, Summers' equation (Ref. 7) was used. This equation was selected because of its satisfactory correlation with impact test data over a wide range of velocities (up to 32,000 ft/sec) and projectile-to-target density ratios. The various other penetration formulae (Whipple's, Bjork's and Kornhauser's) were compared for their penetration values for Whipple model meteorites. A wide range of penetration values was found. Summers' equation gives the penetration of a given projectile into a thick target. The required thin skin thickness for resisting penetration by a projectile was taken as twice the penetration in a thick target.

The design overall probability of no penetration of the critical components of the spacecraft was selected as 0.95 for a 14-day lunar orbit mission. The analysis showed that to obtain a 0.95 probability of no penetration without a significant weight penalty, the critical components would need protection with a meteorite "bumper" shield. In the study analysis, a bumper shield of proper design was assumed to allow the total skin (shield and structural) thickness to be one-third of a single thick skin. An 0.040-in. aluminum alloy skin surrounds the critical components of the propulsion and equipment module and the mission engine components (Fig. I-10). The heat shield acts as a bumper shield for the command module pressure vessel.

~~CONFIDENTIAL~~

The study analyses show that the spacecraft has an 0.95 overall probability of no penetration (approximate) for the critical components during a 14-day lunar orbit mission. This value was based on the assumption of no earth shielding, no mutual components shielding by each other and penetration based on meteorite impacts normal to the surface.

Some recommendations are given for future effort required to obtain a better definition of the meteorite environment and the penetration mechanism due to hypervelocity impacts.

~~CONFIDENTIAL~~

ER 12018

## I. METEORITE ENVIRONMENT

The spacecraft is subjected to meteorite impacts during travel in space. These meteorites consist of particles of stone, iron or nickel of high density, and probably low-density particles of the fragile dustball type. The dustballs are believed to outnumber all other types. These particles are known to vary from large objects weighing many tons to fine dust which settles on the earth. The meteorites, estimated to have velocities in the order of 11 to 72 km/sec, have orbits around the sun. Most knowledge of meteorites is based on visual, photographic and radio observations of the entry of meteorites into the atmosphere. Data also have been obtained from satellite probes. Because of this, knowledge of the meteorite environment in space is limited, and the meteorite environment selected for design of the spacecraft is somewhat arbitrary.

Of the partial models for meteorite environment, Whipple's 1957 model (Ref. 1) appears most suitable for design purposes. This model uses a meteorite density of 0.05 gm/cu cm and an average velocity of 28 km/sec for the larger bodies, decreasing to 15 km/sec for the dust particles. Table I-1, derived from Ref. 1, defines the Whipple 1957 meteorite model. Figure I-1 shows a plot of the meteorite mass in relation to the flux density of Whipple's model, and the more recent models of Bjork (Ref. 2) and Jonah (Ref. 3). Bjork's model uses the same mass and velocity as Whipple's model, but the flux density is based on data from Explorer I and Vanguard III, and a conservative assumption is made that the meteorites have the density of stone (about 2.8 gm/cu cm). Jonah (Ref. 3) has based his model on available data on atmospheric properties, IGY meteor observation programs, high altitude rocket probes, satellite impact counts and other sources. The zero magnitude meteorite has a mass of 16.8 grams, compared to 25 grams for Whipple's. Jonah indicates the density of the meteorites in the magnitude range from 0 to 15 is 0.3 gm/cu cm, and the average velocity for various magnitudes approaches Whipple's velocities. The range of design meteorites for the vehicle varies from visual magnitude 7 to 16 using Whipple's model. From Fig. I-1, both Bjork's and Jonah's models show an increase in flux density over Whipple's model.

For the design study analysis, Whipple's model was selected because it is more definitive in the relation of mass, velocity, density and flux of the meteorites. Jonah's model merits additional investigation as further data becomes available. Another consideration in the meteorite environment is the apparent decrease of flux density with the increase in distance from the earth, as indicated by Whipple (Ref. 4). This effect is not included in Whipple's 1957 model and has been neglected in the study analysis.

### A. PROBABILITY ANALYSIS OF METEORITE IMPACTS

Whipple's 1957 meteorite model gives flux density versus visual magnitudes. To calculate hit probabilities, recourse must be made to probability methods of analysis.



~~CONFIDENTIAL~~

TABLE I-1

Whipple's 1957 Meteorite Model

Meteorite Density = 0.05 gm/cu cm

Visual Magnitude	Meteorite Mass (g)	Diameter (in.)	Velocity (ft/sec)	Number Striking (sq ft/day)
0	25.0	3.88	92,000	$3.55 \times 10^{-10}$
1	9.95	2.86	92,000	$8.92 \times 10^{-10}$
2	3.96	2.10	92,000	$2.24 \times 10^{-9}$
3	1.58	1.55	92,000	$5.63 \times 10^{-9}$
4	0.628	1.14	92,000	$1.41 \times 10^{-8}$
5	0.250	0.835	92,000	$3.55 \times 10^{-8}$
6	$9.95 \times 10^{-2}$	0.615	92,000	$8.92 \times 10^{-8}$
7	$3.96 \times 10^{-2}$	0.453	92,000	$2.24 \times 10^{-7}$
8	$1.58 \times 10^{-2}$	0.333	88,600	$5.63 \times 10^{-7}$
9	$6.28 \times 10^{-3}$	0.246	85,200	$1.41 \times 10^{-6}$
10	$2.50 \times 10^{-3}$	0.181	82,000	$3.55 \times 10^{-6}$
11	$9.95 \times 10^{-4}$	0.133	78,900	$8.92 \times 10^{-6}$
12	$3.96 \times 10^{-4}$	0.098	75,800	$2.24 \times 10^{-5}$
13	$1.58 \times 10^{-4}$	0.072	72,100	$5.63 \times 10^{-5}$
14	$6.28 \times 10^{-5}$	0.053	69,000	$1.41 \times 10^{-4}$
15	$2.50 \times 10^{-5}$	0.039	65,800	$3.55 \times 10^{-4}$
16	$9.95 \times 10^{-6}$	0.029	62,300	$8.92 \times 10^{-4}$
17	$3.96 \times 10^{-6}$	0.021	59,100	$2.24 \times 10^{-3}$
18	$1.58 \times 10^{-6}$	0.016	55,900	$5.63 \times 10^{-2}$
19	$6.28 \times 10^{-7}$	0.0114	52,800	$1.41 \times 10^{-2}$
20	$2.50 \times 10^{-7}$	0.0084	49,300	$3.55 \times 10^{-2}$
21	$9.95 \times 10^{-8}$	0.00615	49,300	$8.92 \times 10^{-2}$
22	$3.96 \times 10^{-8}$	0.00452	49,300	$2.24 \times 10^{-1}$
23	$1.58 \times 10^{-8}$	0.00314	49,300	$5.63 \times 10^{-1}$
24	$6.28 \times 10^{-9}$	0.00198	49,300	$1.41 \times 10^0$
25	$2.50 \times 10^{-9}$	0.00125	49,300	$3.55 \times 10^0$
26	$9.95 \times 10^{-10}$	0.00079	49,300	$8.92 \times 10^0$
27	$3.96 \times 10^{-10}$	0.000497	49,300	$2.24 \times 10^1$
28	$1.58 \times 10^{-10}$	0.000314	49,300	$5.63 \times 10^1$
29	$6.28 \times 10^{-11}$	0.000198	49,300	$1.41 \times 10^2$
30	$2.50 \times 10^{-11}$	0.000124	49,300	$3.55 \times 10^2$
31	$9.95 \times 10^{-12}$	0.000079	49,300	$8.92 \times 10^2$

1 pound = 453.6 grams

Ref: Table I of Ref. 1

~~CONFIDENTIAL~~

The method in the study was based on the analysis by Naumann (Ref. 5). On the assumption (according to Whipple's model) that the number of meteorites increases by a factor of  $10^{0.4}$  per magnitude step, the equation for the number at any magnitude (m) is

$$N_m = N_0 \times 10^{0.4m}$$

where  $N_0$  = the number of zero magnitude meteorites.

However, if magnitude ( $m_c$ ) is sufficient to penetrate the skin of the spacecraft, then anything larger ( $m < m_c$ ) also will penetrate. It is necessary to express the total number ( $N_t$ ), which is the sum of all magnitudes up to and including  $m_c$ , as

$$N_t = N_0 \times 10^{0.4 m_c} + N_0^{0.4 (m_c - 1)} + \dots \quad (2)$$

The general expression becomes

$$N_t = \sum_{j=0}^{\infty} N_0 \times 10^{0.4 (m_c - j)}, \quad (3)$$

Since  $10^{0.4} = 2.512$ ,

$$N_t = N_0 \times \sum_{j=0}^{\infty} 2.512^{(m_c - j)} = 2.512^{m_c} N_0 \times \sum_{j=0}^{\infty} \frac{1}{2.512^j}$$

which is a geometric series and is convergent since  $\frac{1}{2.512} < 1$ .

$$\sum_{j=0}^{\infty} (r)^j = \frac{1}{1-r} = \frac{1}{1 - \frac{1}{2.512}} = 1.6614 \quad (4)$$

$$N_t = 1.6614 \times 2.512^{m_c} \times N_0 \quad (5)$$

Whipple gives the value of  $N_t$  up to magnitude 5 as  $2 \times 10^8$  meteorites striking the earth per day. The value of  $N_0$  can now be found by using Eq (5)

$$2 \times 10^8 = 1.6614 \times 2.512^5 \times N_0 \quad (6)$$

$$N_0 = 1.2 \times 10^6 \quad (7)$$

~~CONFIDENTIAL~~

where  $N_0$  = the number of zero magnitude meteorites striking the earth in one day.

The number of hits per day on a surface ( $A_s$ ) by meteorites of magnitude up to and including ( $m_c$ ) can be written as

$$n = \frac{N_t A_s}{A_e} = \frac{1.6614 \times 2.512^{m_c} \times N_0 \times A_s}{A_e} \quad (8)$$

where  $A_e$  = area of the atmosphere sphere

Assuming a Poisson distribution, the probability of exactly ( $h$ ) hits in ( $T$ ) days is

$$P(h) = \frac{(nT)^h e^{-nT}}{h!} \quad (9)$$

Instead of summing  $P(1) + P(2) + P(3) + \dots + P(n)$ , the probability of no hits ( $P_0$ ) will be calculated.

The probability of one or more hits denoted by  $P_+$  is:

$$P_+ = 1 - P_0 \quad (10)$$

and the probability of zero hits is

$$P_0 = e^{-nT} = e^{-N_t A_s T / A_e} \quad (11)$$

Since most meteors are observed at 80 kilometer altitude and the radius of the earth is 6371 kilometers, the area of the atmospheric sphere is

$$A_e = 4\pi (6371 + 80)^2 = 522.689 \times 10^6 \text{ sq km.} \quad (12)$$

Combining the  $N_t/A_e$  term in Eq (11)

$$\frac{N_t}{A_e} = \frac{1.6614 \times 1.2 \times 10^6 \times 10^{0.4 m_c}}{522.689 \times 10^6} \text{ number/sq km/day} \quad (13)$$

$$\begin{aligned} \frac{N_t}{A_e} &= 3.813 \times 10^{-9} \times 10^{0.4 m_c} \text{ number/sq m/day} \\ &= 3.813 \times 10^{(0.4 m_c - 9)} \text{ number/sq m/day.} \end{aligned} \quad (14)$$

Substituting the value of  $\frac{N_t}{A_e}$  in Eq (11),  $P_0$  may be written

$$P_0 = \left[ e^{-3.813 \times 10^{(0.4 m_c - 9)} A_s T} \right] \quad (15)$$

~~CONFIDENTIAL~~

Letting  $x = -3.813 \times 10^{(0.4 m_c - 9)}$  and expanding  $e^x$  gives

$$e^x = 1 + x + \frac{x^2}{2!} + \frac{x^3}{3!} + \dots$$

For  $m_c \leq 20$ ,  $x$  is small and therefore  $x^2$  and higher order terms may be dropped and  $P_0$  becomes

$$P_0 = \left[ 1 - 3.813 \times 10^{(0.4 m_c - 9)} \right] A_s T. \quad (16)$$

The probability of no hits on one square meter surface area in one day (i.e.,  $A_s T = 1$ ) is

$$p_0 = \left[ 1 - 3.813 \times 10^{(0.4 m_c - 9)} \right]. \quad (17)$$

The probability of one or more hits on one square meter in one day is

$$p_+ = 1 - p_0 = 3.813 \times 10^{(0.4 m_c - 9)} \quad (18)$$

where  $m_c$  = the visual magnitude of the meteorite just sufficient to puncture the skin of the spacecraft.

Equation (16) becomes

$$P_0 = (p_0)^{A_s T} \quad (19)$$

$$\text{or } P_0 = (1 - p_+)^{A_s T}. \quad (20)$$

Expanding Eq (20) binomially

$$P_0 = 1 - (A_s T p_+) + \left[ \frac{A_s T (A_s T - 1) p_+^2}{2!} \right] \dots \quad (21)$$

If  $p_+$  is small,  $p_+^2$  and the higher order terms may be neglected

$$P_0 = 1 - A_s T p_+. \quad (22)$$

Substituting Eq (10) in Eq (22)

$$1 - P_+ = 1 - A_s T p_+$$

$$P_+ = A_s T p_+ \quad (23)$$

Eq (23) is a good approximation if the product  $A_s T p_+ < 1.0$ .

~~CONFIDENTIAL~~

If  $A_s T p_+ > 1.0$ , Eq (19) must be written

$$\log_{10} P_0 = A_s T \log_{10} P_0 . \quad (24)$$

Where  $A_s$  = the effective area exposed to meteorite penetration.

For a satellite in close orbit around the earth, approximately one-half of its area is shielded by the earth.

Figures I-2a and I-2b are plots of Eq (18) and show the variation of the probability of one or more hits on a square meter in a day with the meteorite visual magnitude. To find the visual magnitude ( $m_0$ ) of the "design" meteorite that the spacecraft skin must resist for a desired probability of no penetration ( $P_0$ ), and for a given value of exposure ( $A_s T$ ), Eq (23) gives  $P_+ = A_s T p_+$  and can be written as  $1 - P_0 = A_s T p_+$

$$\text{or } P_0 = 1 - A_s T p_+ \text{ from which} \quad (25)$$

$$p_+ = \frac{1 - P_0}{A_s T} . \quad (26)$$

Knowing the value of  $p_+$ , the design visual magnitude can be found from Figs. I-2a and I-2b.

For example, if the desired value of  $P_0 = 0.95$  and  $A_s T = 100$  square meters X 14 days = 1400

$$p_+ = \frac{1 - 0.95}{1400} = \frac{0.05}{1400} = 3.58 \times 10^{-5}$$

and, from Fig. I-2a, the design visual magnitude is found to be 9.95.

Fig. I-3 is a plot of the visual magnitude of the design meteorite for various values of the probability of no penetration versus the exposed area multiplied by the time. For convenience, the value of  $A_s T$  given on Fig. I-3 is in square feet and days.

## B. PENETRATION EQUATIONS

After the design meteorite is found by using Fig. I-3 the skin thickness needed to resist penetration by the meteorite is determined. Table I-1 gives the mass, diameter, density and velocity of a given meteorite. With these parameters the penetration in a given target material can be calculated, if a penetration equation is known.

~~CONFIDENTIAL~~

This "if" is a large one because no experimental impact data is available at meteorite velocities and densities.

Various investigators have advanced penetration equations, some based on empirical equations derived from test data, some on theoretical considerations, but nearly all give the penetration in a thick target. Because the structural skins of the spacecraft are of aluminum alloy, the primary problem is the penetration of meteorites into aluminum. Four penetration equations are investigated for a comparison of the meteorite penetrations given by the different equations. These equations follow.

(1) Whipple's Equation -- Ref. (1)

$$P = \left[ \frac{(9)}{\pi \rho \xi} \right]^{1/3} E^{1/3} \quad (27)$$

where P = penetration in a thick target, ft

E = meteorite energy, ft-lb

$\rho$  = target density, lb/cu ft

$\xi$  = heat to fusion of target material, ft-lb/lb

For a meteorite of diameter (d) inches moving at a velocity (V) ft/sec and with a density  $\rho_M = 0.05$  g/cu cm = 0.001808 lb/cu in. and  $\xi = 447$  but/lb = 348,000 ft-lb/lb can be found from

$$E = 1/2 \times \frac{W}{g} \times V^2 \text{ and } W = 1728 \times \rho_M \times \frac{\pi}{6} \times \left[ \frac{d}{12} \right]^3$$

$$E = \frac{1/2 \times .524 \rho_M d^3 \times V^2}{32.2}$$

$$E = 0.00814 \rho_M d^3 V^2 \quad (28)$$

$$\text{and } P = \frac{(9 \times .00814 \rho_M d^3 V^2)^{1/3}}{\pi \times \rho_T \times \xi}$$

$$P = \left[ \frac{(9 \times .00814 \times .001808 d^3 V^2)}{(\pi \times .101 \times 348,000)} \right]^{1/3}$$

$$P = 10.62 \times 10^{-4} d V^{2/3}$$

$$\text{or } \frac{P}{d} = 10.62 \times 10^{-4} V^{2/3} \quad (29)$$

~~CONFIDENTIAL~~

where

P = penetration in thick target, inches

d = meteorite diameter, inches

V = meteorite velocity, ft/sec.

Whipple's equation is theoretical and is believed to give penetration depths for hypervelocity impacts that are too high.

(2) Kornhauser's Equation -- Ref. (6)

$$h = 2 \left[ \frac{(U)}{(E)} \right]^{1/3} \left[ \frac{(E)}{(E_0)} \right]^{0.09} \quad (30)$$

where

h = penetration (depth of crater), inches

U = kinetic energy of projectile, in.-lb

E = modulus of elasticity of target material, psi

$E_0$  = reference modulus,  $10^6$  psi

for aluminum alloy targets,  $E = 10.5 \times 10^6$  psi

$$\therefore h = 2 \left[ \frac{(U)}{(10.5 \times 10^6)} \right]^{1/3} \left[ \frac{(10.5 \times 10^6)}{(10^6)} \right]^{1/3}$$

$h = 0.01128 U^{1/3}$  and from Eq (28) the kinetic energy of meteorites is (31)

$$U = .00814 \rho_M d^3 V^2 \text{ and } \therefore \text{ for } \rho_M = 0.05 \text{ g/cu cm} = 0.001808 \text{ lb/cu in.}$$

$$\therefore U = 14.7 \times 10^{-6} d^3 V^2 \quad (32)$$

Substituting the value of U from Eq (32) into Eq (31), we have

$$\begin{aligned} h &= 0.01128 (14.7 \times 10^{-6} d^3 V^2)^{1/3} \\ h &= 2.76 \times 10^{-4} d V^{2/3} \\ \text{or } \frac{h}{d} &= 2.76 \times 10^{-4} V^{2/3} \end{aligned} \quad (33)$$

This equation is similar to Whipple's except the value of the constant is lower.

~~CONFIDENTIAL~~

(3) Summers' Equation - This is an empirical equation based on experimental test data using many different projectile and target material combinations. As given in Ref. (7), the equation has the form of

$$\frac{P}{d} = 2.28 \left[ \frac{(\rho_p)}{(\rho_t)} \right]^{2/3} \left[ \frac{(V)}{(C)} \right]^{2/3} \quad (34)$$

where

P = penetration in a thick target, inches

d = diameter of projectile, inches

$\rho_p$  = density of projectile, lb/cu in.

$\rho_t$  = density of target, lb/cu in.

V = projectile velocity, ft/sec

C = speed of sound in target material, ft/sec.

For Whipple's meteorite density of  $\rho_p = .05 \text{ g/cu cm} = 0.001808 \text{ lb/cu in.}$  and for an aluminum target ( $\rho_t = .101 \text{ lb/cu in.,}$   $C = 16,740 \text{ ft/sec}$ ) Eq (34) reduces to

$$\begin{aligned} \frac{P}{d} &= 2.28 \left[ \frac{(.001808)}{(.101)} \right]^{2/3} \left[ \frac{(V)}{(16,740)} \right]^{2/3} \\ &= 2.28 \times .0684 \times \frac{1}{655} V^{2/3} \\ P &= 2.38 \times 10^{-4} V^{2/3}. \end{aligned} \quad (35)$$

This is close to the value given by Kornhauser, Eq (33).

(4) Bjork's Equation - This is a theoretical equation developed (Ref. 8), using a hydrodynamic model to explain hypervelocity impact. Equations were derived for the impact of aluminum projectiles on aluminum targets and also iron projectiles on iron targets. In Ref. (2), Bjork gives the penetration of an aluminum projectile into an aluminum target as

$$P = 1.09 (m v)^{1/3}$$

where

P = penetration, cm



~~CONFIDENTIAL~~

$m$  = projectile mass, gm

$v$  = impact velocity, km/sec.

Bjork, in Ref. 10, states that the use of a correction factor of the form  $\left(\frac{s_p}{s_t}\right)$  is subject to some conjecture for it rests on no theoretical basis. He favored the value of  $\phi = 1/3$  and  $\theta = 1/3$  in a general penetration equation as

$$p \sim m^{1/3} s_t^{-\phi} s_p^{\phi-1/3} \left(\frac{v}{C}\right)^{\theta} \quad (37)$$

Letting  $K$  = a constant and equating Eq (36) and (37) and solving for  $K$ :

$$1.09 (m v)^{1/3} = K m^{1/3} s_t^{-\phi} s_p^{\phi-1/3} \left(\frac{v}{C}\right)^{\theta}$$

$$1.09 (m v)^{1/3} = K m^{1/3} s_t^{-\frac{1}{3}} s_p^{\circ} \left(\frac{v}{C}\right)^{1/3}$$

$$1.09 = K s_t^{-1/3} \left(\frac{1}{C}\right)^{1/3} \quad (38)$$

~~CONFIDENTIAL~~

For aluminum targets,  $\rho_t = 2.8 \text{ g/cu cm}$  and  $C = 5.1 \text{ km/sec}$

$$1.09 = K (2.8)^{-1/3} \left( \frac{1}{5.1} \right)^{1/3}$$

$$K = 1.09 \times 1.41 \times 1.721$$

$$K = 2.63 \quad (39)$$

Thus,

$$P = 2.63 \text{ m}^{1/3} \rho_t^{-1/3} \left( \frac{V}{C} \right)^{1/3} \quad (40)$$

where  $d$  = the meteorite diameter, cm

$$\rho_p = 0.05 \text{ g/cu cm (density)}$$

$$P = 2.63 \left( \frac{\pi}{6} \times d^3 \times \rho_p \right)^{1/3} \rho_t^{-1/3} \left( \frac{V}{C} \right)^{1/3} \quad (41)$$

$$\begin{aligned} P &= 2.63 \times .806 d \rho_p^{1/3} \rho_t^{-1/3} \left( \frac{V}{5.1} \right)^{1/3} \\ &= \frac{2.63 \times .806}{1.721} \times \left( \frac{.05}{2.8} \right)^{1/3} \times d \times V^{1/3} \\ P &= .322 d V^{1/3} \quad \text{or} \quad \frac{P}{d} = 0.322 V^{1/3} \end{aligned} \quad (42)$$

where

$P$  = penetration, cm

$d$  = meteorite dia, cm

$V$  = meteorite velocity, km/sec

Eq. (42) probably extends Bjork's work, but necessarily for comparison with the other formulas.

A comparison was made of the penetrations in a thick aluminum target as given by the four different equations for the meteorite model of Whipple with a density of  $0.05 \text{ g/cu cm}$ . The results are shown in Fig. I-4. It has been assumed that the relationships may be applied to the meteorite conditions of

~~CONFIDENTIAL~~

velocity and density. Examination of Fig. I-4 shows that Bjork's equation gives higher penetration than either Summers' or Kornhauser's equations, although Bjork's equation uses velocity to the one-third exponential compared to two-thirds for the other equations. Whipple's equation, as was expected, gives the highest penetration.

For thick aluminum targets, the effects of the ratio of projectile to target density on the penetration to diameter ratio for the velocity range of meteorites are shown in Fig. I-5. The different equations are in closer agreement at the high than the low density ratios. An analysis was made of the comparative test data, using Summers' and Bjork's equations with available test data (Fig. I-6). From the figure, Summers' equation matches the experimental data over a wide range of  $\left(\frac{\rho_M}{\rho_t} \times \frac{V}{C}\right)$  and  $(P/d)$  to 32,800 fps. Bjork's equation

does not fit the test data, as shown on Fig. I-6 and seems to indicate values of  $P/d$  too low for values of  $\left(\frac{\rho_M}{\rho_t} \times \frac{V}{C}\right)$  of 1.0 and higher. It is of interest

to show the range of  $\left(\frac{\rho_M}{\rho_t} \times \frac{V}{C}\right)$  that might be experienced for meteorites hitting an aluminum target as shown in the following tabulation.

Range of $\left(\frac{\rho_M}{\rho_t} \times \frac{V}{C}\right)$ for Meteorites On Aluminum Targets				
Meteorite Type	Density (g/cu cm)	$\frac{\rho_M}{\rho_t} \times \frac{V}{C}$		
		Minimum Velocity V = 11 km/sec	Average Velocity V = 28 km/sec	Maximum Velocity V = 72 km/sec
Dustball	0.05	0.0386	0.0984	2.52
Stony	2.7	2.08	5.40	13.6
Iron	7.8	6.01	15.30	39.3

For aluminum target,  $\rho_t = 2.8$  g/cu cm;  $C = 5.1$  km/sec

The range of test data extends to a value of  $\left(\frac{\rho_M}{\rho_T} \times \frac{V}{C}\right) = 6.1$  for the Ballistics Research Laboratory tests at 10 kilometers per second.

Summers' equation was used for the study analysis to determine meteorite penetration because of its close agreement with experimental data (Fig. I-6).

~~CONFIDENTIAL~~

## C. DETERMINATION OF REQUIRED SKIN THICKNESS

Summers' formula gives the penetration of a projectile in a thick target. Since most structural components of the spacecraft have relatively thin skins, a formula is required for penetration into thin targets. Kinard et al (Ref. 11) indicates that a projectile can completely penetrate a target the thickness of which is 1-1/2 times as large as the penetration into a quasi-infinite target. Since this analysis explores the probability of no penetration of various pressurized components of the spacecraft, the required thin skin thickness was assumed to be twice the depth of penetration in a thick target given by Summers' equation. The factor of two rather than 1.5 was taken because the skin of the pressurized components are under stress at the time of possible meteorite impacts.

Therefore, the required single layer skin thickness,  $t = 2p$ , where  $p$  is the penetration given by Summers' equation.

To recapitulate, the parameters of the meteorite (diameter, velocity and density) are obtained from Table I-1, and the required skin thickness can be found by using Summers' equation. Thus, the required skin thickness to resist penetration by a meteorite of a given visual magnitude can be determined. Skin thicknesses for the various materials usable on the spacecraft are listed in the following tabulation.

## Material Properties

<u>Material</u>	<u>Density (lb/cu in)</u>	<u>Speed of Sound in Material (ft/sec)</u>
Aluminum	0.101	16,740
Steel	0.281	16,410
Magnesium	0.067	16,500
Titanium	0.162	17,800
Glass	0.081	17,750
Phenolic-nylon	0.044	5,320

~~CONFIDENTIAL~~

The results are presented in Fig. I-7 for these materials. The curve for glass has been included because of its use for windows and optical sights. Phenolic-nylon is an ablative heat shield material. Fig. I-8 shows the unit weight required to withstand penetration by a meteorite of a given visual magnitude.

Most of the structural material used for the pressure vessels of the command module and the mission module, the fuel tanks, etc., of the spacecraft will be of aluminum alloy. Fig. I-9 is used to obtain the required skin thickness for a given value of the probability of no penetration and the exposure for aluminum alloy material. It was developed from the methods used to establish Figs. I-3 and I-7 and is essentially a cross plot of them. Fig. I-9 was used to determine the overall probability of no penetration for the spacecraft as will be shown later.

#### D. DESIGN PROBABILITY OF NO PENETRATION

The spacecraft will be exposed to the relatively unknown hazard of meteorite impacts. Since many components of the spacecraft are pressurized vessels (tanks, etc.), these components must be able to withstand, with a reasonable reliability, the chance of meteorite impact during the 14-day mission. Accordingly, a design value must be selected for the probability of no meteorite penetration of critical components. The design value selected is 95% overall probability of no meteorite penetration using Whipple's 1957 meteorite model and Summers' penetration equation. This 95% value represents a best-judgement estimate after considering spacecraft weight limits and the desired chance of completing the mission.

~~CONFIDENTIAL~~

### E. METEORITE BUMPER CONCEPT

Preliminary analyses using the curves of Fig. I-9 indicated that heavy aluminum single-layer skin thicknesses are required to obtain a probability of no penetration of 95% or higher for the larger components of the spacecraft (Fig. I-10). For example, the mission module has a surface area of 271 square feet and an exposure for the 14-day mission of  $271 \times 14 = 3795$  sq ft-days. Using Fig. I-9, the following skin thicknesses can be found.

#### Skin Thickness Requirements

Probability of No Penetration	Required Single Layer Skin Thickness (in.)
0.80	0.061
0.90	0.076
0.95	0.100
0.99	0.171
0.999	0.390
0.9999	0.880

Since it is desired to obtain 0.95 overall probability of no spacecraft penetration, the probability value for each of the components will have to be approximately 0.99. This would indicate a skin thickness of 0.171 inches which is much heavier than that required by pressure loads. However, Whipple proposes the meteorite "bumper" concept which indicates a significant reduction in total skin thickness by using two skins suitably spaced rather than one thick skin. The outer skin serves as a shield (bumper) and causes the meteorite to disintegrate on impact, greatly reducing inner skin damage. From tests by Olshaker (Ref. 12), it appears that a bumper of suitable design may allow a reduction in a single-layer thickness to one third. Olshaker's data were obtained from tests using lead targets.

A recent paper by Wallace et al (Ref. 13), states that a weight reduction of 50% or more may be achieved by a proper shield design. For the study analysis, it is assumed that the use of a bumper allows a reduction such that the combined thickness of the bumper shield and the adjoining skin is only one-third of a single layer skin thickness needed to resist meteorite penetration. To take advantage of the bumper concept, the critical components of the spacecraft are protected by an 0.040-in. aluminum skin around the propulsion and equipment module, and the mission engine components (Fig. I-10). The command module pressure vessel is protected by the heat shield which serves as a bumper. The 0.040-in. bumper skin thickness is based on an analysis made at The Martin Company (Ref. 14). This analysis indicates the shield thickness should be equal to 0.47 times the radius of the meteorite to give the most efficient conversion of energy. As indicated in Fig. I-1, the range of design meteorites for the spacecraft is from visual magnitude 7 to 16; thus, the bumper shield thickness is in accordance with Ref. 14.

~~CONFIDENTIAL~~

## Bumper Thickness Requirements

Visual Magnitude	Diameter of Meteorite (in.)	Bumper Thickness = $(0.47 \times \frac{d}{2})$
7	0.453	0.110
8	0.333	0.078
9	0.246	0.058
10	0.181	0.043
11	0.133	0.032
12	0.098	0.023
13	0.072	0.017
14	0.053	0.0125
15	0.039	0.0092
16	0.029	0.0068

An 0.040-in. aluminum skin will resist meteorite puncture of visual magnitude 14 and higher (Fig. I-7). The 0.040-in. bumper skin can be considered as an average bumper thickness until more definitive data become available on the various parameters of bumper shield design.

## F. HYPERVELOCITY IMPACT TESTS

Hypervelocity impact tests initiated by The Martin Company are being conducted by the Ballistic Research Laboratory at the Aberdeen Proving Ground. The objective of the tests were to determine the bumper shield effectivity of aluminum alloy materials and the penetration resistance of various heat shield materials. Since only a few tests have been made to date, only general conclusions on the significance of the results can be made. Fig. I-11 and -12 show the results of the impact of a 0.18-gram steel disc (approx  $\frac{1}{16}$ -in.

thick and  $\frac{3}{16}$ -in. diameter) at a velocity of 5.01 km/sec (16,430 ft/sec) on a

1-in. plate protected by a 0.10-in. thick shield spaced 1-in. As may be seen, the projectile was broken up by the 0.10-in. thick shield and created only  $\frac{3}{16}$ -in. deep pits in the 1-in. plate, showing that the shield is effective if the projectile is broken up. The penetration aluminum target which is unshielded for the same projectile using Summers' equation is 0.61 inch.

Figure I-13 shows the results of the impact of the 0.18-gram steel disc at 5.01 km/sec on a foamed silicon-carbide heat shield specimen with a density of approximately 0.017 lb/cu in. The silicon carbide shows severe cratering and spalling. The adhesive has been torn from both the silicon carbide and the 0.063-in. aluminum backup plate. The 0.063-in. plate shows a large petal-shaped hole apparently caused by a pressure wave effect from the silicon carbide particles. The specimen (Fig. I-14) is foamed silicon carbide impregnated with phenolic resin. The density of the specimen is about 0.038 lb/cu in. and is bonded to an 0.063-in. aluminum alloy backup plate. The damage (Fig. I-14) was caused by the impact of a 0.18-gram steel disc ( $\frac{1}{16}$ -in.

~~CONFIDENTIAL~~

thick by approximately 3 -in. diameter) at a velocity of 5.01 km/sec on the  
I6  
2 1/2-in. thick specimen. The crater is approximately 2-in. deep and 2 1/2-in.  
in diameter. The penetration given by Summers' equation for this test is 2.54-  
in.

The silicon carbide brick was badly cracked and the 0.063-in. metal back-up plate was partially separated from the brick. No bulging or perforation of the 0.063-in. plate occurred in this test. Because of its brittle behavior, foamed silicon carbide does not appear promising in its ability to withstand hypervelocity impacts.

#### G. RESULTS AND RECOMMENDATION

The results of the meteorite penetration study for the spacecraft are shown in Table I-2. As previously explained, the analysis is based on Whipple's 1957 meteorite model and Summers' penetration equation. To obtain an overall vehicle probability of no penetration, the exposed surface area and effective skin thickness of various critical components were used. The 0.040-in. thick external skin shown in Fig. I-10 surrounds the critical components of the mission and equipment module and the propulsion system. Advantage has been taken of this surrounding skin to serve as a meteorite bumper to protect the enclosed components. Likewise, the superalloy honeycomb panel and the ablation material serve as a bumper for protection of the command module pressure vessel. In order to arrive at the probability of no penetration for the various components, it was necessary to determine the equivalent skin thickness of aluminum where the materials used are different (e. g., the heat shield). This was done by finding the equivalent penetration resistance of the material in terms of aluminum. The penetration furnished by the bumper shield is assumed to increase the penetrating resistance of the shield plus the structural skin by a factor of three.

Table I-2 shows that the M-1-1 spacecraft has approximately 0.95 overall probability of no penetration. This probability is based on a conservative assumption of no earth shielding, no mutual shielding of the components by each other and penetration based on meteorite impacts normal to surface.

Until more knowledge of the meteorite environment in space and the hypervelocity impact mechanism at meteorite velocities is obtained, any meteorite penetration analysis represents only an estimate. No precise evaluation of the meteorite hazard can be made.

The following recommendations are offered

- (1) The obvious continuation of the present meteorite observation programs--visual, radar, radio and photographic.



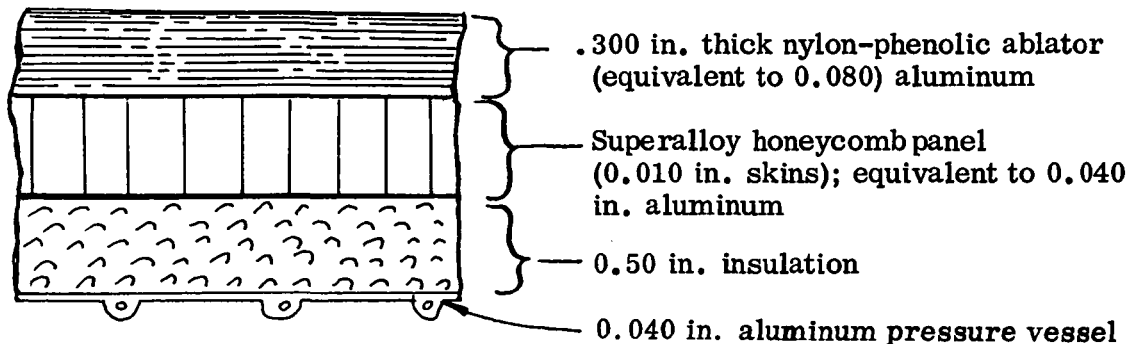
TABLE I-2

Model 410 Meteorite Penetration Probability  
(14-day mission)

Component	Basic Aluminum Skin Thickness (in.)	Bumper Skin Thickness (aluminum equivalent in.)	Effective Aluminum Skin Thickness with Bumper Effect (in.)	Surface Area (sq ft)	Exposure (sq ft - days)	Probability of No Penetration
Command module	1/0.040	1/0.120	2/0.480	369	5,170	0.9991
Mission module	0.040	4/0.040	2/0.240	271	3,795	0.994
Main propellant system						
Hydrogen tank	0.040	4/0.040	2/0.240	391	5,470	0.992
Oxygen tank	0.032	4/0.040	2/0.216	130	1,820	0.996
						0.9880-6/- -0.9496 overall probability
Vernier rocket system						
N <sub>2</sub> H <sub>4</sub> tank	0.070	4/0.040	2/0.330	15.9	223	0.9999
N <sub>2</sub> O <sub>2</sub> tank	0.070	4/0.040	2/0.330	15.9	223	0.9999
Helium reservoir	3/0.270	4/0.040	2/0.93	7.08	99.1	0.9999
Fuel cell tanks						
Hydrogen tank	0.040	4/0.040	2/0.240	25.2	352	0.9995
Oxygen tank	0.040	4/0.040	2/0.240	13.6	190	0.9997
						0.9992
Engine (cooling tube)						
External surface	5/0.025	4/10.040	2/0.195	8.4	121	0.9997
Internal surface	5/0.025	NONE	0.025	7.65	40	0.969
						0.9687

Refer to "Table Notes" on following page.

## 1. Average heat shield cross section



2. Assuming bumper increases effective skin thickness 3 times i. e.,  
effective skin  $3 \times (\text{Bumper thickness} + \text{Basic thickness})$
3. Helium Reservoir is 0.192 in.-wall Titanium (equivalent to 0.270 in. of  
aluminum)
4. External 0.040 in. aluminum skin acts as a bumper
5. Engine nozzle cooling tubes are 0.013 in.-wall stainless steel (equivalent  
to 0.025 in. aluminum)
6. Overall probability of no penetration, no earth shielding, no mutual shield-  
ing of components and all meteorite impacts normal to surface.
7. Exposure based on 3-1/2 days earth-to-moon and 7-day lunar orbit (ex-  
posure = 10-1/2 days) after which period engine is not used. A reduction  
factor of 0.5 accounts for the sloping sides of the nozzle.

~~CONFIDENTIAL~~

- (2) Specific satellite probes to obtain data on the size and frequency of meteorites near the earth. A program may be undertaken to evaluate the meteorite risk based on time that certain size satellites such as Vanguard and Echo have been safely orbiting the earth.
- (3) Continuation of the current hypervelocity impact programs, but emphasizing target impact and typical spacecraft materials and construction. The penetration characteristics of typical or possible heat shield materials such as charring ablators, sublimating ablators, ceramics, etc., need investigation.
- (4) Further investigations of optimum meteorite bumper shield parameters for typical spacecraft materials. This is important because the use of a meteorite bumper shield appears a necessity for large spacecraft.

~~CONFIDENTIAL~~

## II. REFERENCES

1. Whipple, F. L., "The Meteorite Risk to Space Vehicles," American Rocket Society Paper 499-57.
2. Bjork, R. L., "A Conservative Estimate of the Meteoroid Penetrating Flux," Rand Corporation Report P-1913, February 11, 1960.
3. Jonah, F. C., "Critical Analysis of Solid Debris in Space," IAS Paper 60-73.
4. Whipple, F. L. "Symposium on Medical and Biological Aspects of the Energies of Space", October 1960.
5. Naumann, R. J., "Meteoric Effects on Long Range and Orbital Vehicles," Army Ballistic Missile Agency Report No. DS-TN-94, September 27, 1957.
6. Kornhauser, M., "Satellite Pressure Losses Caused by Meteoroid Impacts," ARS Journal, May 1960.
7. Summers, J. L., "Investigation of High Speed Impact: Regions of Impact and Impact at Oblique Angles," NASA TN D-94, October 1959.
8. Bjork, R. L., "Effects of a Meteoroid Impact on Steel and Aluminum in Space" Proceedings Xth International Astronautical Congress, London, 1959.
9. Bjork, Comments on "The Effect of Micrometeorites on Reflecting Surfaces", Rand Corporation Report P-1936, February 29, 1960.
10. Kinard, W. H. et al, "Effect of Target Thickness on Cratering and Penetration of Projectiles Impacting at Velocities to 13,000 feet per second," NASA memorandum 10-18-58 L, December 1958.
11. Olshaker, A. E., "An Experimental Investigation In Lead of the Whipple Meteor Bumper," Fourth Symposium "Hypervelocity Impact" AFGC-TR-60-39, September 1960.
12. Wallace, R. R. et al, "Effects of Hypervelocity Particles on Shielded Structures", ARS Paper 1683-61.
13. "Manned Lunar Vehicle System, Vol. 1, Feasibility Survey," Engineering Report ER 11245 M, Part 1, The Martin Company.

~~CONFIDENTIAL~~

~~CONFIDENTIAL~~

ER 12018

~~CONFIDENTIAL~~

M-III-1

### III. ILLUSTRATIONS

~~CONFIDENTIAL~~

ER 12018

~~CONFIDENTIAL~~

~~CONFIDENTIAL~~

CONFIDENTIAL

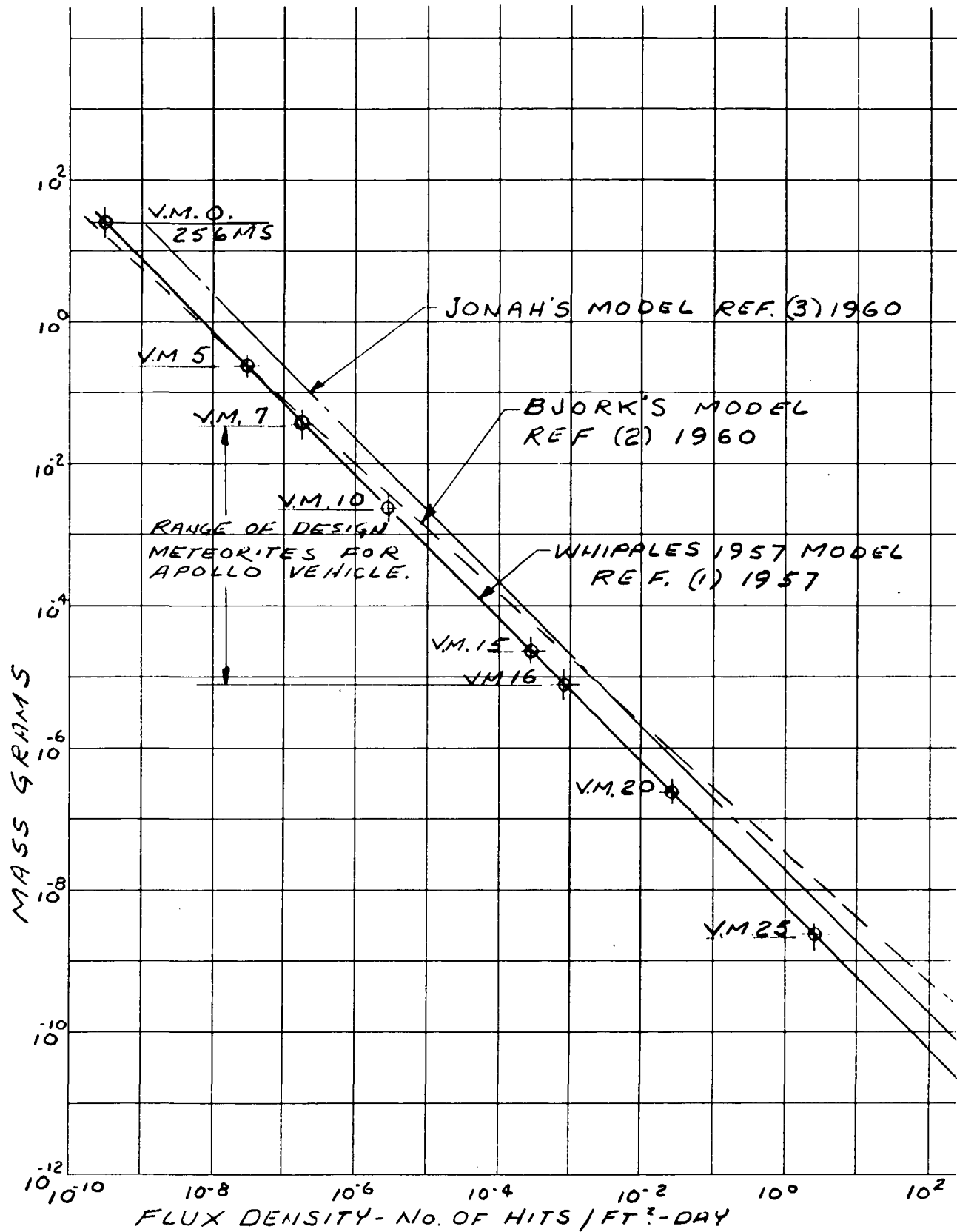


Fig. I-1. Meteorite Mass Versus Flux Density--Comparison of Data

CONFIDENTIAL

ER 12018



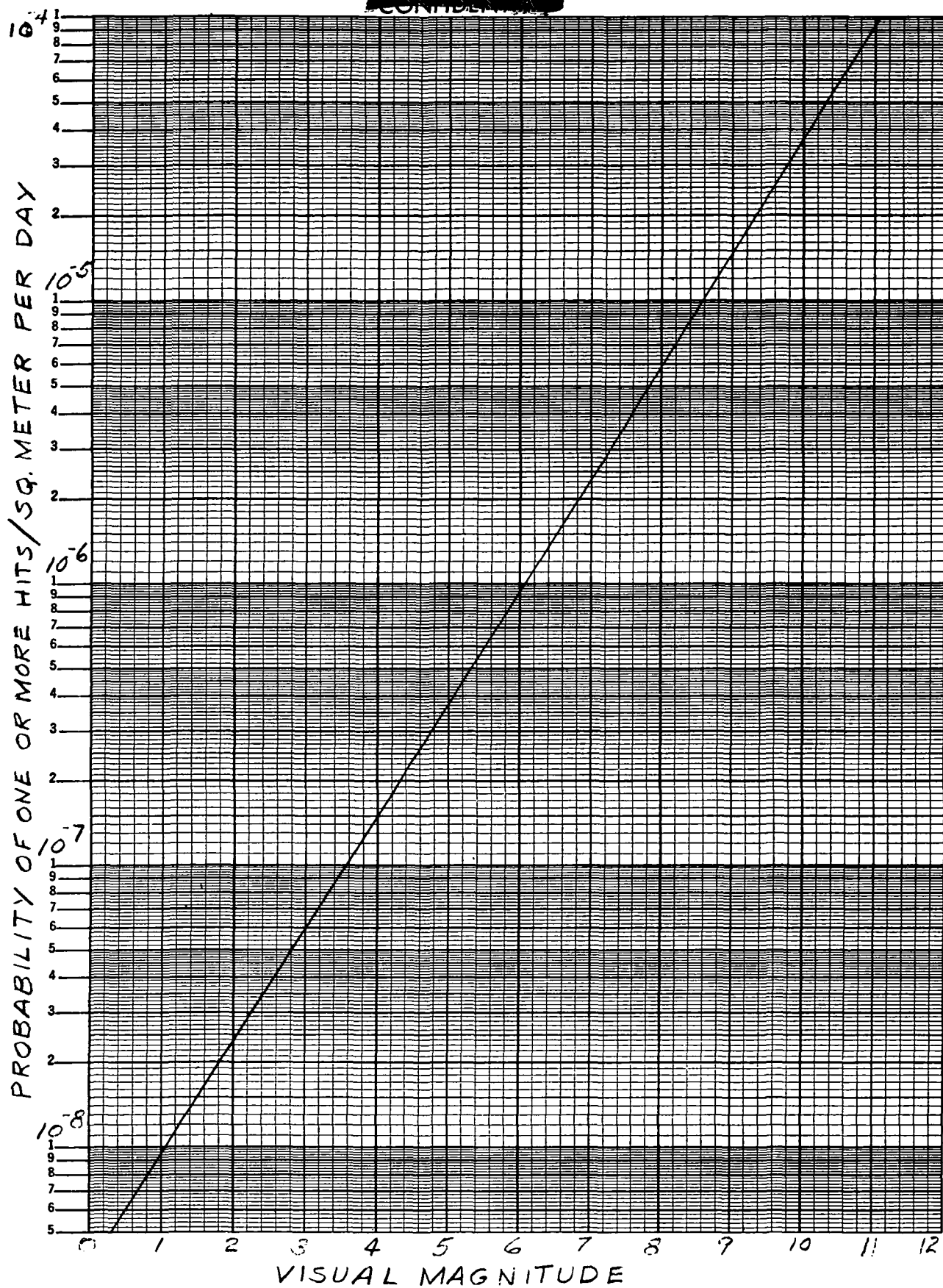
~~CONFIDENTIAL~~

Fig. I-2a. Probability of One or More Hits Versus Visual Magnitude

~~CONFIDENTIAL~~

ER 12018

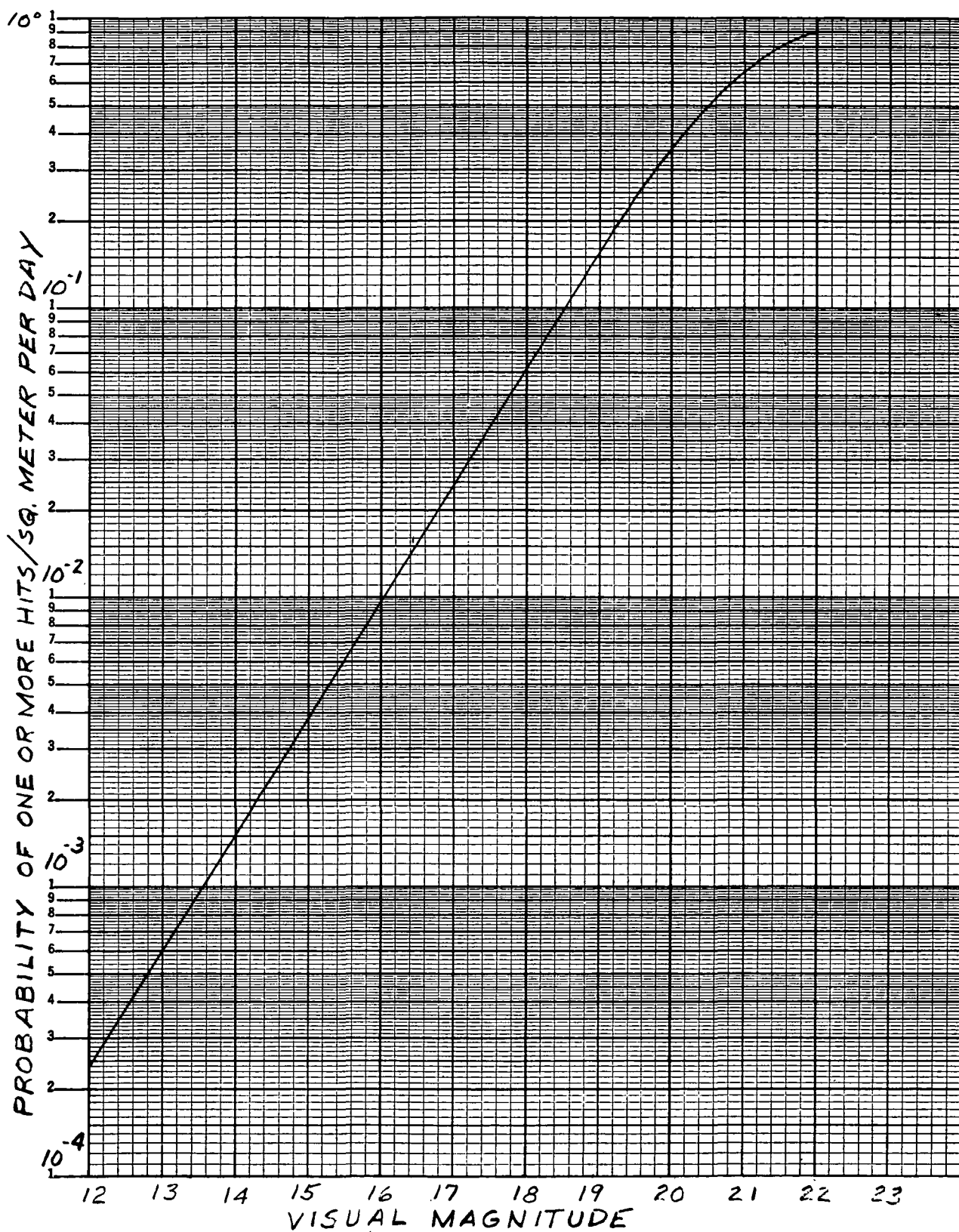
~~CONFIDENTIAL~~

Fig. I-2b. Probability of One or More Hits Versus Visual Magnitude

~~CONFIDENTIAL~~

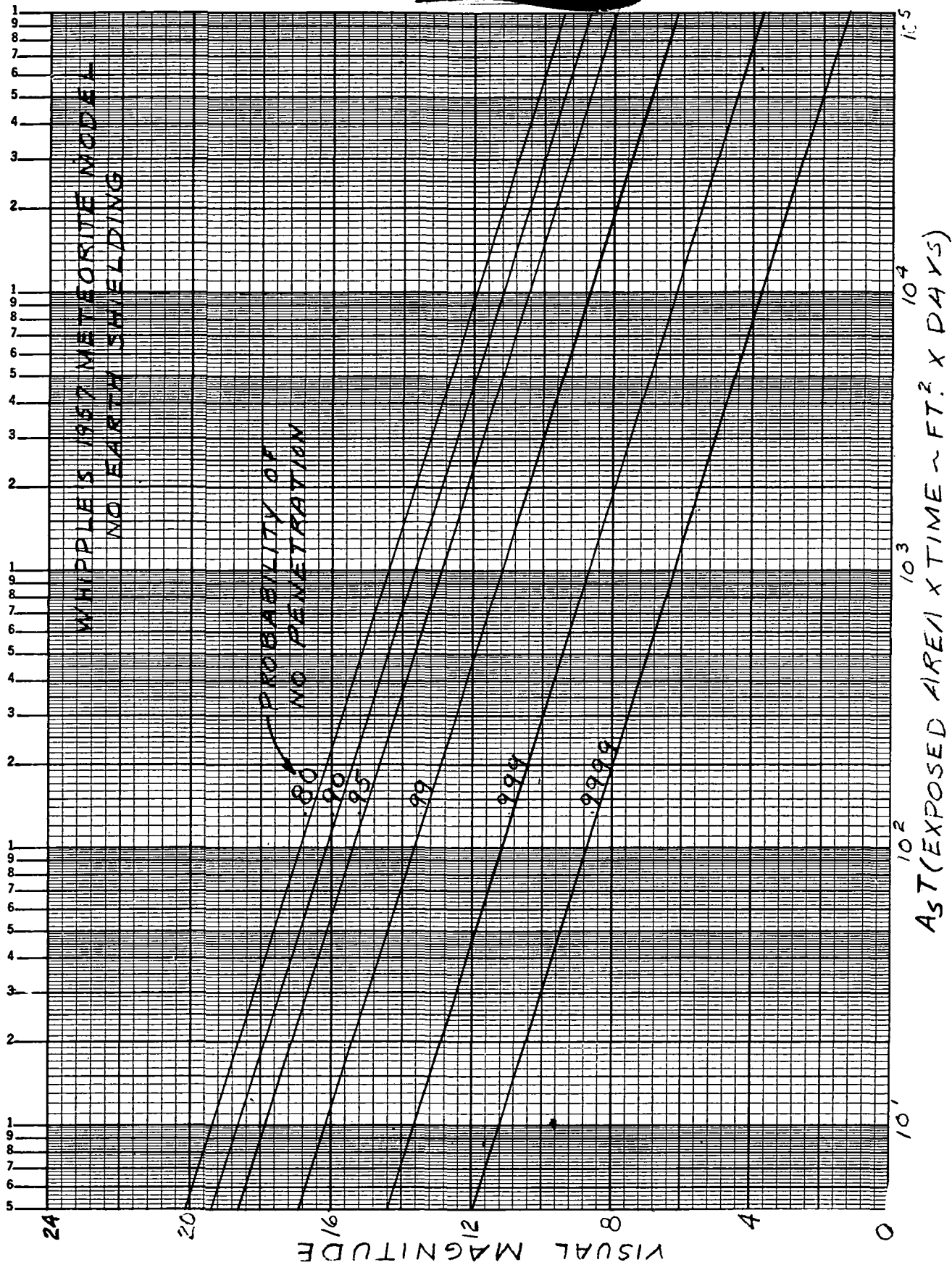
~~CONFIDENTIAL~~

Fig. I-3. Visual Magnitude to be Protected Against Versus Exposed Area Times Exposure Time

~~CONFIDENTIAL~~

CONFIDENTIAL

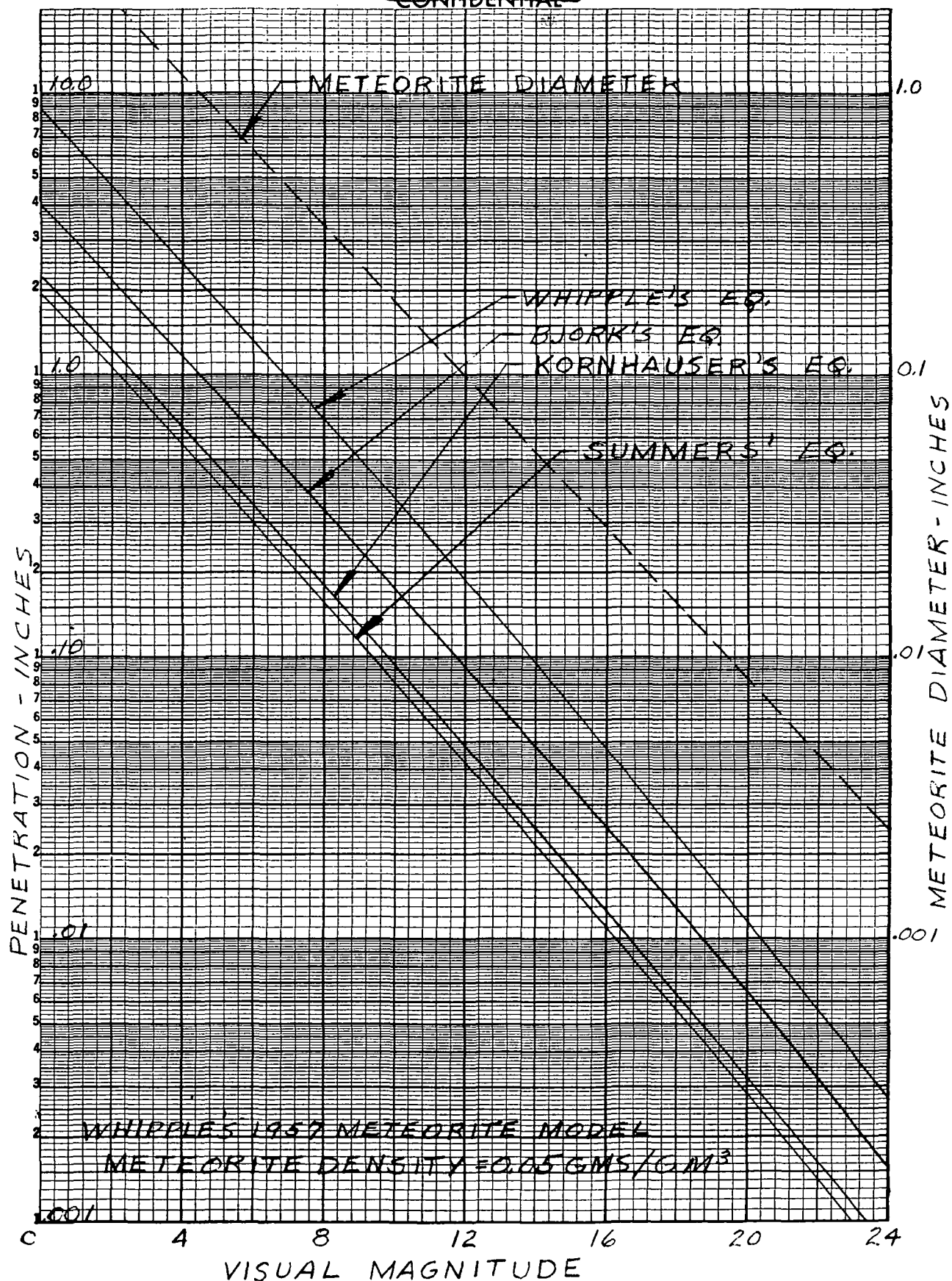


Fig. I-4. Penetration Versus Visual Magnitude for Thick Aluminum Targets--  
Comparison of Equations

CONFIDENTIAL

ER 12018





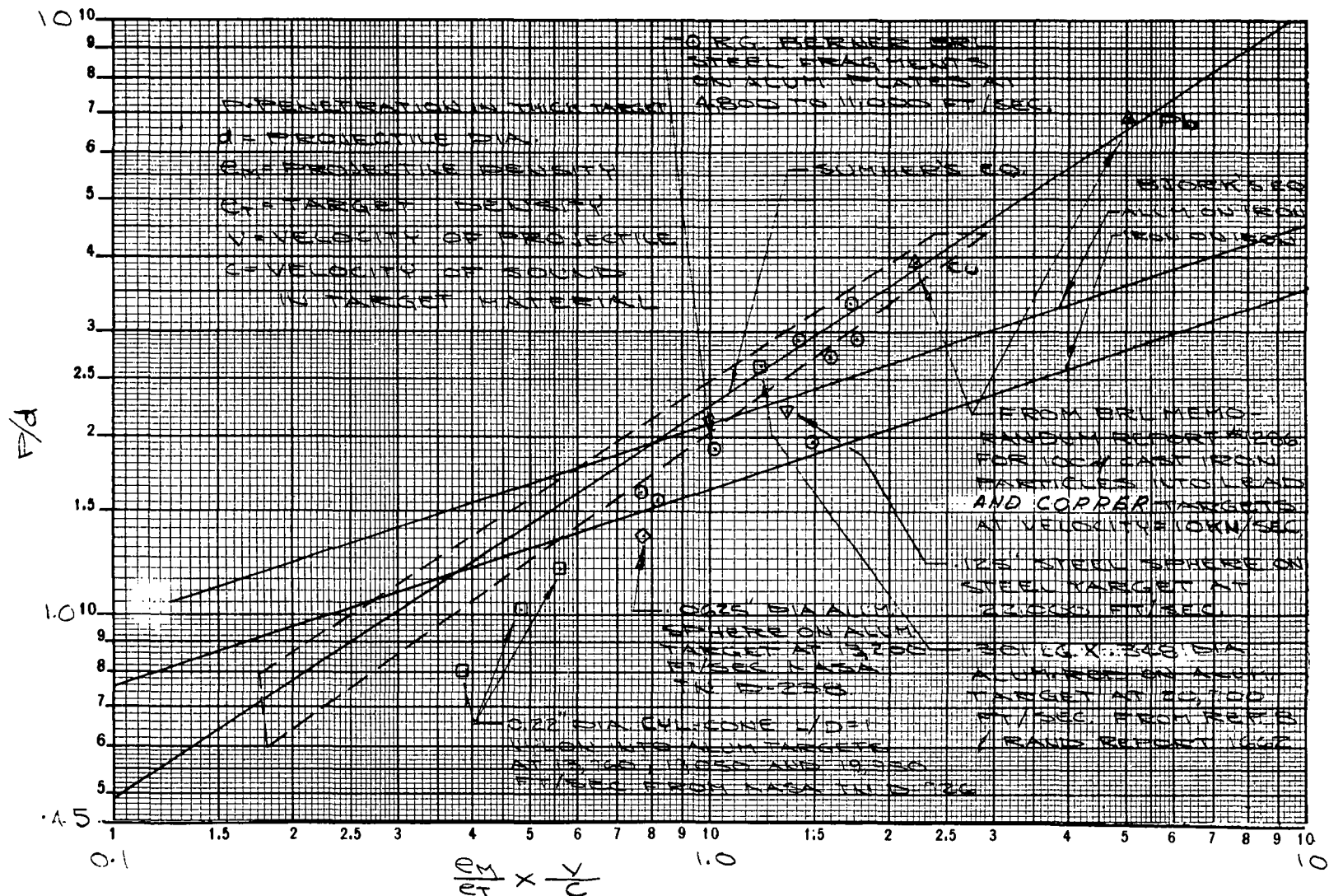


Fig. I-6. Comparison of Test Data with Summers' and Bjork's Penetration Equations for Thick Targets

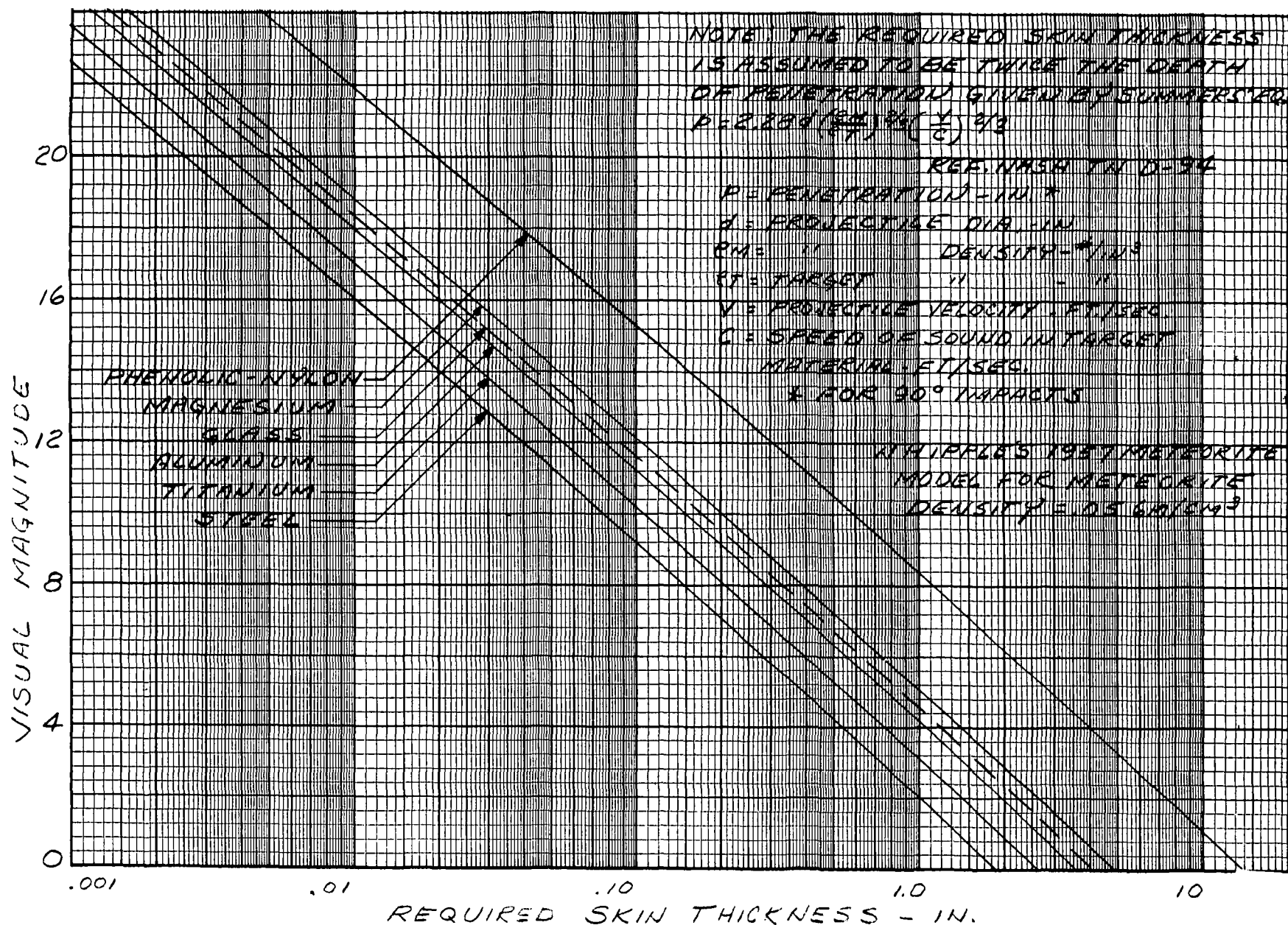


Fig. I-7. Required Skin Thickness Versus Visual Magnitude--Whipple's 1957 Meteorite Model

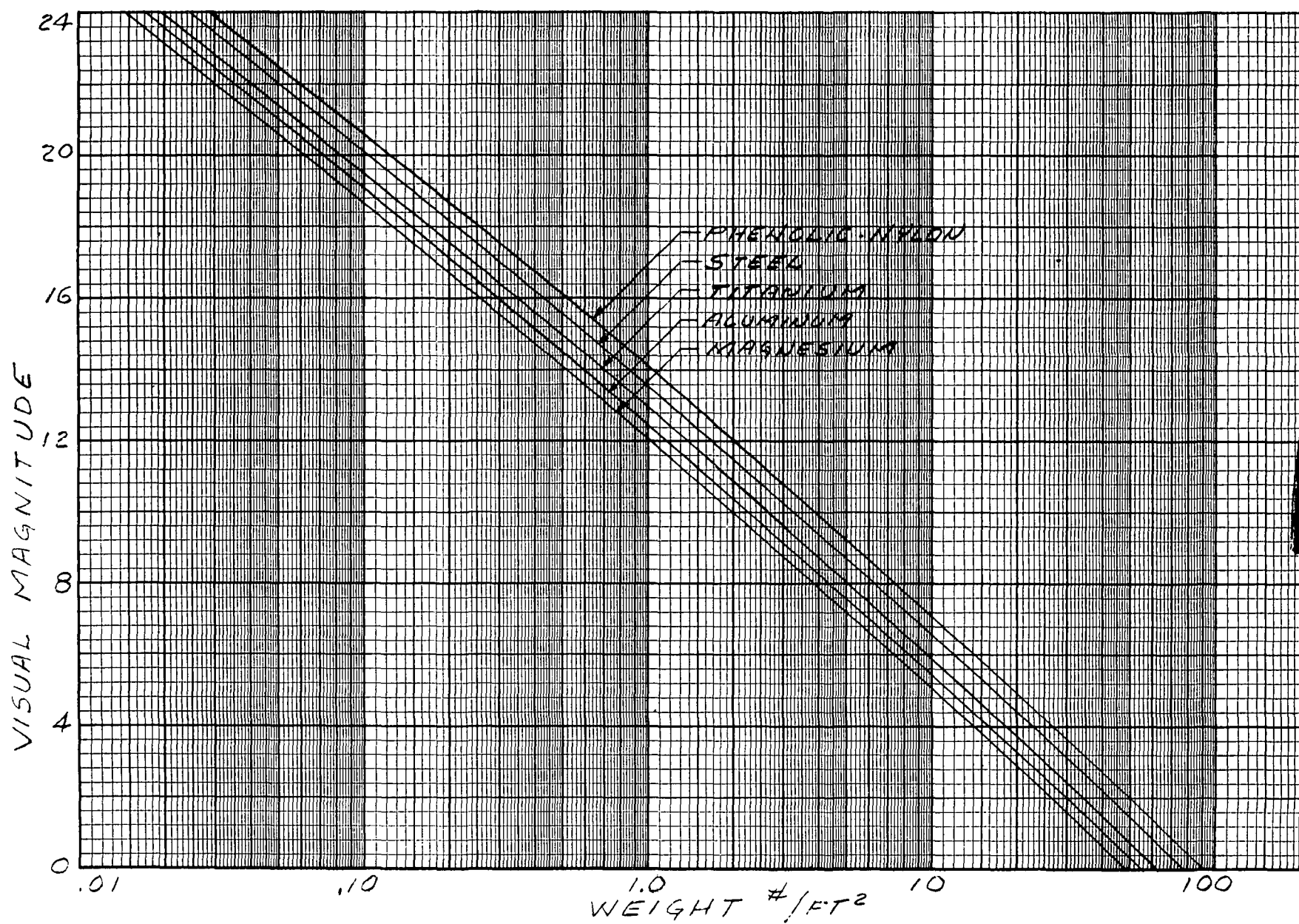


Fig. I-8. Required Skin Weight Versus Visual Magnitude



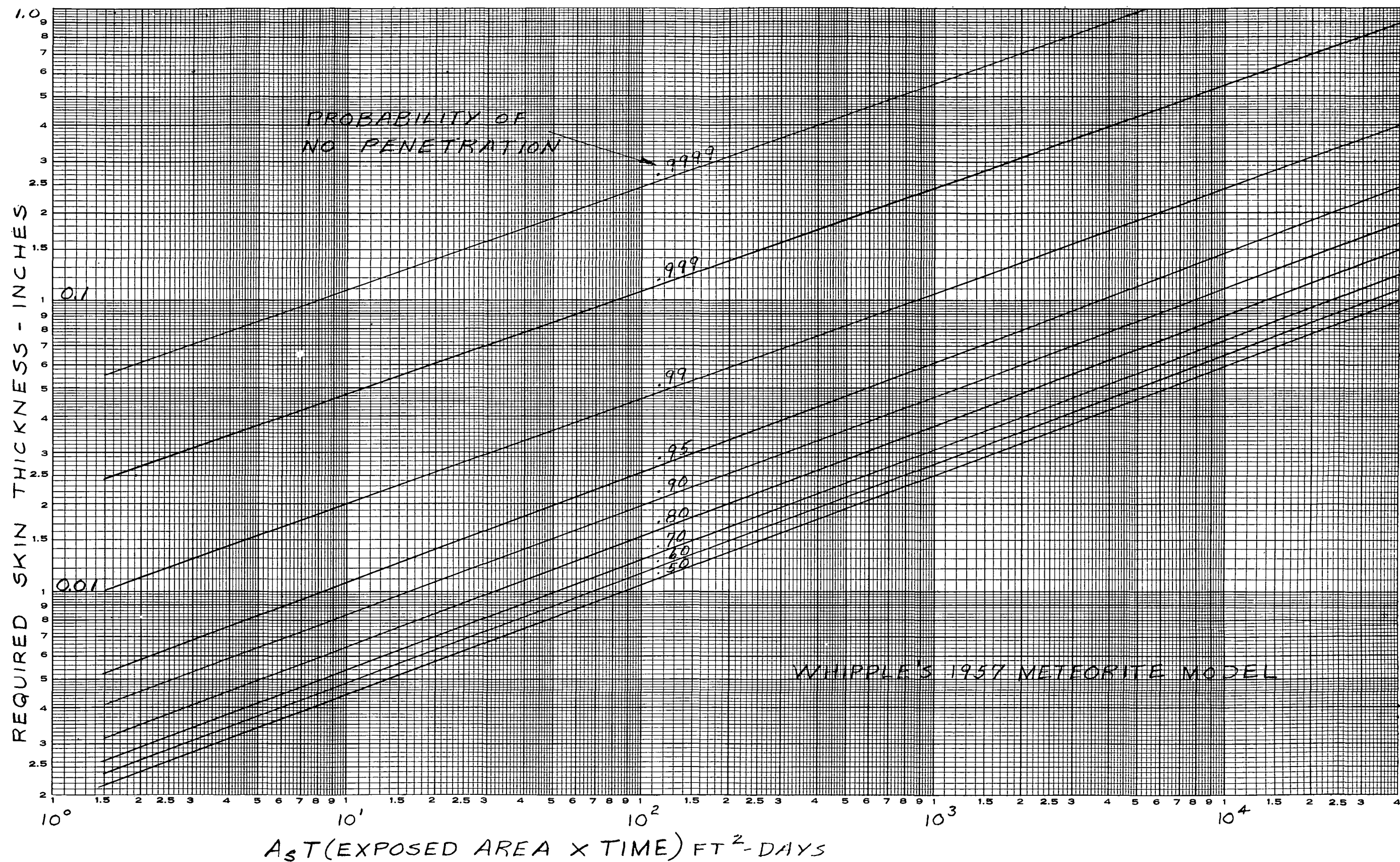
~~CONFIDENTIAL~~

Fig. I-9 Aluminum Skin Thickness Versus Exposed Area Times Time--  
Whipple's 1957 Meteorite Model

~~CONFIDENTIAL~~

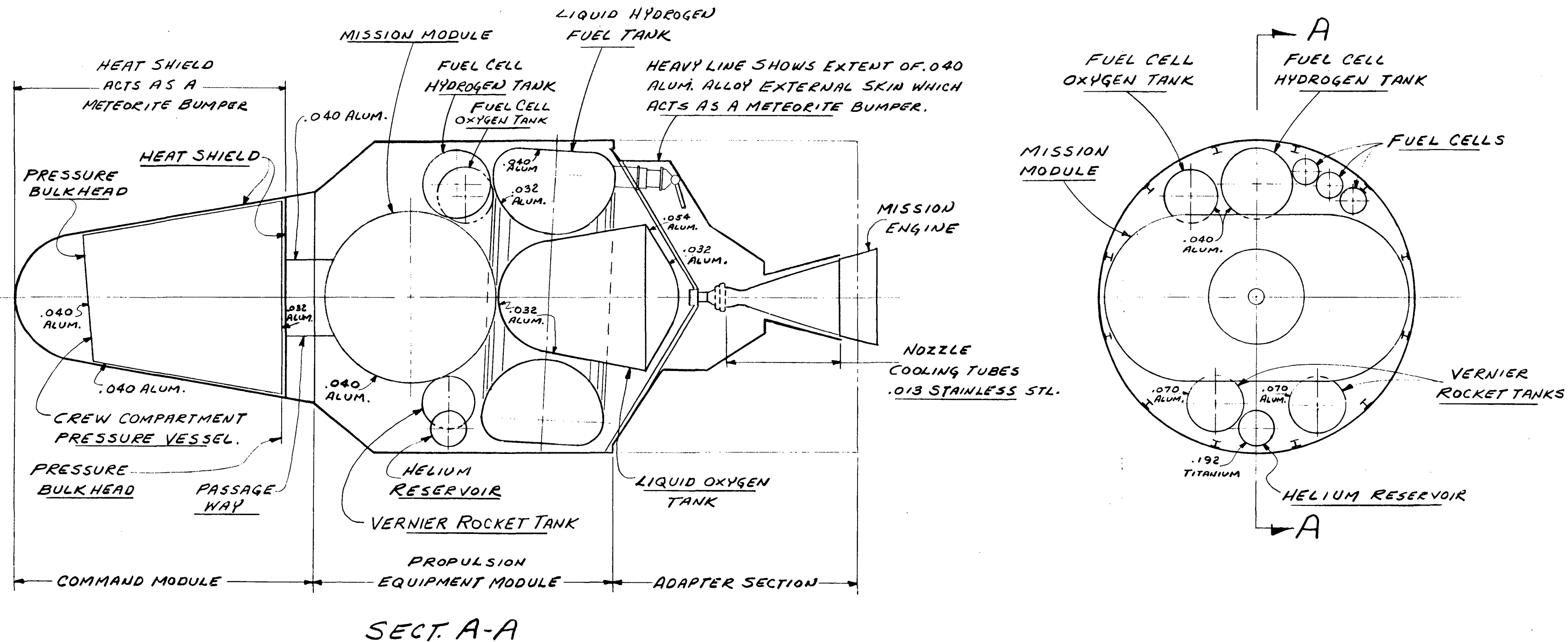


Fig. I-10. Meteorite Shield Arrangement for M-1-1 Apollo Spacecraft

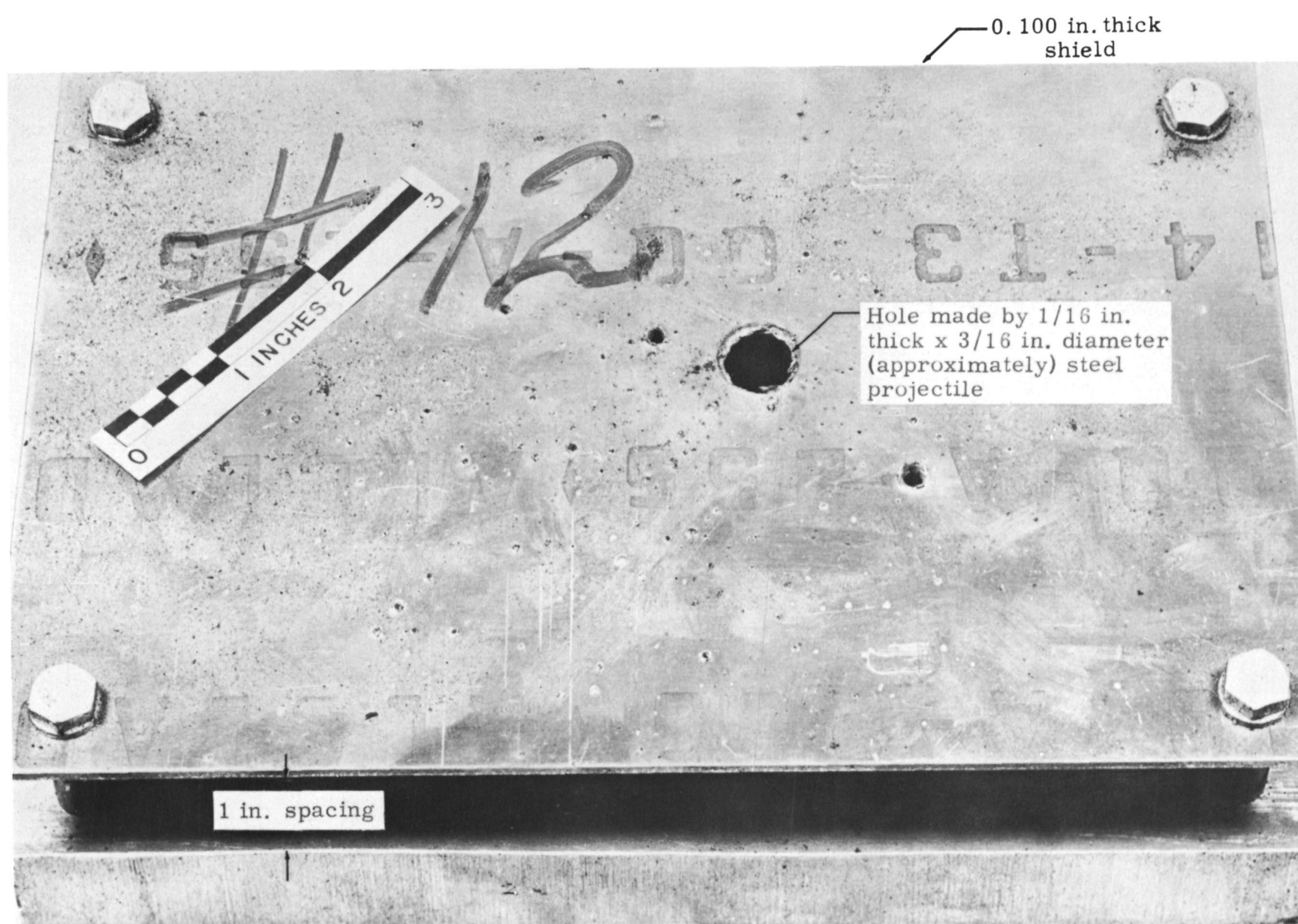


Fig. I-11. Impact of Steel Disc of 0.18 Gram at 5.01 km/sec on 2014 ST Aluminum Alloy Shield Specimen

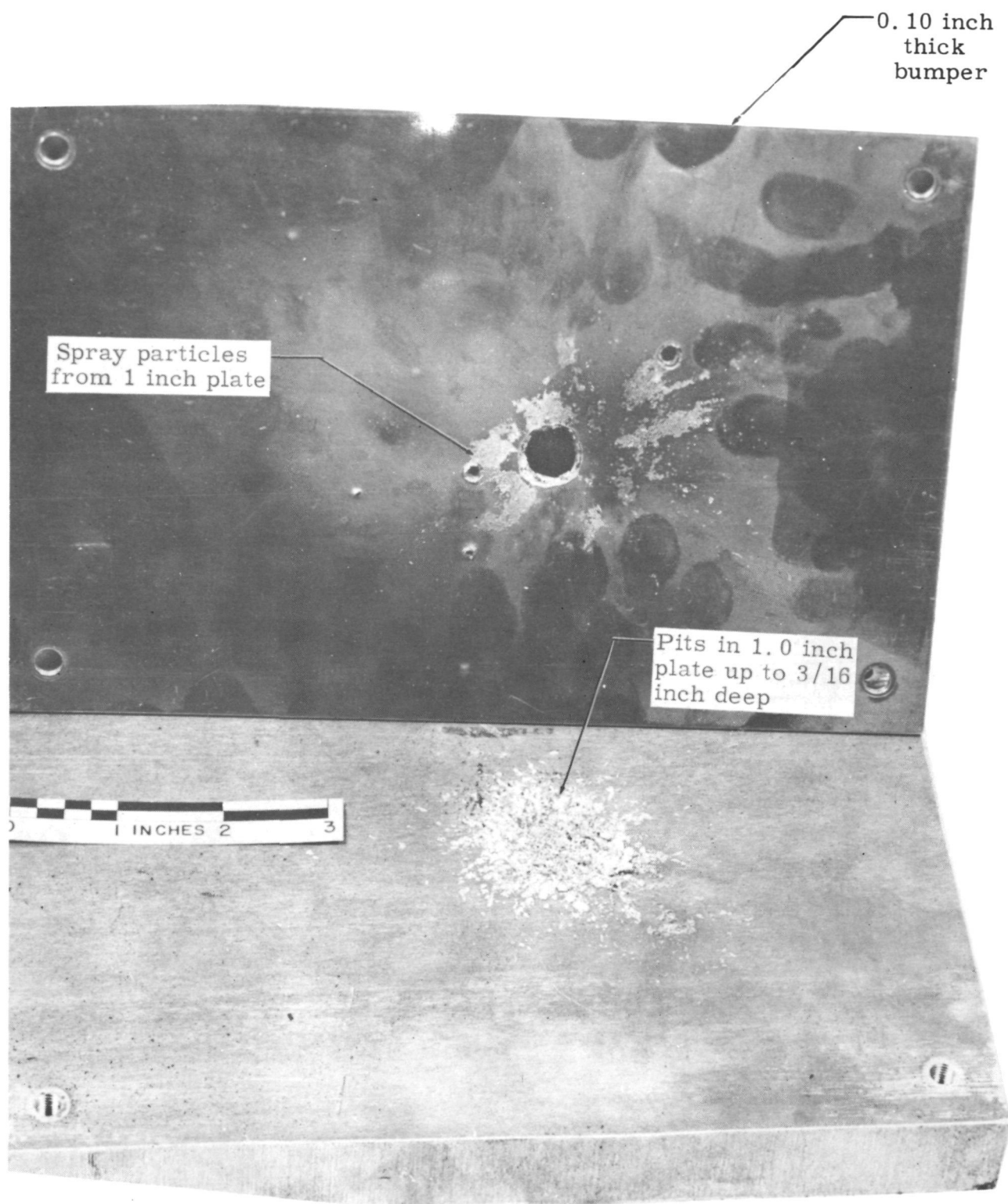
~~CONFIDENTIAL~~

Fig. I-12. Damage to 1-in. Plate After the Projectile Has Passed Through 0.10-in. Thick Shield--Projectile Steel Disc of 0.18 Gram with Velocity Equal to 5.01 km/sec

~~CONFIDENTIAL~~

ER 12018



CONFIDENTIAL

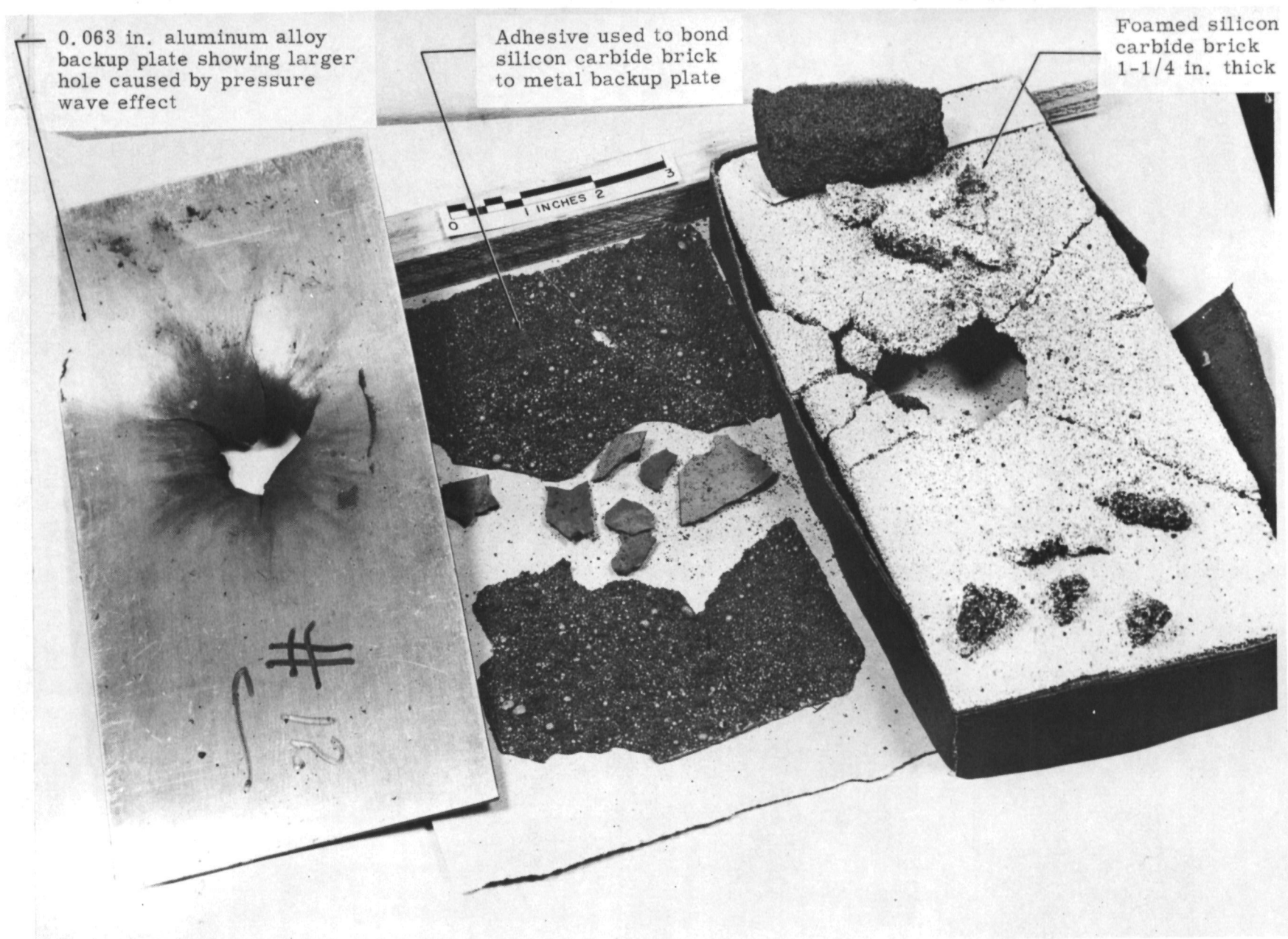


Fig. I-13. Impact of Steel Disc Projectile of 0.18 Gram at 5.01 km/sec on Foamed Silicon Carbide Heat Shield Specimen

CONFIDENTIAL  
ER 12018

CONFIDENTIAL

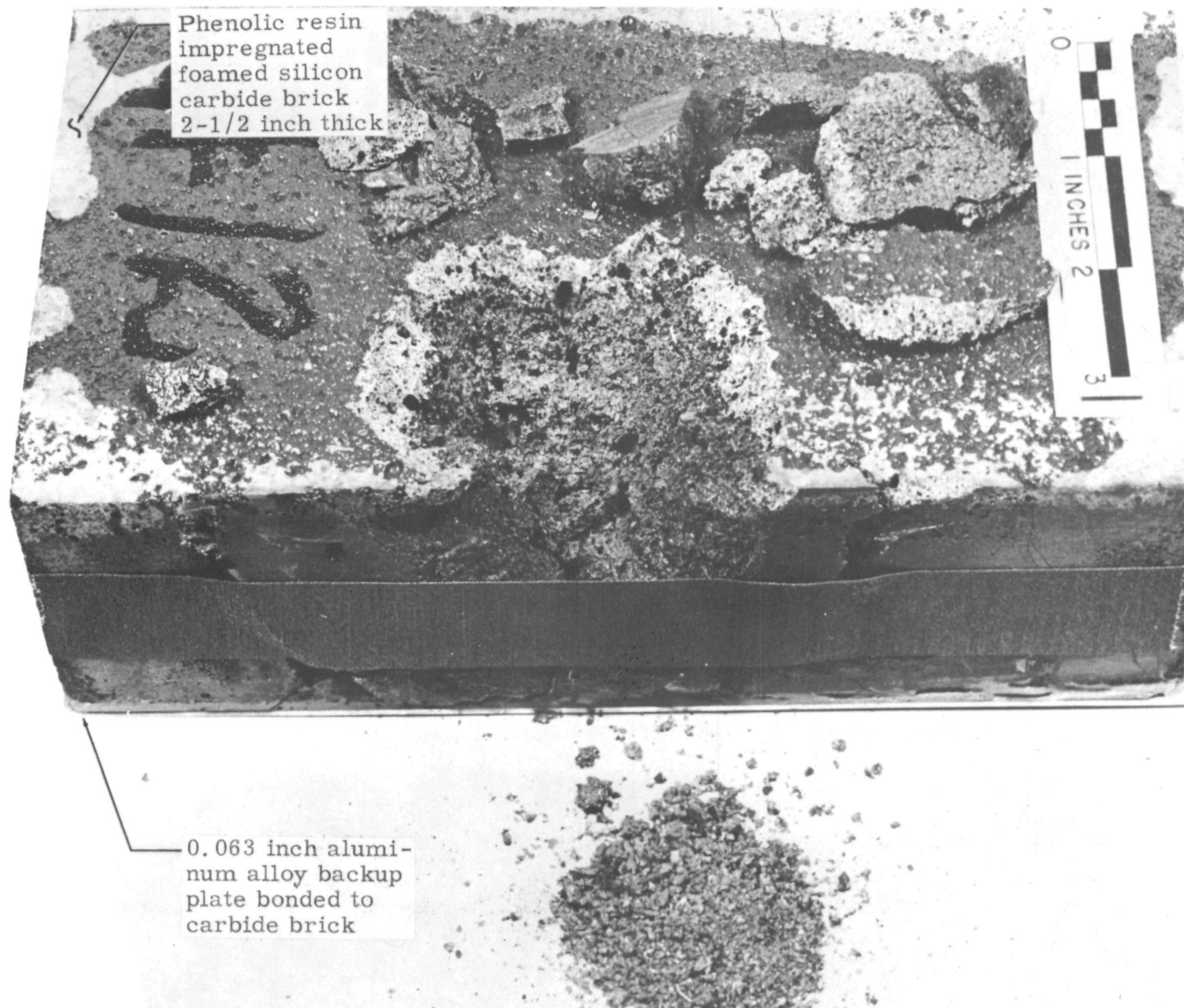


Fig. I-14. Impact of Steel Disc Projectile at 5.01 km/sec on Foamed Silicon Carbide Impregnated with Phenolic Resin

CONFIDENTIAL

CONFIDENTIAL

CONFIDENTIAL

ER 12018

*THE FINAL REPORT of The Martin Company's Apollo design feasibility study comprises the following publications:*

System and Operation	ER 12001
Support	ER 12002
Trajectory Analysis	ER 12003
Configuration	ER 12004
Aerodynamics	ER 12017
Mechanical Systems	ER 12005
Aerodynamic Heating	ER 12006
Guidance and Control	ER 12007
Life Sciences	ER 12008
Onboard Propulsion	ER 12009
Structures and Materials	ER 12010
Instrumentation and Communications	ER 12011
Space Environment Factors	ER 12018
Test Program	ER 12012
Fabrication and Quality Assurance	ER 12013
Program Management	ER 12014
Business Plan	ER 12015
Preliminary Specifications	ER 12016



CONFIDENTIAL

CONFIDENTIAL